DUBLIN CITY UNIVERSITY

LASER, OPTICAL AND ELECTRICAL DIAGNOSTICS OF COLLIDING LASER-PRODUCED PLASMAS

A Thesis Submitted for the Degree of:

DOCTOR OF PHILOSOPHY

Presented to:

THE SCHOOL OF PHYSICAL SCIENCES

Submitted by:

PÁDRAIG HOUGH B.SC. (HONS)

Research Supervisor:

PROFESSOR JOHN T. COSTELLO

January 2010

Declaration:

I hereby certify that this material, which I now submit for assessment on the programme of study leading to the award of Doctorate of Philosophy is entirely my own work, that I have exercised reasonable care to ensure that the work is original, and does not to the best of my knowledge breach any law of copyright, and has not been taken from the work of others save for and to the extent that such work has been cited and acknowledged within the text of my work.

Signed: _____

ID No.: 56114591

Date: _____/_____/_____

To my parents.

Acknowledgements

First and foremost I would like to thank my supervisor, Prof. John Costello, who has been a constant source of knowledge and guidance over the course of the project. His support and direction has been essential throughout my Ph.D. and I could not have wished for a better supervisor. I would also like to extend this gratitude to Prof. Sivanandan Harilal whom I was lucky enough to meet and work closely with during my Ph.D. His advice and encouragement was central to all the work performed during the project and presented in this thesis. I would also like to thank Dr. Jean-Paul Mosnier whose input and advice during the project proved invaluable.

Thanks to Conor McLoughlin with whom I have shared lots of highs and lows, but definitely more great moments than not. Thanks to Ricky O'Haire not only for lots of great advice but also for the CoD! I would like to extend my gratitude to the guys in the office and the other members of the laser-plasma group (both past and present) who made the experience of pursuing a Ph.D. one of the most enjoyable experiences of my life. In particular those who have moved on: Kevin Kavanagh, Eoin O'Leary, John Dardis, Caroline Banahan, Deirdre Kilbane, Jofre Pedregosa Gutierrez and Alan Meaney, and those here presently: Vincent Richardson, Colm Fallon, Xi Jiang, Eanna McCarthy, Conor Coyle and Jack Connolly.

I would like to thank Brendan Doggett, who spent some considerable time with me dismantling my Surelite, Pat Yeates, who found time to give me a crash course in ion diagnostics and probes. Paddy Hayden – thanks for all the endless help in the lab and advice and especially for proofing reading the thesis. Mossy Kelly – thanks for everything; I'll keep an eye out for that mysterious π and don't worry, I'll frame the napkin.

I would like to thank the two-colour FLASH collaboration, as part of which, I spent a portion of my time at the Deutsches Elektronen-Synchrotron (DESY) in Hamburg working with some of the best people in the business. In particular, Michael Meyer, Denis Cubaynes, Stefan Düsterer, Paul Radcliffe, Wenbin Li and Armin Azima.

I would like to extend my thanks to all the support staff in DCU and the NCPST including Pat Wogan, Mike Aughey, Sheila Boughton, Samatha Fahy, Alan Hughes, and Ray Murphy. Lisa Peyton, for all the help with all the orders, printing and awkward requests and Des Lavelle, for helping in designing and building the new colliding plasma lab.

Finally, I would like to thank my friends and family. John E and Sepanda for all the helpful discussions. To my parents, my brothers, Seán and Dermot and my sisters, Sharon, Shelly and Paula – thanks for all the support you have given me throughout my studies. A very special thank you to Ailish, for her constant support and for keeping me smiling through all the ups and downs of my Ph.D. I know one thing for certain; I could not have done it without you.

Contents

Abstract

This thesis describes the development of and results from a new laboratory facility designed to investigate the properties and explore potential applications of colliding laser produced plasmas.

When two plasmas collide there are two extreme scenarios that can play out – the plumes can either interpenetrate or stagnate depending on the ion-ion mean free path. During interpenetration, the plasmas stream through each other, the main interaction amounting to binary collisions. In the case of stagnation, rapid accumulation of plasma material at the collision front leads to the formation of a dense layer of material between the two plasmas.

Interferometry of single laser produced plasmas created in background gaseous atmospheres expose the presence of a shock front at the plasma gas interface which rapidly expands outwards. Shadowgraphy is currently the most widely employed diagnostic technique to analyse such shock fronts and a comparison of both techniques reveals that interferometry can be used to diagnose the interaction of laser produced plasmas in gaseous environments in pressure regimes where other techniques such as shadowgraphy are not sensitive.

Optical diagnostics such as laser interferometry, fast imaging (angularly resolved) and optical emission spectroscopy have been employed to probe colliding plasmas, revealing important factors in the formation of the stagnation layer. For example the studies have found that electrons stagnate before ions and similarly ions stagnate before neutral species.

Faraday Cup measurements reveal a significant increase in ion yield normal to the target from the colliding plasma system compared to single plumes and the ions possess a much narrower range of kinetic energies.

Finally, preliminary experiments on materials deposition using colliding plasmas as the source of deposition reveal an enhancement in the number density of nano-particles deposited on a substrate compared to single plumes suggesting increased clusterisation in the stagnation layer.

Introduction

Introduction I: Thesis Structure

The main aim of this work reported herein was to design and construct a new laboratory facility to probe the fundamental physical properties of colliding plasmas. The project also had the ultimate goal of identifying and performing preliminary investigations into potential applications of colliding laser produced plasmas. This thesis has been divided into six chapters. A short description of each chapter follows.

Chapter 1: includes a brief overview of the background physics and basic concepts relevant to the work presented in the thesis. The basic theory of plasmas (including main atomic processes and equilibrium models) is presented along with the theory of the interaction of high power lasers with matter. In addition theoretical considerations underlying the plasma diagnostic techniques employed during the course of the Ph.D. are outlined. Finally the principles of colliding laser produced plasmas are also presented.

Chapter 2: presents the main experimental apparatus. This includes the design, assembly and testing of the entire experimental laboratory. The experimental setups for the various plasma diagnostic techniques are summarised.

Chapter 3: outlines the results from experiments on single laser produced plasmas. Results from interferometric and shadowgraphic probing of single laser produced plasmas created in vacuum and gaseous atmospheres are compared and contrasted.

Chapter 4: presents the results from optical and laser diagnostics of colliding laser produced plasmas, specifically spectrally and temporally resolved imaging and spatially resolved optical emission spectroscopy. Laser interferometry constitutes the laser based diagnostic of colliding plasmas.

Chapter 5: presents results on ion emission from colliding laser produced plasmas with a Faraday cup and compares the results to those from single laser produced plasmas.

Chapter 6: outlines the potential applications of colliding plasmas identified from preliminary results of experiments performed during the course of this work.

Chapter 7: concludes the thesis with a summary of all the conclusions arising to date. The chapter concludes with suggestions on possible future experiments on colliding laser produced plasmas that could build on the work in this thesis.

Introduction II: Colliding Laser Produced Plasmas

Laser produced plasmas, formed when a high power pulsed laser is focussed onto a solid density target or into a gaseous atmosphere, have been the subject of considerable attention since their discovery in 1960's [1]. Studies have been driven not only by a desire to obtain a full understanding of the fundamental physics underlying their formation and evolution across the wide parameter spaces in which they can exist but also to develop and exploit applications. Applications of single laser produced plasmas include Pulsed Laser Deposition (PLD) [2], Extreme UltraViolet (EUV) light sources [3] and ion accelerators [4]. In addition, laser plasmas are playing an important role in the search for solutions to problems including energy generation [5], analytical sciences [6, 7] and industrial, environmental and security applications [8].

Single laser produced plasmas, formed *in vacuo* or in an ambient gas atmosphere, are still the subject of significant research activity and in keeping with this, the first experiments conducted with the new laboratory facility were focused on their study. The results from the investigations of single plasma plumes are presented in Chapter 3 and provide not just a performance benchmark of the experimental system for comparison with existing studies of single laser produced plasmas, but also reference data for comparison with colliding plasma measurements. In our studies laser interferometry was used to diagnose the spatial profile of the electron density for a single plasma created both *in vacuo* and in a low pressure gaseous atmosphere. It was found that a shock wave (*i.e.* a compressive layer of gas) was visible in the interferograms when the plasma was created in a gaseous atmosphere. The expansion dynamics of this compressive layer were investigated using interferometry (low pressure ambient atmosphere) and focused shadowgraphy (high pressure background gas) and the results from both techniques compared.

The overriding motivation for the project, however, originates from a growing recognition of several important potential applications of colliding laser produced plasmas. Colliding plasmas have shown much potential as laboratory scale models of astronomical interactions between colliding shock waves where, for example, Gregory *et al.* [9] and Smith *et al.* [10] have shown how they can be used as a scaled model of astrophysical colliding shocks. Colliding plasmas have also been prevalent in the area of research into indirect drive laser nuclear fusion systems where a hollow hohlraum hosts multiple colliding plasmas as X-ray sources which are used to drive fusion in a fuel cell located at the centre of the hohlraum [11].

In addition to these applications, it has been shown [12, 13] that heating of a preformed plasma with an intense laser pulse has the ability to increase laser absorption and consequently provide emission intensity enhancement. This has led to benefits in the area of Laser Induced Breakdown Spectroscopy (LIBS), for example, where prepulsing has been shown to enhance analyte line emissions [14]. Since the stagnation layer is itself a preheated slab of plasma it can at least be speculated that it could be used as a source for similar applications.

More recently, in the area of materials deposition, Irssou *et al.* [15] have demonstrated the successful fabrication of droplet free films using colliding laser produced plasmas. Further investigations into materials deposition using colliding plasmas performed as part of this project have shown an ability to increase the number density of nano-particles deposited on a substrate compared to that from a single plume (*cf.* Section 5.4.2). Also as part of this work, analysis of the ion emission from colliding plasmas using a Faraday cup reveal real possibilities for applying colliding plasmas as a new source of laser generated ions (*cf.* Section 5.4.1). The ion time of flight distribution from colliding plasmas displays a narrower, more symmetric profile with a higher peak signal (≈ 3X) than a single laser produced plasma. With so many wide and varied potential areas where colliding plasmas can make a significant impact

in future applications, both fundamental research into the properties of colliding plasmas and also research into the applications of colliding plasmas is of particular interest thereby providing a solid motivation for the work presented in this thesis.

Colliding laser produced plasmas are created when a single laser beam is split into two beams and then focused to two points on a target thereby creating two laser produced plasmas separated by a fixed distance (usually 1-10 mm). These two plasmas are referred to as the "seed" plasmas. The seed plasmas freely expand until they start to collide over a region of space at the interface between the two plasmas. Under appropriate conditions, as outlined by Rambo *et al.* [16], a layer of plasma is formed at the collision front between the two counter-propagating plasmas. Far from these conditions the colliding plasmas can undergo significant interpenetration where the plasmas pass through each other without any evidence of stagnation occurring. Rambo *et al.* [16] introduced the so called "collisionality parameter," ξ, to determine whether stagnation or interpenetration dominates the interaction between a pair of colliding plasmas. The collisionality parameter is given by

$$\xi = \frac{L}{\lambda_{ii}} \qquad \text{I.1}$$

where L is the typical plasma dimension (i.e. the separation between the two colliding plasmas) and λ_{ii} is the ion-ion mean free path given by [17]

$$\lambda_{ii} = \frac{m_i^2 v_{12}^4}{4\pi e^4 Z^4 n_i \ln \Lambda_{12}} \qquad \text{I.2}$$

where m_i is the ion mass, v_{12} is the relative collision velocity of the ions from each of the plumes, e is the electronic charge, Z is the average ionization state of the plasma, n_i is the average plasma ion density, and $\ln\Lambda_{12}$ is the so-called Coulomb logarithm [18] for

collisions between seed plasma 1 and seed plasma 2. Inserting values of the parameters typical of experiments presented in this thesis ($n_i = 10^{18}$ cm^{-3}, $Z = 2$, $\nu_{12} = 4 \times 10^6$ cms^{-1}) one obtains a value of 270 for the collisionality parameter and so the plasmas in this thesis are in the strong collisionality or 'hard stagnation' regime [16].

In a colliding plasmas system, the higher the value of the collisionality parameter, the more likely it is that stagnation will occur at the interface between the two plasmas. Changing the collisionality of the colliding plasmas system can be preformed experimentally by a number of ways. Two of the most important of these are, firstly, by changing the separation between the two plasmas and secondly, changing ion number density in the plumes (*e.g. via* changing the on-target irradiance). In fact, by examining equations I.1 and I.2, one can readily see that low density, high velocity colliding plasmas will tend to interpenetrate where as high density, low velocity colliding plasmas will tend to stagnate. Figure I.1 highlights how the collisionality parameter varies with ion density (figure I.1 a) and with relative collision velocity (figure I.1 b) for the experimental parameters given above. The red line indicates the parameters for the colliding plasmas presented in this thesis.

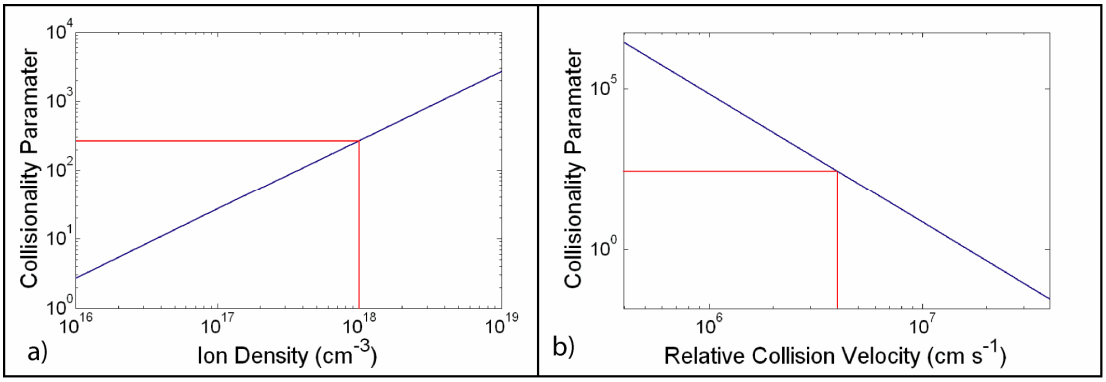

Figure I.1: a) Variation of collisionality parameter with ion density. b) Variation of collisionality parameter with relative collision velocity. The red lines indicate the values of the parameters for the colliding plasmas presented in this thesis.

It is clear from figure I.1 a) that as the ion density rises for a given velocity, so to does the probability of stagnation. This can be explained by the fact that with higher

densities, one increases the probability of collisions occurring leading to a reduction in λ_{ii} and, ultimately, stagnation at the interface between the colliding plasmas. On the other hand, looking at figure I.1 b), it is clear that as the velocity rises for a given ion density, the probability of stagnation decreases. This can be understood from the fact that as the velocity increases, the probability of the ions occupying the same region of space long enough for a collision to happen decreases. For both of these processes, the collisionality parameter provides a good measure of stagnation, where higher values indicate increased probability of stagnation.

The physical process of stagnation layer formation has been found to be very complex. For example, Pollaine *et al.* [19] have shown that plasma stagnation can be preceded by a phase of interpenetration where the plasmas initially pass through each other. Rancu *et al.* [20] also found that interpenetration and stagnation in colliding laser exploded Al/Al and Al/Mg foils is highly dependent on the collisionality parameter. In this thesis it is shown that separation of charge in space can play a significant role in stagnation of various plasma constituents (*cf.* Section 4.3, [13]) where, specifically, we found that electrons stagnate before ions and similarly, ions stagnate before neutral atoms.

With many simultaneous and complex processes involved, it is critical that comprehensive diagnostics of the seed plasmas and the stagnation layer are performed to obtain a more complete picture of the physical nature of colliding plasmas and the mechanisms of stagnation. The diagnostics can also provide extremely useful reference data for colliding plasma modelling efforts [16] especially for colliding plasmas in the soft stagnation regime. This need for further data on colliding plasmas, especially in the critical early or nascent stagnation stage, provided further motivation for the conducting the studies presented in this thesis.

Over the years, a variety of different diagnostic techniques have been employed to study the interaction of colliding plasmas since first produced by Rumsby *et al.* in 1974 [21]. In that study they investigated the interaction of two laterally colliding laser produced carbon plasmas using time-integrated imaging and photon scattering techniques. Several years passed before research on colliding plasmas by Rumsby *et al.* [21] was extended when Begimkulov *et al.* [22] studied the interaction of laterally colliding aluminium or beryllium plasmas using time and wavelength integrated imaging as well as spectroheliography to track the spatial distribution of selected ion stages.

Shortly after the work of Begimkulov *et al.*, Vick *et al.* [23] utilised an X-ray pinhole camera together with an X-ray spectrometer to study colliding aluminium plasmas. In their study, they utilised a 2-D single fluid hydrodynamic code (IZANAMI) to model the conditions of their experiment and showed good agreement with their experimental results revealing the stagnation of the colliding plasmas in nonirradiated regions.

Later eXtreme UltraViolet (XUV) spectroscopy of colliding plasmas was initiated by a group in the Institut fur Experimentaphysik Ruhr-Universat in Bochum Germany and results were first published by Ruhl *et al.* [24]. In their study they utilised time-integrated XUV spectroscopy of the collision region between two colliding carbon plasmas. They observed an increase in emission from the C (VI) Balmer-alpha line compared to single plasma emission and attributed the observation to charge-exchange collisions during the collisional interactions. Shortly afterwards, the same group were also the first to utilise time-integrated VUV spectroscopy to study the lateral collision of two boron-nitride plasmas [25] and again observed evidence of charge-exchange between fully ionised boron and B (III) ions.

Harilal *et al.* [26], again from the group in Bochum, was the first to utilise time resolved XUV pinhole imaging to track the interaction of two colliding laser produced magnesium plasmas. The interactions were studied for laterally and orthogonally colliding laser produced plasmas and it was found that a good deal of interpenetration occurred between the plasmas colliding orthogonally compared to the laterally colliding case.

One of the first major studies into the properties of the stagnation layer using space- and time-resolved visible imaging and spectroscopy was published in 2007 by Luna *et al.* [27]. In that study they used visible emission spectroscopy to extract the temperature and density profile along the stagnation layer at relatively late times (≥ 300 ns). In more recent times, laser based probes, in particular, laser interferometery have been employed to study the interaction of colliding plasmas. One of the first of these studies was conducted by Purvis *et al.* [28] where they utilised soft X-ray laser interferometry to diagnose colliding plasmas created in semi-cylindrical cavities. These experiments were performed using high intensity pump lasers (10^{12} W cm^{-2}) combined with a soft X-ray probe laser and the experiments were aimed at developing X-ray laser interferometry as a diagnostic tool for laser fusion studies. Gregory *et al.* [9] also utilised laser interferometry as a diagnostic tool to study the interaction of two colliding laser produced plasmas with the aim of creating plasma jets for which the relevant scaling parameters showed significant overlap with outflows associated with Young Stellar Objects (YSOs). Finally, Velso *et al.* [29] investigated the properties of laser produced annular plasmas using both laser schlieren imaging and laser interferometry techniques.

Despite the significant body of work that has been published on colliding plasmas to date, summarised above, the number of investigations on colliding plasmas is dwarfed by that performed on single laser produced plasmas. In particular, up until recently, there was a paucity in the published literature on optical diagnostics (such as

fast imaging, optical emission spectroscopy, optical laser interferometry) of colliding plasmas (especially at early times i.e. <100ns and for laboratory scale plasmas). This was uppermost in our thinking when deciding on the various plasma diagnostic techniques to be used during the project as we aimed to fill this knowledge gap.

In addition, the work was also intended to extend an early study at DCU by Luna *et al.* [27] who investigated the properties of the stagnation layer at mid to late times in the lifecycle of the seed plasmas using visible emission spectroscopy. For this reason, it was decided to avail of plasma diagnostic techniques that could elucidate the properties of colliding plasmas at early times (< 100 ns). Consequently, laser interferometry was the first diagnostic technique to be chosen for these studies as it could provide values the electron density of the plasma at early times.

Visible fast imaging was also utilised, in addition to laser interferometry, to investigate the spatial distribution of atoms and ions in colliding plasmas. Optical emission spectroscopy was utilised briefly during the course project to reveal spatial distribution of neutral atoms and ions in the stagnation layer at relatively early times (≈ 80 ns).

A Faraday cup electrical probe was the final diagnostic to be utilised to investigate the properties of ions emitted from the colliding laser produced plasmas and compare them to those emitted from single plumes. This diagnostic technique was chosen as it can effectively and rapidly measure the distribution of the kinetic energies of the ions emitted from the plasmas and so is well suited for investigating ion emission from colliding plasmas.

Finally it is worth noting that, in this work we have concentrated on studying colliding plasmas created with nanosecond tabletop laser sources which are likely to impact routine and wide scale applications in materials science, analytical science, EUV

and X-ray light sources. This is mostly due to their ease of use and cost competitiveness (compared to short pulse or high intensity laser systems) and also concomitantly wide availability. The advent of cheap and widely available pulsed high power fiber lasers are set to accelerate applications and their deployment in industrial, medical and analytical environments further over the coming decade.

To conclude, figure I.2 shows an example of two laterally colliding Al plasmas formed on a flat slab target with the stagnation layer visible at the interface or collision plane. The image was taken during the course of the work presented in this thesis. The field of view of the image was 3.84 mm X 3.84 mm and it was recorded 50 ns after creation of the seed plasmas with an exposure time of 3 ns. The energy carried in each laser pulse of 6 ns (FWHM) duration was 300 mJ and the laser beams were focused onto a flat aluminium target separated by a distance of 1.3 mm. The diameter of each focal spot was 100 μm.

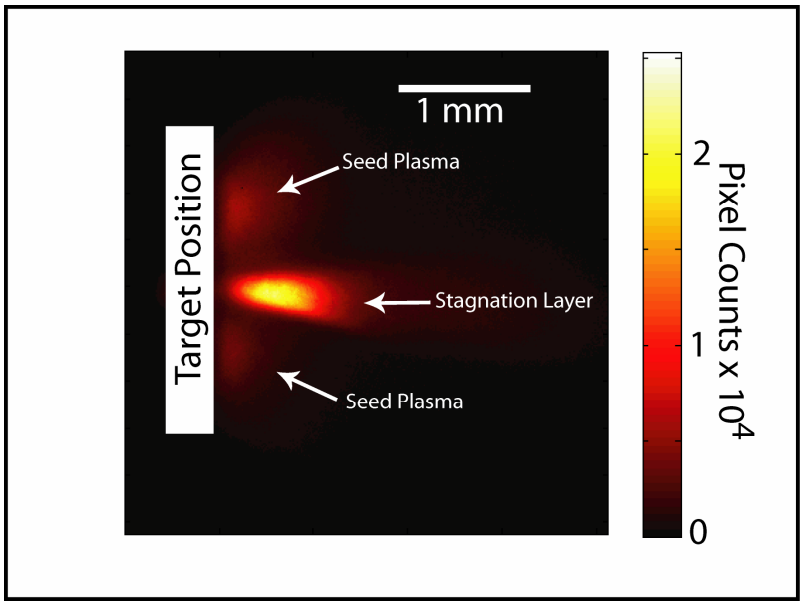

Figure I.2: Image of colliding laser produced aluminium plasmas and stagnation layer captured 50 ns after creation of the seed plasmas. Each seed plasmas was created with a laser beam with an energy of 300 mJ, a wavelength of 1064 nm and a pulse-width of 6 ns, focused to two spots of diameter 100 μm separated by a distance of 1.3 mm.

References

[1] S. A. Ramsden, W. E. R. Davies, Radiation Scattered from the Plasma Produced by a Focused Ruby Laser Beam, *Physical Review Letters*, **13**, 227 (1964).

[2] R. O'Haire, E. McGlynn, M. O. Henry and J. P. Mosnier, ZnO Nanostructured Thin Films Grown by Pulsed Laser Deposition in Mixed O_2/Ar Background Gas, *Superlattices and Microstructures*, **42**, 468 (2007).

[3] P. Hayden, A. Cummings, N. Murphy, G. O'Sullivan, P. Sheridan, J. White, P. Dunne, 13.5 nm Extreme Ultraviolet Emission from Tin Based Laser Produced Plasma Sources, *Journal of Applied Physics*, **99**, 093302 (2006).

[4] S. V. Bulanov, T. Z. Esirkepov, F. F. Kamenets, Y. Kato, A. V. Kuznetsov, K. Nishihara, F. Pegoraro, T. Tajima, V. S. Khoroshkov, Generation of High-quality Charged Particle Beams During the Acceleration of Ions by High-power Laser Radiation, *Plasma Physics Reports*, **28**, 975 (2002).

[5] T. R. Dittrich, S. W. Haan, M. M. Marinak. S. M. Pollaine, D. E. Hinkel, D. H. Munro, C. P. Verdon, G. L. Strobel, R. McEachern, R. C. Cook, C. C. Roberts, D. C. Wilson, P. A. Bradley, L. R. Foreman, and W. S. Varnum, Review of Indirect-drive Ignition Design Options for the National Ignition Facility, *Physics of Plasmas*, **6**, 2164 (1999).

[6] C. Pasquini, J. Cortez, L. M. C. Silva, F. B. Gonzaga, Laser Induced Breakdown Spectroscopy, *Journal of the Brazilian Chemical Society*, **18**, 463 (2007).

[7] M. A. Khater, J. T. Costello, E. T. Kennedy, Optimization of the Emission Characteristics of Laser-produced Steel Plasmas in the Vacuum Ultraviolet: Significant Improvements in Carbon Detection Limits, *Applied Spectroscopy*, **56**, 970 (2002).

[8] U. Willer, M. Saraji, A. Khorsandi, P. Geiser, W. Schade, Near- and mid-infrared laser monitoring of industrial processes, environment and security applications, Optics and Lasers in Engineering, **44**, 699-710 (2006).

[9] C. D. Gregory, J. Howe, B. Loupias, S. Myers, M. M. Notley, Y. Sakawa, A. Oya, R. Kodama, M. Koenig and N. C. Woolsey, Astrophysical Jet Experiments with Colliding Laser-Produced Plasmas, *The Astrophysical Journal*, **676**, 420-426 (2008).

[10] R. A. Smith, J. Lazarus, M. Hohenberger, A. Marocchino, J. A. Robinson, J. P. Chittenden, A. S. Moore, E. T. Gumbrell and M. Dunne, High Resolution Imaging of Colliding Blast Waves in Cluster Media, *Plasma Physics and Controlled Fusion*, **49**, B117-B124 (2007).

[11] B. A. Remington, S. W. Haan, S. G. Glendinning, J. D. Kilkenny, D. H. Munro and R. J. Wallace, Large Growth, Planar Rayleigh-Taylor Experiments on Nova, *Physics of Fluids B*, **4**, 4, (1992).

[12] A. Murphy, J. S. Hirsch, D. Kilbane, E. T. Kennedy, M. A. Khater J-P. Mosnier, A. Neogi, G. O'Sullivan, C. L. S. Lewis, S. Topping, R. Clarke, E. Divall, P. Foster, C. Hooker, A. Langley, D. Neely, P. Dunne, and J. T. Costello, *Proceedings of the Society of Photo-Optical Instrumentation Engineers (SPIE)*, **4876**, 1196-1203, (2003).

[13] P. Dunne, G. O'Sullivan, and D. O'Reilly, Prepulse-enhanced Narrow Bandwidth Soft X-ray Emission from a Low Debris, Subnanosecond, Laser Plasma Source, *Applied Physics Letters*, **76**, 34 (2000).

[14] V. I. Babushok, F. C. DeLucia, J. L. Gottfried, C. A. Munson, A. W. Miziolek Double Pulse Laser Ablation and Plasma: Laser Induced Breakdown Spectroscopy Signal Enhancement, *Spectrochimica Acta Part B-Atomic Spectroscopy*, **61**, 999 (2006).

[15] E. Irissou, F. Vidal, T. Johnston, M. Chaker, D. Guay and A. N. Ryabinin, Influence of an Inert Background Gas on Bimetallic Cross-beam Pulsed Laser Deposition, *Journal of Applied Physics*, **99**, 034904 (2006).

[16] P. W. Rambo and J. Denavit, Interpenetration and Ion Separation in Colliding Plasmas, *Physics of Plasmas*, **1**, (12), 4050-4060 (1994).

[17] C. Chenais-Popovics, P. Renaudin, O. Rancu, F. Gilleron, J.-C. Gauthier, O Larroche, O. Peyrusse, M. Dirksmöller, P. Sondhauss, T. Missalla, I. Uschmann, E. Förster, O. Renner and E. Krousk, Kinetic to Thermal Energy Transfer and Interpenetration in the Collision of Laser-Produced Plasmas, *Physics of Plasmas*, **4**, 190-208 (1997).

[18] J. D. Huba. Naval Reseach Laboratory: Plasma Formulary. http://www.ppd.nrl.navy.mil/nrlformulary/, Naval Research Laboratory, Washington, DC 20375, Revised Edition (2004).

[19] S. M. Pollaine, R. L. Berger, C. J. Keane, Stagnation And Interpenetration of Laser-Created Colliding Plasmas, *Physics of Fluids B-Plasma Physics*, **4**, 989-991 (1992).

[20] O Rancu, P. Renaudin, C. Chenais-Popovics, H. Kawagashi, J.-C. Gauthier, M. Dirksmöller, T. Missalla, I. Uschmann, E. Förster, O. Larroche, O. Peyrusse, O. Renner, E. Krousky, H. Pépin and T. Shepard, Experimental Evidence of Interpenetration and High Ion Temperature in Colliding Plasmas, *Physical Review Letters*, **75**, 3854-3857 (1995).

[21] P. T. Rumsby, J. W. M. Paul, M. M. Masoud, Interactions Between two Colliding Laser Produced Plasmas, *Plasma Physics*, **16**, 969 – 975, (1974).

[22] U. Sh. Begimkulov, B. A. Bryunetkin, V. M. Dyakin, G. A. Koldashov, A. Yu. Repin, E. L. Stupitsky and A. Ya. Faenov, Interaction of Laser-produced Plasma Clouds

in Vacuum and Background Medium, *Journal of Physics D: Applied Physics*, **25**, 1583-1590, (1992).

[23] D. Vick, M. Kado, H. Yamamoto, A. Nishiguchi, K. A. Tanaka, K. A. Tanaka, A. A. Offenberger, C. E. Capjack and S. Nakai, Hydrodynamics of Collisional Structures in Laser-Produced Plasmas, *Physics Review E*, **48**, 3, 2308-2311, (1993).

[24] F. Ruhl, L. Aschke and H.-J. Kunze, Selective Population of the n=3 Level of Hhydrogen-like Carbon in Two Colliding Laser-Produced Plasmas, *Physics Letters A*, **225**, 102-107, (1998).

[25] V. Henc-Bartolic, Z. Andreic, D. Gracin, L. Aschke, F. Ruhl and H.-J. Kunze, Spectral Line Enhancement in Laterally Colliding Boron-Nitride Plasmas, *Physica Scripta*, **T75**, 279-299, (1998).

[26] S. S. Harilal, C. V. Bindhu and H.-J. Kunze, Time Evolution of Colliding Laser Produced Magnesium Plasmas Investigated Using a Pinhole Camera, *Journal of Applied Physics*, **89**, 9, 4737-4740 (2001).

[27] H. Luna, K. D. Kavanagh and J. T. Costello, Study of a Colliding Laser-Produced Plasma by Analysis of Time- and Space-Resolved Image Spectra, *Journal of Applied Physics*, **101**, 033302 (2007).

[28] M. Purvis, J. Grava, J. Filevich, M. C. Marconi, J. Dunn, S. J. Moon, V. N. Shlyaptesv, E. Jankowska and J. J. Rocca, Dynamics of Converging Laser-Created Plasmas in Semicylindrical Cavities Studied Using Soft X-ray Laser Interferometry, *Physical Review E*, **76**, 046402 (2007).

[29] F. Velso, H. Chuaqui, R. Aliaga-Rossel, M. Favre, I. H. Mitchell and E. Wyndham, Laser-Produced Annular Plasmas, *Review of Scientific Instruments*, **77**, 063506 (2006).

List of Figures

List of Tables

Chapter 1:

Orientation

A brief introduction to the properties and current/potential applications of colliding laser generated plasmas has already been described along with the main motivations for conducting the research presented in this work. A brief history of the main research performed to date on the properties of colliding plasmas was also presented.

This chapter aims to provide an orientation around the fundamental properties of plasmas in general and principles of plasma generation with high power lasers. The key atomic processes prevalent in laser produced plasmas are also summarised along with the main plasma expansion and plasma equilibrium models employed to describe laser produced plasmas. The underlying concepts behind the operation of the various plasma diagnostic techniques that were employed during this work is included and the chapter ends with a summary of the principles and characteristics of colliding laser generated plasmas.

1.1: Plasma Definition

Plasma is recognised as the 4^{th} state of matter. It is distinguished from solids, liquids and gases by the fact that it is in a state of partial or complete ionisation. Thus, in its simplest form, a plasma is a gaseous – like assembly of electrons, ions and (not

necessarily, however) neutral atoms. Laser produced plasmas are formed when a high power laser interacts with matter, for example, by focussing a high power laser onto the surface of a solid target or into a gas at high pressure. The laser ionises the matter and creates a plasma plume that subsequently expands outwards into the surrounding environment.

A very important attribute that plasmas possess is that the bulk plasma is overall electrically neutral. This is defined by the expression [1]

$$n_e = \sum_z n_z Z \qquad 1.1$$

where n_e is the electron density, n_z is the density of ions of charge Z.

In a plasma the electrons will tend to accumulate at and surround a positively charge ion and therefore they will tend to shield the electric field from that charge preventing it from penetrating the local plasma environment. One of the fundamental properties of a plasma is the distance over which the electric field from such a charge is shielded. This distance is known as the Debye length, λ_D, and is given by [2]

$$\lambda_D = \sqrt{\frac{\varepsilon_0 k_B T_e}{e^2 n_e}} = 7.43\times10^3 \sqrt{\frac{T_e}{n_e}} \qquad 1.2$$

where ε_0 is the permittivity of free space, k_B is the Boltzmann constant, T_e is the plasma temperature (in kelvin), e is the electron charge and n_e is the electron density.

An extension of the Debye length is the Debye sphere, i.e. the sphere with a radius equal to the Debye length, outside which the electric field of the enclosed charge is zero (fully shielded). The number of electrons, N_{De}, inside the Debye sphere is then given by [3]

$$N_{De} = \frac{4\pi n_e}{3} \lambda_D^3 \qquad 1.3$$

A perturbation of a charged particle in the plasma (by e.g., displacing it from its equilibrium position) will immediately affect its neighbours. This collective response of charged ions and/or electrons is an important defining characteristic of a plasma and pertains only when the length of the plasma is considerably greater than the debye length [1], $L >> \lambda_D$.

The collective response of the plasma manifests itself as a wave–like motion of the particles within the plasma. If by some mechanism the electrons are displaced by a small distance, the electrons will tend to move back to their equilibrium positions. The equation of motion of the electrons is found to have an oscillatory solution corresponding to the collective motion of the electrons. This so called electron wave oscillates with a frequency, ω_p, given by [1]

$$\omega_p = \left(\frac{n_e e^2}{m_e \varepsilon_0} \right)^{\frac{1}{2}} \qquad 1.4$$

If an electromagnetic wave (with frequency ω) propagates through the plasma, it will be subjected to a dispersion which is dependent on the electron density. The dispersion relation for an electromagnetic wave travelling through a plasma is given by [1]

$$\omega^2 = \omega_p^2 + c^2 k^2 \qquad 1.5$$

where ω_p, is the plasma frequency, c is the speed of light and $k=2\pi/\lambda$ is the propagation constant of the wave. Clearly, from equation 1.5, for $\omega > \omega_p$, k is real and the wave propagates through the plasma. However, for $\omega < \omega_p$, k is imaginary and the

wave does not propagate through the plasma. By setting $\omega = \omega_p$ and using equation 1.4 one can determine that the electron density of the plasma at which the electromagnetic wave no longer propagates is given by

$$n_c = \frac{\omega^2 m_e \varepsilon_0}{e^2} \qquad 1.6$$

This value is known as the critical density and for a CO_2 laser (with a wavelength of 10.6 μm), the critical density is approximately 10^{19} cm^{-3} while for a Nd:YAG laser (with a wavelength of 1.064 μm) it is ca. 10^{21} cm^{-3}. The critical density is a crucial parameter when considering the interactions of high power lasers with matter.

1.2: The Interaction of High Power Lasers with Matter

When a high power laser beam is tightly focussed onto the surface of a solid target a laser produced plasma is created. In this thesis high power laser beams are defined as those delivering pulses with energies typically between 0.1 and several joules in a few nanoseconds (typically < 10 ns). Focused to a spot with a diameter of ≈ 100 μm, the irradiance achieved is in the region of 10^{10} – 10^{11} W cm^{-2}. The laser produced plasmas so formed have some very specific features including:

- High temperature (electron temperatures up to 100 eV).
- High density (electron densities of ≈ 10^{18} – 10^{21} cm^{-3})
- Relatively high degree of ionisation of material, up to 20 times ionized (depending on irradiance, material *etc.*)
- High expansion velocities (ion velocities of ≈ 10^6 - 10^7 cm s^{-1})

The laser produced plasma evolves on a very short timescale and has a lifetime of a few microseconds (in the sense that one can still observe the remnants of photon and ion emission in the vicinity of original plasma core). The lifetime of plasmas of interest here is divided up into three main stages which are as follows:

1. Early-life – i.e. from initiation up to approximately one hundred nanoseconds (0-100 ns)
2. Mid-life – i.e. one to a few hundred nanoseconds (100 – 1000 ns)
3. Late-life – i.e. typically one to a few microseconds (1 – 10 μs)

When the laser radiation first reaches the target, it only penetrates to a very short depth (typically less than one optical wavelength). The actual initial interaction between the laser radiation and the target occurs over a very thin layer close to the surface of the target referred to as the skin depth, δ, given by [4]

$$\delta = (\pi \nu \mu_0 \sigma')^{-1/2} \qquad 1.7$$

where ν is the frequency of the incident laser radiation, σ' is the conductivity of the target material and μ_0 is the permeability of vacuum ($\mu_0 = 4\pi \times 10^{-7}$ N A^{-2}).

In the case of aluminium, having a conductivity of 3.767×10^7 S m^{-1} and irradiated with an Nd:YAG laser working at its fundamental frequency of 2.819×10^{14} Hz, the skin depth given by equation 1.7 is $\delta \approx 5$ nm – a very small fraction of the 1064 nm irradiating laser wavelength. Even so the electric field is high enough to interact strongly with the conduction electrons which results in rapid heating, evaporation and ionisation of the electrons thereby creating the initial or primary dilute plasma. The maximum electric, E_{max}, and magnetic fields, B_{max}, of the laser in vacuum are related to the laser irradiance, I_L, by [3],

$$E_{\max}\left(\frac{V}{cm}\right) \cong 2.75\times10^{9}\left(\frac{I_L}{10^{16}W/cm^2}\right)^{\frac{1}{2}} \quad 1.8$$

$$B_{\max}(Gauss) \cong 9.2\times10^{6}\left(\frac{I_L}{10^{16}W/cm^2}\right)^{\frac{1}{2}} \quad 1.9$$

For a Nd:YAG laser (as utilised in these studies) with 0.8 J per pulse and a pulse width of 6 ns focussed to a spotsize of 100 μm, the laser irradiance is found to be $I_L \approx 4.24 \times 10^{11}$ W cm^{-2}. The maximum electric and magnetic fields are calculated to be, $E_{max} \approx 1.8 \times 10^{7}$ V cm^{-1} and $B_{max} \approx 6 \times 10^{4}$ G (6 T) respectively.

The incoming laser radiation is absorbed by the primary plasma via the inverse Bremsstrahlung process [5, 6] (described in more detail in Section 1.4.3). The absorption of this radiation leads to a gain in the kinetic energy of the liberated electrons. These electrons create further ionization and the electron density rises rapidly. Indeed the density increases so much that after a time the plasma becomes opaque to the laser radiation. The plasma density at which the laser light no longer propagates is called the critical density, n_c, of the plasma given by equation 1.6 above or quite simply by [7]

$$n_c \approx \frac{9.85\times10^{20}}{\lambda_{\mu m}^2} \quad 1.10$$

where $\lambda_{\mu m}$ is the wavelength of the laser light in micrometres.

At or above n_c the laser pulse is therefore prevented from reaching the target surface and creating more plasma. The region of the plasma where the density reaches and even exceeds the critical density is referred to as the critical density layer and is where much of the laser energy is deposited, i.e., the so called deflagration zone (see figure 1.1). This does not prevent the plasma expanding however and the plasma

continues to gain energy and expands rapidly which reduces the density. After some expansion the density of the plasma drops below the critical density and the radiation can once again reach the target surface where it generates more plasma via evaporation and ionization which once again increases the density. This cyclical process repeats right throughout the whole duration of the laser pulse (few nanoseconds typically). A shock front develops that propagates into the target as a reaction to the plasma streaming away from the target when the laser light hits the target [3]. Figure 1.1 depicts this process pictorially.

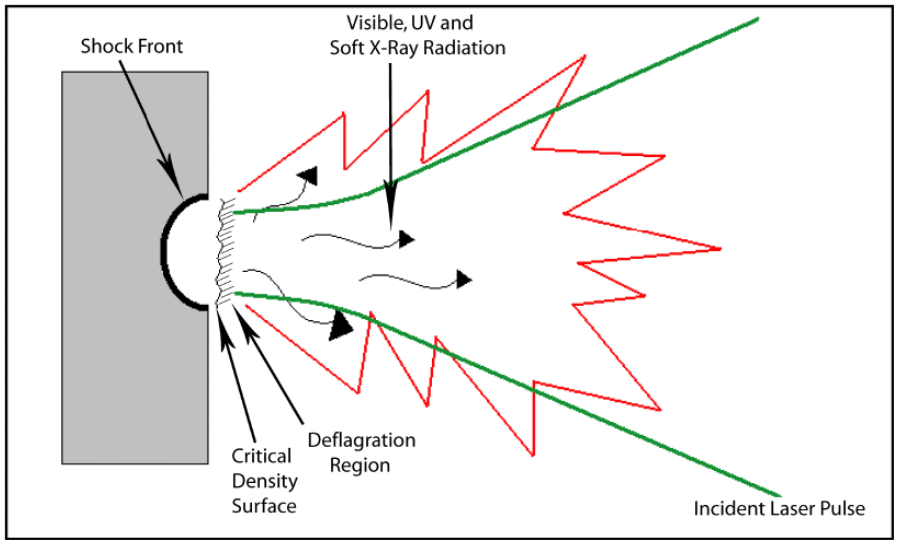

Figure 1.1: Schematic diagram of a laser pulse incident on a solid target creating a laser produced plasma [3].

After the laser pulse terminates, no new plasma is generated and what follows is a rapid expansion of the laser produced plasma plume into the surrounding space where the radiation emitted from the plasma in the early-phase of its lifecycle is mostly continuum. Diagnosis of the plasma is particularly difficult in this phase due to the continuum emission which affects standard plasma spectroscopic diagnostic techniques such as spectral line width analysis and of line intensity ratio analysis from which one can extract the plasma density and temperature respectively. It has been shown, however, that it is possible to gain some information about the plasma at these early times even though the emitted radiation is mainly from continuum emission. For

example, De Luna *et al.* [8] have shown that it was possible to parameterise a laser produced plasma from the analysis of emission line to continuum ratios, however, they have pointed out that the technique is difficult to implement. At mid-lifetimes the density subsides sufficiently so that there is only weak continuum emission and the radiation loss is mainly due to bound-bound transitions from which plasma parameters such as densities and temperatures can be extracted via optical emission spectroscopy or OES.

1.3: Plasma Expansion

When a laser impinges on a solid target a plasma is created. For the duration of the laser pulse, the plasma is said to be *isothermal*. This means that a dynamic equilibrium exists between the plasma absorption coefficient and the rapid transfer of thermal energy to kinetic energy. In the isothermal regime the density, temperature and dimensions of the plasma plume adjusts in such a manner the rate of thermal energy generation via Inverse Bremsstrahlung and collisional excitation is greater than or equal to the rate of loss of thermal energy to the surrounding environment. Assuming so, the expansion of the plasma plume in directions *X, Y, Z* can be described by the equation of isothermal expansion [9]

$$X(t)\left[\frac{1}{t}\frac{dX}{dt}+\frac{d^2X}{dt^2}\right]=Y(t)\left[\frac{1}{t}\frac{dY}{dt}+\frac{d^2Y}{dt^2}\right]=Z(t)\left[\frac{1}{t}\frac{dZ}{dt}+\frac{d^2Z}{dt^2}\right]=\frac{kT_0}{M} \qquad 1.11$$

where the direction *X* is normal to the target surface, *Y* and *Z* are both orthogonal to each other and parallel to the target surface, *k* is the Boltzmann's constant, T_0 is the isothermal temperature of the plasma and *X(t), Y(t), Z(t)* are the plume dimensions as a

function of time. Equation 1.11 holds true only for times less than the duration of the laser pulse.

Once the laser pulse has terminated, the subsequent expansion of the plume can be described as an adiabatic expansion. An adiabatic process here is one where the expansion of the plume happens so rapidly that there is no transfer of heat between the plasma and the surroundings. The plume expands rapidly into the surrounding vacuum and cools as the thermal energy in the plume is converted to kinetic energy. The adiabatic expansion of the plume is also described by Singh and Narayan [9] as

$$X(t)\left[\frac{d^2X}{dt^2}\right] = Y(t)\left[\frac{d^2Y}{dt^2}\right] = Z(t)\left[\frac{d^2Z}{dt^2}\right] = \frac{kT_0}{M}\left[\frac{X_0Y_0Z_0}{X(t)Y(t)Z(t)}\right]^{\gamma-1} \qquad 1.12$$

where γ is the ratio of the specific heat capacities at constant pressure and volume.

Plume front velocities of up to 10^6 cms^{-1} have been observed for plasmas presented in this thesis (Section 4.1) and so the velocity of the plasma species can indeed attain very high values.

As the plasma expands into the surrounding vacuum, the velocity of the electrons can far exceed those of the ions, due to the significant difference in mass between the electron and ions. Consequently the electrons lead the expansion of the plasma plume and hence strong space – charge electric fields (originating from the Coulombic force between the electrons and ions) are created. This will cause the highly charged ions to be accelerated out from the target surface. These space charge separation effects have been observed in single plasmas by various groups worldwide, e.g. Okano *et al.* [10], Ursa *et al.* [11], and are also evident in the colliding plasmas studied during this work (*cf.* Section 4.3 [12]).

1.4: Atomic Processes in Plasmas

Many atomic processes occur in plasmas. These processes commence at the instant that the laser radiation impinges on the target surface creating the plasma, right through to plasma expansion and eventual dissipation into the surrounding environment. When the laser strikes the target, the laser photons can be:

- absorbed by atoms and ions promoting them into excited states (photoabsorption)
- absorbed by atoms and ions resulting in the liberation of electrons into the free-electron continuum (photoionisation)
- absorption by free electrons in the vicinity of ions which results in an increase in kinetic energy of the electrons (inverse-Bremsstrahlung).

After creation of the plasma with the laser, collisional processes (e.g. excitation, recombination) occur in the plasma for the remainder of its life. Table 1.1 summarises the main atomic processes occurring in laser produced plasmas. They are divided into 3 main types of processes, Bound – Bound (B – B), Bound – Free (B – F) and Free – Free (F – F) [13].

Table 1.1: Summary of the main atomic processes that occur in Laser Produced Plasmas

Process	Excitation	De-excitation	Type
B – B	Impact Excitation	Impact De-excitation	Collisional
B – B	Photoabsorption	Spontaneous Decay	Radiative
B – F	Impact Ionisation	3-Body Recombination	Collisional
B – F	Photoionisation	Radiative Recombination	Radiative
F – F	Bremsstrahlung	–	Collisional
F – F	–	Inverse Bremsstrahlung	Radiative

1.4.1: Bound - Bound Processes

Radiative Bound – Bound Processes

There are two situations where bound to bound transitions can occur. Firstly, a bound to bound transition can occur in atoms/ions which have an electron dropping from an excited state to one with lower energy releasing a photon in the process. The energy of the liberated photon is equal to the energy difference of the electron before and after the transition. This process is denoted as *Spontaneous Decay* [13] and analysis of the emitted line spectra is important in many plasma diagnostic techniques. Spontaneous decay can be described by:

$$A^* \rightarrow A + \gamma \qquad 1.13$$

where *A** denotes the atom/ion in an excited state, *A* represents the atom/ion in a lower energy state and γrepresents the photon released during the transition.

Conversely a bound to bound transition can also occur when a photon is absorbed by an electron in a low energy state that is consequently promoted to a state of higher energy. In this case the energy difference of the electron before and after its transition is equal to that of the energy of the photon absorbed. This process is denoted as *Photoabsorption* and can be described by:

$$A + \gamma \rightarrow A^* \qquad 1.14$$

where *A, A** and $\gamma$are as indicated above in equation 1.13. Figure 1.2 depicts these two processes schematically:

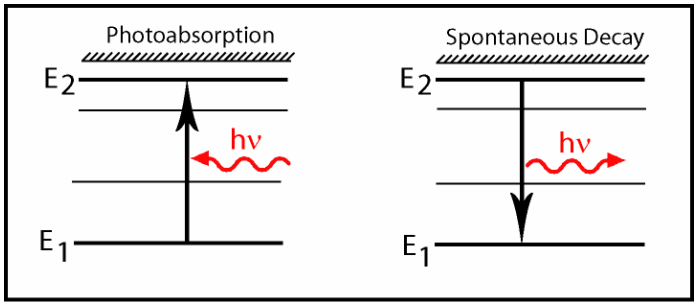

Figure 1.2: Schematic illustration of the photoabsorption (left) and spontaneous decay (right) atomic processes which occur in laser produced plasmas. E_1 and E_2 are lower and upper electron energy states of the atom/ion respectively [13].

Collisional Bound – Bound Processes

In collisional bound – bound processes a bound electron can gain or lose energy i.e., become excited or de-excited after a collision with free electron. *Electron Impact Excitation* occurs when some or all of the kinetic energy of a free electron is transferred to a bound electron exciting it to a higher energy level [13]. The energy gained by the bound electron is equal to the energy lost by the free electron.

Conversely, *Electron Impact De-excitation* occurs when a bound electron in an excited state loses energy and is demoted to a state of lower energy upon collision of the host atom or ion with (usually) a free electron. The kinetic energy of the free electron will be increased by the same amount or quantum of energy that lost by the bound electron in the collision.

The balance equation for these collisional bound to bound processes is given in equation 1.15

$$A + e(\varepsilon_1) \Leftrightarrow A^* + e(\varepsilon_2) \qquad 1.15$$

where *e* denotes the free electron, *A** denotes the atom/ion in an excited state, *A* represents the atom/ion in a lower energy state and ε_1 and ε_2 denote the free electron kinetic energies before and after the collision respectively. Also $\varepsilon_1 > \varepsilon_2$. Reading equation 1.15 from the left-hand side to the right-hand side describes the process of electron-impact excitation, and vice-versa for the case of electron-impact de-excitation (right-to-left)

Figure 1.3 is a simple schematic diagram of the collisional bound – bound atomic processes.

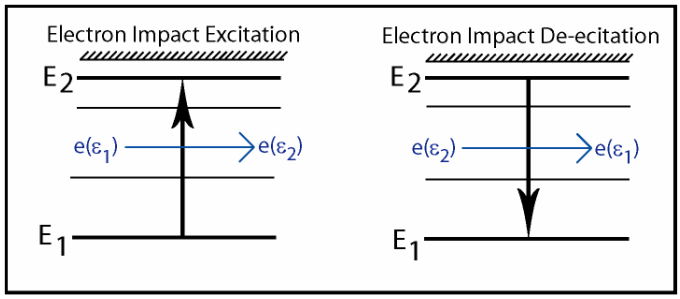

Figure 1.3: Schematic diagram of the electron impact excitation (left) and electron impact de-excitation (right) atomic processes which occur in laser produced plasmas [13].

1.4.2: Bound – Free Processes

Radiative Bound – Free Processes

Bound - free transitions also occur in two ways. First of all when a free electron is in the vicinity of an ion, it can be captured by the ion and consequently recombine with the atom. During the process a photon is released with an energy equal to the energy difference of the electron before and after the transition. This process is called *Radiative Recombination* (RR) [3] and can be described by:

$$e + A^{z+1} \rightarrow A^{z} + \gamma \qquad 1.16$$

where e is the free electron, A^{z+1} and A^{z} represents ions in charge state z+1 and z respectively and $\gamma$is the emitted photon.

The inverse process to Radiative Recombination is the famous photoelectric effect or so called *Photoionisation* [3]. In photoionisation, the absorption of a photon by a bound electron results in the release of the electron into the continuum. The photoelectric is described by:

$$\gamma + A^{z} \rightarrow A^{z+1} + e \qquad 1.17$$

where e, A^{z+1}, A^{z} , and $\gamma$are as already defined. Figure 1.4 illustrates the two bound to free processes.

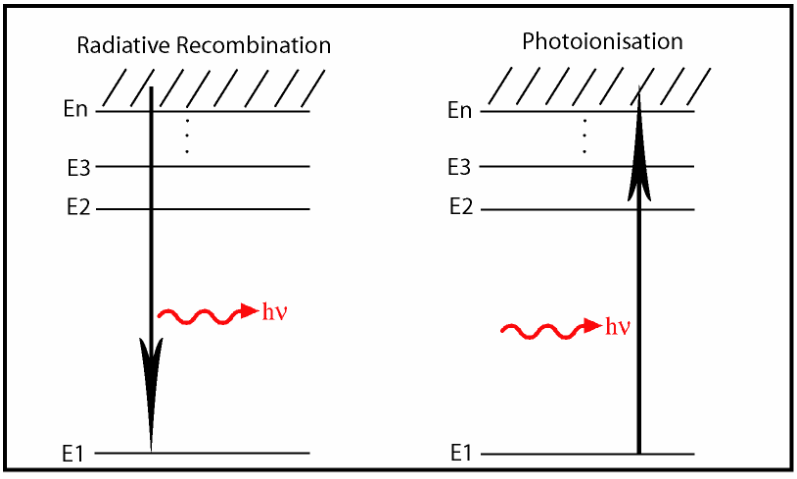

Figure 1.4: Schematic illustration of the Radiative Recombination (left) and Photoionisation (right) atomic processes that occur in laser produced plasmas. E1, E2, E3…En are bound electronic states of the atom/ion [13].

Collisional Bound – Free Processes

When a free electron collides with an atom or ion, enough energy may be transferred from the free electron to a bound electron to overcome the ionisation potential of the atom/ion. The bound electron will then be ionised and enter the free

electron continuum. The energy gained by the bound electron is equal to the energy lost by the free electron. This process is known as *electron impact ionisation* [13] and is described by

$$A^{Z} + e_1 \rightarrow A^{z+1} + e_1^{'} + e_2 \qquad 1.18$$

where A^z and A^{z+1} are as described above, e_1 and $e_1^{'}$ is the free electron before and after (lower energy) the collision and e_2 is the ionised electron.

The inverse of this process is known as *3-body recombination* and usually occurs in high density plasmas where the probability of two electrons entering the debye sphere of an ion becomes relatively high. In 3-body recombination, one free electron is captured into an outer level of an ion. The second electron gains the energy lost by the captured electron. The balance equation for 3-body recombination is given by:

$$A^{z+1} + e(\varepsilon_1) + e_2(\varepsilon_2) \rightarrow A^{z} + e_1(\varepsilon_1^{'}) \qquad 1.19$$

where A^{z+1} is an ion in charged state *z+1*, A^z is the ion in charge state *n*, $e_1(\varepsilon_1)$ and $e_2(\varepsilon_2)$ are the free electrons before the interaction and $e_1(\varepsilon_1^{'})$ is a free electron with increased energy after the capture of the other free electron by the ion. Figure 1.5 illustrates these processes graphically.

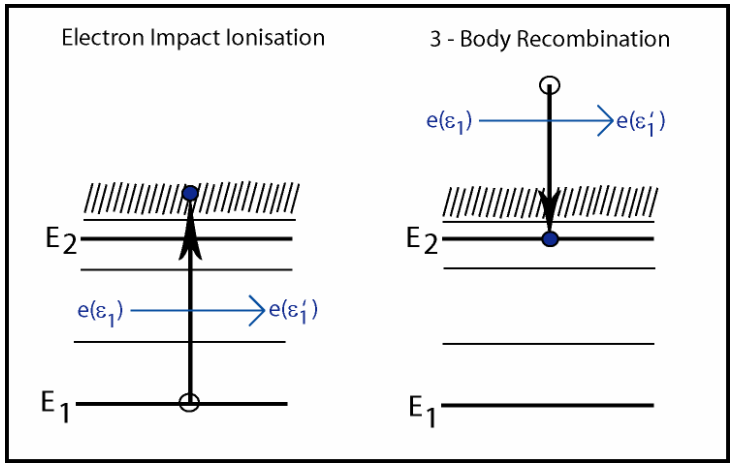

Figure 1.5: Schematic diagram illustrating the electron impact ionisation (left) and 3-body recombination (right) atomic processes that occur in laser produced plasmas [13].

1.4.3: Free – Free Processes

Radiative Free – Free Processes

When a free electron (in the vicinity of a heavy ion) absorbs a photon the kinetic energy of the electron is increased by the quantum of energy absorbed. Because the electron is in the vicinity of the heavy ion, momentum is conserved. This process is called *Inverse Bremsstrahlung* (IB) and plays a major role in laser radiation absorption by a plasma. Inverse Bremsstrahlung is described by [3]:

$$e(\varepsilon_1) + A + \gamma \rightarrow A + e(\varepsilon_2) \qquad 1.20$$

where *e* is the free electron, ε_1 and ε_2 are the energies of the free electron before and after the process, *A* represents the ion and γ is the photon. The inverse Bremsstrahlung process is shown schematically below in figure 1.6.

The corresponding free – free emission process is known as Bremsstrahlung. Bremsstrahlung or 'braking radiation' occurs when an electron is passing through the electric field of an ion (in fact it can happen when passing through any electric field, but for the case of plasmas the field originates from the Coulombic field of an ion in the plasma). The electron may be accelerated in the electric field and thereby emit a photon. Bremsstrahlung can be described by:

$$e(\varepsilon_1) + A \rightarrow e(\varepsilon_2) + A + \gamma \qquad 1.21$$

where e, ε_1, ε_2, A, and γ are defined above.

Figure 1.6 shows the Bremsstrahlung process schematically.

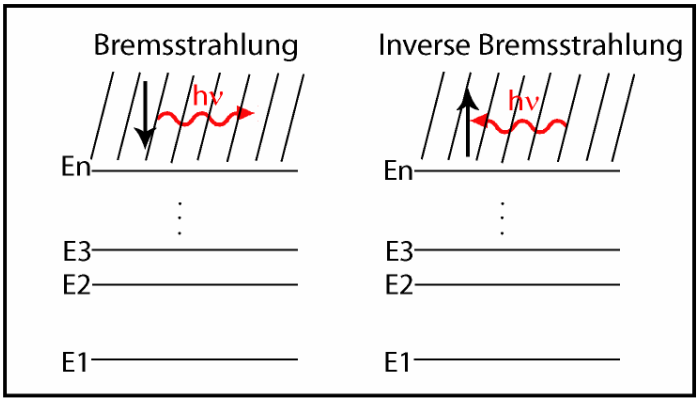

Figure 1.6: Schematic diagram of the Bremsstrahlung (left) and Inverse Bremsstrahlung (right) atomic processes that occur in laser produced plasmas [13].

1.5: Plasma Equilibrium Models

A plasma is said to be in a state of *Complete Thermodynamic equilibrium* (CT) if all of the following conditions (A – D) are satisfied [1]:

A. All particles obey the Maxwell velocity distribution law.

B. The population distributions over the states of any atom or ion are given by the Boltzmann formula.
C. The number of ions in a charge state z relative to the number in state (z-1) is given by the Saha equation.
D. The intensity distribution of the radiation emitted can be described by the Planck radiation distribution function.

In CT plasmas every atomic process occurring in the plasma is balanced by an equal and opposite process, for example the rate of collisional excitation equals the rate of collisional de-excitation. This is the ideal case for a plasma in equilibrium and in fact it is very rare for this to be the case, especially in laboratory plasmas.

Laboratory plasmas rarely approach a state of complete thermodynamic equilibrium. The fact that radiation is emitted from plasmas prevents this from happening. Thus for more practical reasons, equilibrium models have been developed to describe plasmas in different regimes with less stringent prerequisites than those for CT. The 3 most common equilibrium models used to describe plasmas are:

I. Local Thermodynamic Equilibrium
II. Coronal Equilibrium
III. Collisional Radiative Equilibrium

Figure 1.7 [14] illustrates the range of validity of each model for a range of plasma densities and temperatures.

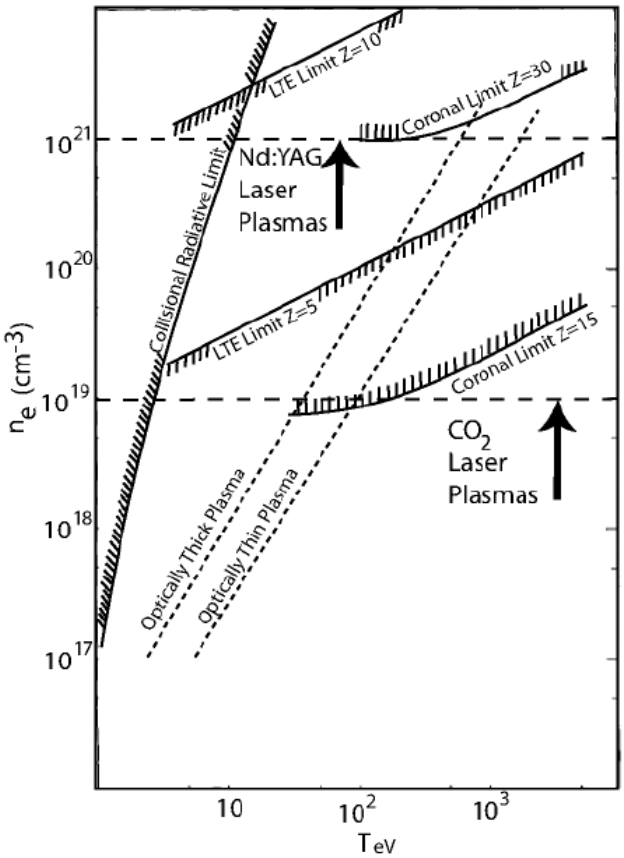

Figure 1.7: Ranges of validity for the application of the different plasma equilibrium models (after Colombant and Tonon, 1973 [14]).

1.5.1: Local Thermodynamic Equilibrium

Local Thermodynamic Equilibrium (LTE) is the name given to describe a plasma in which collisional excitation and de-excitation are the dominant atomic processes. The electron density must be high enough that an ion in an excited state has a greater chance of returning to the ground state through collisional de-excitation than through spontaneous emission. LTE is distinguished from complete thermodynamic equilibrium in that the temperature need not be the same everywhere, and the spectrum is not characteristic of a pure blackbody. Several conditions must hold true for LTE [6, 15, 16]:

- The electron and ion velocity distributions should obey a Maxwell-Boltzmann distribution written as:

$$f(v)dv = 4\pi n_e v^2 \left\{ \frac{m_e}{2\pi k_B T_e} \right\} \exp\left\{ -\frac{m_e v^2}{2k_B T_e} \right\} dv \qquad 1.22$$

where *f(v)* is the density of the electrons with velocity between *v* and *v + dv,* n_e is the electron density and T_e is the electron temperature.

- The plasma dimensions should be much smaller than the mean free path of the emitted photons but larger than the collision length of the electrons and ions.
- The electron density should be high enough so that the ratio between collisional de-excitation and radiative decay should be larger than 10:1 for all transitions. McWhirter [16] derived the following relationship between the electron density and temperature for LTE:

$$n_e \geq 1.6 \times 10^{12} T_e^{\frac{1}{2}} \chi(p,q)^3 \text{ cm}^{-3} \qquad 1.23$$

where T_e is in Kelvin and χ is the energy difference between levels *p* and *q* in electron volts. If we take the example of an Al^+ ion with a transition at 466 nm (2.66 eV) and an electron density of 1×10^{19} cm^{-3}, an electron temperature of $T_e \geq 30$ eV is required for LTE to hold in that particular case.

1.5.2: Coronal Equilibrium

Coronal Equilibrium (CE) is the name given to describe a plasma in which the electron density is too low for LTE to hold so that upward atomic transitions are

assumed to be caused by collisions between electrons and ions and downward transitions occur by spontaneous emission [6], i.e., in CE radiative processes dominate the de-excitation to lower lying levels.

1.5.3: Collisional Radiative Equilibrium

Collisional radiative equilibrium (CRE) is the name given to the model that describes an intermediate state between LTE and CE (typically $n_e \approx 10^{19} - 10^{21}$ cm^{-3}). Here both collisional and radiative processes have to be taken into account [14]. The following conditions must be satisfied in order for CRE to hold:

- The velocity distribution of the electrons must be Maxwellian to ensure that the electron-electron relaxation time is smaller than the electron heating time.
- The population density of ions of charge Z+1 must not change significantly during the period when the quasisteady-state population distribution is being established among the ions of charge Z.
- The plasma must be optically thin to its own radiation.

1.6: Fundamentals of Plasma Diagnostics

In order to fully explore and understand (and eventually exploit for applications) the properties of laser produced plasmas, it is essential to employ diagnostic techniques that can extract critical parameters such as densities, temperatures, velocities, dimensions *etc.* which characterise the laser produced plasma.

After construction of the experimental system, the first experiments concentrated on analysis of single laser produced plasmas. These experiments aimed not only to provide a test and benchmark in preparation for future experiments on colliding plasma but provide useful data on the properties of single plumes at early times in the life of the plasma plume. To this end the experiments concentrated on utilising laser interferometry (which can reveal the 2-dimensional (2D) spatial distribution of electron densities) and laser shadowgraphy (which can visualise the spatial expansion of the plume) to investigate the properties of single plumes expanding into vacuum and variable gaseous atmospheres which is currently of significant in the PLD community who utilise background gases in the growth of materials.

Earlier studies on colliding plasmas in Dublin City University (DCU) [17 - 19] employed techniques such as optical emission spectroscopy to extract the temperatures and densities of the stagnation layer and seed plumes at mid-late times in the life of the plasma. In extending these studies, it was logical to employ diagnostic techniques that could measure the stagnation layer at early times as to elucidate plasma conditions before, at and beyond stagnation, thereby, revealing more detailed information about both the process of stagnation and the properties of the stagnation layer. For this reasons, two main diagnostic techniques were employed during the project, laser interferometry (already well tested and benchmarked on single plumes in the literature) and fast imaging (which, in combination with spectral filtering, can reveal the 2-D spatial distribution of visible emission from neutral atoms and ions).

The project did not exclusively use these techniques, however, and during the project two other diagnostic technique were employed to study the properties of the colliding plasmas. Optical emission spectroscopy was utilised to reveal the spatial distribution of emission from neutral atoms and singly and doubly charged ions in the stagnation layer. Finally, in order to reveal the properties of ion emission from the

colliding plasmas, a Faraday cup was employed which uncovered the distribution of kinetic energies of the ions. What follows is an overview of the fundamental principles of each of the diagnostic techniques employed during the project.

1.6.1: Fast Imaging

Time resolved optical imaging of laser produced plasmas with fast framing cameras has been a useful and widely used diagnostic over the past two decades or so e.g. Harilal *et al.* [20], Siegel *et al.* [21], Whitty *et al.* [22] and Geohegan [23]. Broadband imaging is useful for tracking the whole plasma motion for comparison with the results of single fluid codes such as Medusa [24]. Further refinement via the use of narrow bandpass filters enables one to select the charge state of each individual atomic and/or molecular plasma constituent and so can be useful for comparison with multifluid codes, e.g. Rambo and Denavitt [25] and Jones *et al.* [26]. Indeed, with a sufficiently narrow bandpass, one can even isolate a particular excitation state of the atom or ion, under study.

The high temporal resolution afforded by the use of modern gated-intensified charge coupled device cameras or ICCD's (usually a few nanoseconds) means that specific atomic or ionic constituents in a plasma can be tracked over time and subsequently the images processed to extract important information such as their spatial distributions and velocities. The focus of the fast imaging work presented in this thesis (results described in Chapter 4) is specifically on spectrally resolved imaging of colliding laser produced plasmas. As stated in the introduction, fast imaging enables a comparison of the spatio-temporal evolution of ions before, at and after stagnation. In this work, the spatio-temporal behaviour of Al^+ ions is compared with that of the free electrons for colliding aluminium plasmas. Furthermore, fast imaging can, especially, in

combination with spectroscopy, help to shed light on the populating/depopulating mechanisms for highly excited electronic states in plasmas.

1.6.2: Optical Emission Spectroscopy

Optical Emission Spectroscopy (OES) is a very useful and versatile tool for analysing laser produced plasmas as demonstrated by Shaikh *et al.* [27]. In particular OES can be used to extract temperatures and densities of plasmas at mid to late times during the lifecycle of the plasma.

The width of spectral lines is dominated by so-called Stark broadening effects. Thus for a spectral line with a Stark broadening parameter, w, the width (Full Width at Half Maximum or FWHM), $\Delta\lambda_{FWHM}$, of the broadened line is given by [28]

$$\Delta\lambda_{FWHM} = 2w\left(\frac{n_e}{10^{16}}\right) \qquad 1.24$$

where n_e is the electron density (cm^{-3}).

The electron temperature, T_e, can be extracted from emission spectra by comparing the intensity of spectral lines which originate from consecutive charge states [28]. Assuming a Boltzmann population distribution of the charge states, the ratio of line intensities from successive charge states is described by [28]

$$\frac{I'}{I} = \frac{f'g'\lambda^3}{fg\lambda'^3}(4\pi^{3/2}a_0^3 n_e)^{-1}\left(\frac{kT_e}{E_H}\right)^{3/2}\exp\left(\frac{E-E'-E_\infty}{kT_e}\right) \qquad 1.25$$

where I'/I is the ratio of intensities of the two measured lines and λ, g and f are the wavelength, statistical weight of the lower state of the transition, and absorption oscillator strength, respectively. E and E' are the excitation energies of the transitions of interest in the successive ion stages, while E_∞ and E_H are the ionization energies of the lower of the two apposite ion stages and the hydrogen atom, respectively. The subsequent (higher) ionisation stage is primed in equation 1.25.

Significant work has already been performed at Dublin City University on analysing temperatures and densities of colliding plasmas using OES (e.g. Kavanagh [18] and Dardis [19]). For this reason, OES has not been employed to study temperatures and densities in this thesis. Rather it has been exploited to reveal the spatio – temporal evolution of different of different plasma species (in this study: Al^0, Al^+ and Al^{2+}) in the stagnation layer (*cf.* Section 4.4).

1.6.3: Laser Interferometry

Although OES can yield both densities and temperatures and is especially useful if combined with both space and time resolution [21, 29], it is at its most effective only during the mid-life of a laser produced plasma when there is little or (ideally) no continuum emission that, if present, can overpower the line emission used for analysis [8]. To fully diagnose the interaction region between colliding plasma plumes, a quantitative technique that can "pinpoint" the birth phase of the stagnation region and diagnose the plasma parameters at the same time is required. Laser interferometry is one such solution as it permits an accurate determination of the electron density distribution at early times (<100 ns) in the lifecycle of a laser produced plasma [30]. The basic theory of an interferometer is outlined below [7].

One can express the temporal variation of the electric field vector, *E*, for a wave with a given frequency ω, by equation 1.26 below [31],

$$E = E_0 \exp i\{\omega t\} \qquad 1.26$$

where, ω is the angular frequency of the wave and E_0 is the peak electric field amplitude and E is the instantaneous electric field amplitude.

In a simple two arm interferometer this wave is split into two waves, E_1 and E_2, and then added together after introducing some phase difference, Φ, between them. Assuming that one arm of the interferometer is in vacuum, the value of the refractive index is thus, $n = 1$. After addition of the two waves the total field, E_t, is given by

$$E_t = (E_1 + E_2 \exp i\Phi_1) \exp i\omega t \qquad 1.27$$

The magnitude of the power detected is proportional to $|E_t|^2$,

$$|E_t|^2 = [E_1^2 + E_2^2]\left[1 + \frac{2E_1E_2}{E_1^2 + E_2^2}\cos\Phi\right] \qquad 1.28$$

From equation 1.28, is can be readily seen that the output power of the interferometer has a constant component that depends only on the individual probe beam intensities plus a component that varies as $\cos\Phi$ and therefore an interference pattern is obtained comprising constructively interfering bright and destructively interfering dark fringes. Figure 1.8 is an example of this interference pattern captured using the interferometer constructed in this project.

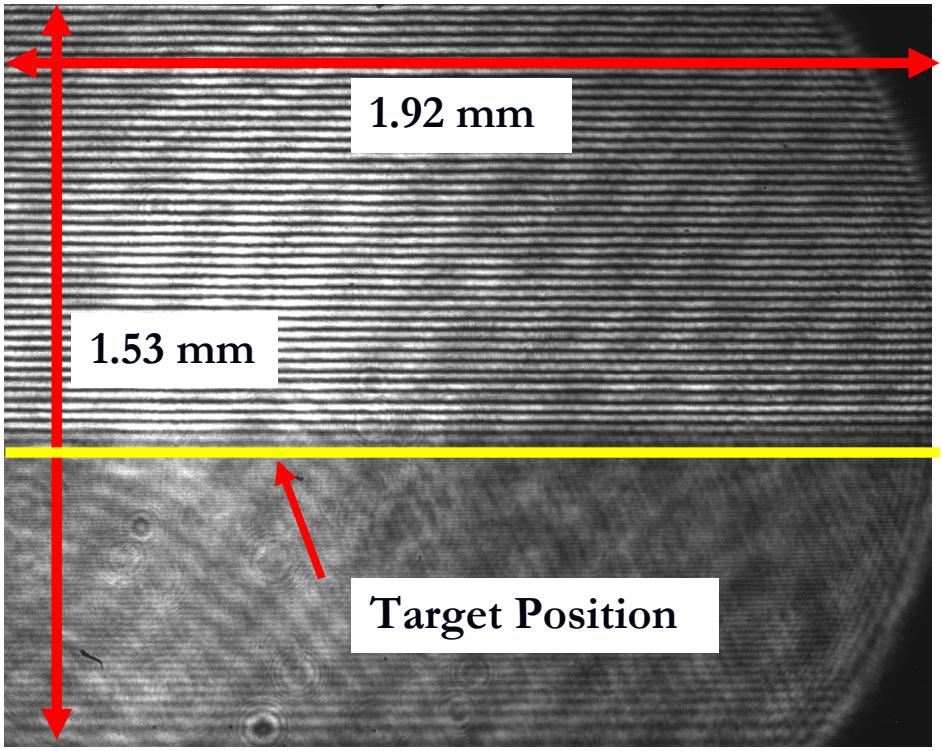

Figure 1.8 Sample interferogram where the modulation in intensity (from equation 1.26) is visible, i.e. the horizontal fringes of light visible in the top half of the interferogram. The yellow line points out the position of the surface of the target. The interference fringes are visible above the target surface.

Consider now what happens if a medium with an unknown refractive index, for example, a laser produced plasma, is introduced into one of the arms of the interferometer. By doing so one acquires an additional phase Φ' in the interferometer which can be computed using the relationship:

$$\Phi' = \int k \cdot dl = \int N \frac{\omega}{c} \cdot dl \qquad 1.29$$

where *k* is the wavenumber of the probe beam along the path of length *l that it takes through the plasma*. Here, *N* is the refractive index of the plasma calculated along the path, *l*. When the ray is travelling outside the plasma (i.e. in vacuum) the wavenumber is denoted by k_0 and *N* = 1, therefore,

$$k_0 = \frac{\omega}{c} \tag{1.30}$$

Of course the interferogram of the plasma also comprises the phase lag Φ, i.e. the integration outside the plasma e.g. to the detector. To extract any information about the plasma, it is necessary to find the phase lag due to the plasma alone.

The phase due to the plasma alone is simply the difference in phases between Φ and Φ' which is denoted by $\Delta\Phi$, given by,

$$\Delta\Phi = \Phi' - \Phi = \int k_{plasma} - k_0 \cdot dl = \int (N-1)\frac{\omega}{c} dl \tag{1.31}$$

This process of subtraction of the phase with no plasma present is known as background subtraction. The phase shift induced by the plasma can now be directly related to the refractive index of the plasma. According to standard plasma theory the refractive index of a plasma is composed of a contribution from free electrons only [7] and is given by,

$$N = \left(1 - \frac{n_e}{n_c}\right)^{\frac{1}{2}} \tag{1.32}$$

where, n_e is the density of free electrons and n_c is the critical density of the plasma where, as already defined in Section 1.2, n_c is given by

$$n_c = \frac{9.85 \times 10^{20}}{\lambda_{\mu m}^2} \tag{1.33}$$

where $\lambda_{\mu m}$ is the wavelength of the light in μm.

Assuming that $n_e << n_c$, a valid assumption in laser produced plasmas, equation 1.32 reduces to

$$N \approx 1 - \frac{1}{2}\left(\frac{n_e}{n_c}\right) \qquad 1.34$$

By substituting equation 1.34 into equation 1.31, the phase shift induced by the presence of a plasma in the arm of an interferometer can be directly related to the number density of free electrons present in the plasma to obtain [7],

$$\Delta\Phi = \frac{-\omega}{2cn_c}\int n_e dl \qquad 1.35$$

Finally with the use of the Abel inversion mathematical technique [32], it is possible to find a solution for calculating the electron density. The electron density is then given by [30],

$$n_e \cong \frac{-\lambda_{\mu m} n_c}{\pi}\int_r^{r_{\max}} \frac{d\Delta\Phi}{dx}(x^2 - r^2)^{-\frac{1}{2}} dx \qquad 1.36$$

where r is the radial distance of the cordial light path through the plasma and x is the propagation distance of the light as depicted in figure 1.9 below,

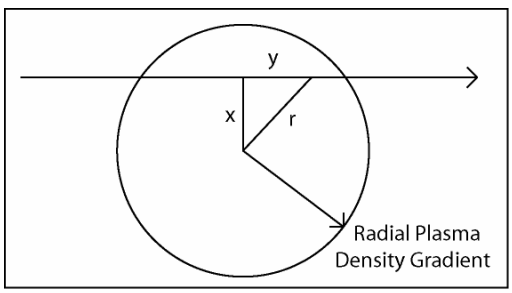

Figure 1.9: Coordinate system for a ray of laser light passing through a cylindrically symmetric plasma [32].

A freely available software package was employed to analyse the interferograms, perform the able inversion technique and extract the electron density profiles. The freeware software package, called IDEA [33], was specially developed for the purpose of analysing interferograms by a group in the Technical University Graz, Austria [34] and is widely utilised in the interferometry community.

1.6.4: Shadowgraphy

Shadowgraphy in its simplest form is the detection of variations in the transmitted intensity of a collimated light beam after it has passed through a (usually) non-uniform medium, for example, a laser produced plasma [35]. The refractive index of the medium results in the deflection of the probe light beam. This is illustrated schematically in figure 1.10 [7].

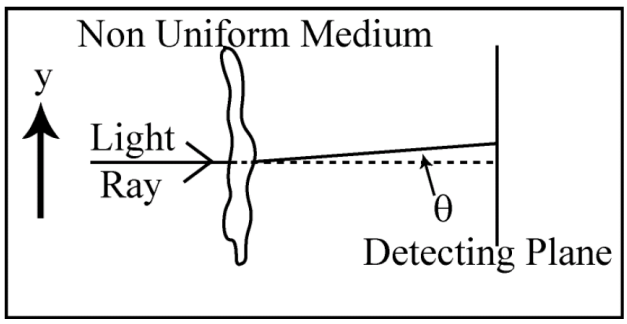

Figure 1.10: Schematic diagram of the angular deflection of a light ray through an angle θ after passing through a non-uniform medium [7].

As already defined in equation 1.29 the phase shift, Φ, induced in a monochromatic light wave along the beam path, *l*, through a plasma is given by

$$\Phi = \int N \frac{\omega}{c} \cdot dl \qquad 1.37$$

As a result, the emerging ray will subtend an angle, θ, with respect to the incident ray, given by [7]

$$\theta(y) = \frac{d\Phi}{dy}\frac{\lambda}{2\pi} = \frac{d}{dy}\left[\int Ndl\right] \qquad 1.38$$

where all of the arguments are as defined above.

So, on passing through the medium the beam is deflected in proportion to the density gradient. If the point at which the ray falls without the medium present is denoted by *y*, then with the medium present it will be moved to a new position *y'* given by the expression:

$$y' = y + L\theta(y) \qquad 1.39$$

where *L* is the distance from the non-uniform medium to the detecting plane.

The same process occurs in the orthogonal direction (i.e. direction into the page in figure 1.10) denoted by the coordinate *x*. Therefore, a light ray incident on a point *(x,y)* at the detection plane will be moved to *(x',y')* in the presence of a non-uniform medium where

$$(x', y') = \left(x + L\frac{d}{dx}\left[\int Ndl\right], y + L\frac{d}{dy}\left[\int Ndl\right]\right) \qquad 1.40$$

If the incident beam intensity is denoted by I_i then the detected intensity I_d will be given by:

$$I_d dx' dy' = I_i dx dy \qquad 1.41$$

Following from equation 1.40 and equation 1.41 [7], one obtains,

$$\frac{I_i}{I_d} = 1 + L\left[\frac{d^2}{dx^2} + \frac{d^2}{dy^2}\right]\left(\int Ndl\right) \qquad 1.42$$

For small fractional intensity variations equation 1.42 becomes

$$\frac{\Delta I_{di}}{I} = L\left[\frac{d^2}{dx^2} + \frac{d^2}{dy^2}\right]\left(\int Ndl\right) \qquad 1.43$$

Thus, for shadowgraphy, a signal proportional to the second derivative of the refractive index of the medium is detected.

In particular, shadowgraphy is very useful when observing the propagation of shock fronts in gaseous atmospheres that are produced when a laser driven plasma is created in the presence of a background gas [36]. The variation of refractive index at the shockfront arises from the compression of the gas which changes the refractive index.

1.6.5: Faraday Cup Probe

The technique of using an electrostatic probe to measure the properties of plasmas was first introduced by Langmuir in the 1920's [37]. Langmuir developed the theory needed to use a metallic probe for analysing collision-less, large volume, steady state plasmas in which the velocities of the ions and electrons can be described by Maxwellian distribution functions. Essentially when a bias voltage is applied to a probe placed in the vicinity of a plasma, the charge is collected across a capacitor (which serves to block the bias voltage and transmit the varying signal current – i.e. the

plasma charge being collected by the probe) which is then registered on an oscilloscope.

The use of an electrostatic probe applied to flowing plasmas was developed further by Koopman [38]. Koopman employed the Langmuir probe together with a self-designed bias circuit, the so called “Koopman bias circuit”, to investigate properties such as electron and ion velocities of a “plasma ball” created with a ruby laser.

The Faraday cup is a variation of the Langmuir electrostatic probe named after Michael Faraday who pioneered investigations of electricity and magnetism in the 1800’s [39]. A Faraday cup is simply a conducting cup shaped device to which a bias voltage is applied. The cup collects charged particles which are registered as a change in current on an oscilloscope. The cup is surrounded by a grounded metal conductor to shield it from electrical noise.

When placed in the path of a laser produced plasma, the Faraday cup can collect the passing electrons or ions (depending on the polarity of the bias voltage). The charged particles are collected by the cup as the plasma expands outward in time and is registered as a change in current on the oscilloscope. By knowing the exact moment the laser strikes the target surface, for example – by using a fast photodiode, the velocity of the particles can be calculated by the distance from target to the Faraday cup divided by the time after the laser is incident on the target as demonstrated, for example, by Harilal *et al.* [40].

The kinetic energy of the particles, E_k, can then be extracted using

$$E_k = \frac{1}{2} m v^2 \qquad 1.44$$

where m is the mass of the charged particle and v is the velocity.

For the case of aluminium ions, which is the case for experiments presented in this thesis, equation 1.44 becomes

$$E_k = \frac{\left(\frac{1}{2} m_{Al} \left(\frac{d}{t}\right)^2\right)}{1.6 \times 10^{-19}} \qquad 1.45$$

where E_k is the kinetic energy of the ions in electronvolts, m_{Al} is the mass of aluminium, d is the distance to the Faraday cup and t is the time to reach the Faraday cup.

Calculating for the time of flight for all the ions reveals the kinetic energy distribution of the ions emitted from the laser produced plasma.

1.7: Fundamentals of Colliding Laser Produced Plasmas

Colliding laser produced plasmas have been a largely unexplored and an especially unexploited research domain until quite recent times despite the fact that first experiments can be traced back to the early 1970s [41].

When a laser beam is split into two parts and focused onto a target, two separate laser produced plasmas are created at each of the two foci. The two plasmas created initially are referred to as the "seed" plasmas. Each of these two laser produced plasmas initially expand as single individual laser produced plasmas up to a certain point after which they start to "sense" each another. At this point two extreme scenarios can potentially occur – they can either interpenetrate or stagnate at the collision midplane. If the plasmas interpenetrate, then the two plasmas just stream through each other with binary collisions dominating. If they stagnate, on the other

hand, a layer of plasma builds up at the interface where the two plasmas collide. This layer of plasma is referred to as the stagnation layer, the location where the density and temperature increases and the velocity drops to make a somewhat uniform (compared to a seed plume) layer of plasma. In practice the situation may be somewhere between these two scenarios, a state which is referred to as "soft stagnation".

The key quantity determining whether interpenetration or stagnation (hard or soft) occurs is the so called collisionality parameter, ζ [25]. It is expressed as the ratio of the experimental scale, *D*, usually taken to be the separation between the two seed plasmas, to the ion – ion mean free path, λ_{ii} [25]:

$$\zeta = \frac{D}{\lambda_{ii}} \qquad 1.46$$

where the ion – ion mean free path is given by [42]:

$$\lambda_{ii} = \frac{m_i^2 v_{12}^2}{4\pi e^4 Z^4 n_i \ln \Lambda_{12}} \qquad 1.47$$

where m_i is the ion mass, v_{12} is the relative collision velocity is the charge of the electron, *Z* is the average ionization state of the plasma, n_i is the average plasma ion density, and $\ln\Lambda_{12}$ is the so-called Coulomb logarithm for collisions between seed plasma 1 and seed plasma 2. The value of the Coulomb logarithm is typically in the range of 10 to 30 for most laboratory plasmas [43].

Since λ_{ii} scales as v_{12}^2, for a given *D*, high temperature – high velocity plasmas will tend to interpenetrate whereas low temperature – low velocity plasmas will tend to stagnate. Figure 1.11 shows a picture of a pair of colliding plasmas and the

stagnation layer created at the interface between the two. The image was captured 40 ns after the creation of the seed plasmas by splitting a 800mJ laser beam and focusing it onto two spots of diameter 100 µm separated by a distance, D, of 1.3 mm. The target used consisted of a flat aluminium slab (99.99% purity). An interference filter with a centre wavelength of 460 nm and a FWHM of 10 nm was used to select emission from the Al II ions (singly ionised Al) only and the exposure time was 3 ns.

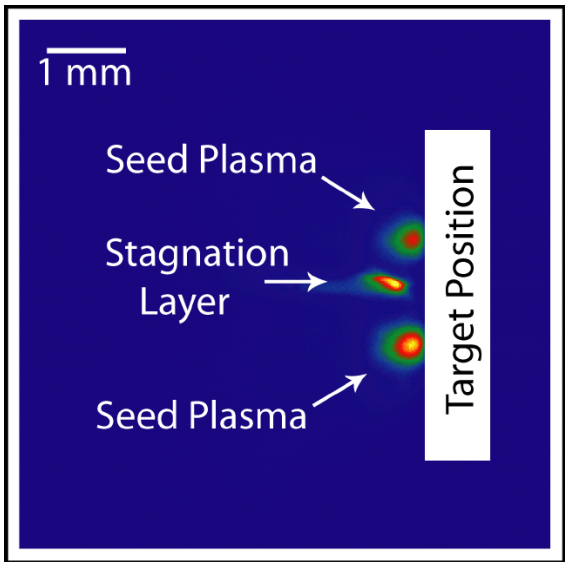

Figure 1.11: Sample image of two seed plasmas and stagnation layer taken 40 ns after the creation of the seed plasmas.

Briefly, several configurations for generating colliding plasmas have been investigated by different groups internationally, including a split laser beam focused onto two orthogonal targets [17], a single beam impinging onto a hemispherical target [44] and a single beam focused to create annular plasmas [45]. Diagnostics used to probe colliding laser produced plasmas in the past mainly include visible and X-ray emission imaging and spectroscopy (e.g. Harilal *et al.* [46], Leboucher-Dalimier *et al.* [47], Eagleton *et al.* [48] and Luna *et al.* [17]).

In this work a new experimental laboratory facility was constructed to investigate the properties and potential applications of colliding laser produced

plasmas. A flat target configuration was used for all colliding plasma experiments performed during this work. The first reason for choosing the flat target arrangement is due to the simplicity of the experimental system which avoids the alignment challenges that can arise when utilising, for example, angled targets. Secondly, to avoid laser drilling, the target system needs to be moved, after the laser impinges on the target surface, to reveal a fresh surface. By employing a flat target, it is possible to move the target in 2-dimensions significantly increasing the life of a target compared to an angled target which can only be moved in 1 direction.

Finally, a variety of plasma diagnostic techniques were employed to investigate the properties of colliding plasmas, including Nomarski laser interferometry, fast imaging and optical emission spectroscopy which revealed detailed information on the spatial and temporal dynamics of electrons, neutral atoms and ions in the colliding plasmas with high resolution. A Faraday cup was utilised to reveal the distribution of the kinetic energies of the ions emitted from the colliding plasmas.

References

[1] P. K. Carroll, and E. T. Kennedy, Laser-Produced Plasmas, *Contemporary Physics*, **22,** 1, 61 – 96 (1981).

[2] R. J. Goldston and P. H. Rutherford, Introduction to Plasma Physics, Institute of Physics Publishing, (1995).

[3] S. Eliezer, The interaction of High-Power Lasers with Plasmas, Institute of Physics Publishing, (2002).

[4] D. R. Corson and P. Lorrain, Electromagnetic Fields and Waves, Freeman, New York, (1988).

[5] S. Hafeez, N. M. Shaikh and M. A. Baig, Spectroscopic Studies of Ca Plasma Generated by the Fundamental, Second, and Third Harmonics of a Nd:YAG Laser, *Laser and Particle Beams*, **26**, 1, 41-50 (2008).

[6] H. R. Griem, Plasma Spectroscopy, McGraw-Hill, (1964).

[7] I. H. Hutchinson, Principles of Plasma Diagnostics, New York, Cambridge University Press, (1987).

[8] H. Luna, J. Dardis, D. Doria, and J. T. Costello, Analysis of Time-Resolved Laser Plasma Ablation using an Imaging Spectra Technique, *Brazilian Journal of Physics*, **37**, 1301 (2007).

[9] R. K. Singh, and J. Narayan, Pulsed Laser Evaporation Technique for Deposition of Thin Films: Physics and Theoretical Model. *Physical Review B*, **41,** (13), 8843-8859 (1990).

[10] Y. Okano, Y. Hironaka, K. G. Nakamura, and K. Kondo, Time-resolved Electron Shadowgraphy for 300 ps Laser Ablation of a Copper Film, *Applied Physics Letters*, **83**, 8 (2003).

[11] C. Ursu, S. Gurlui, C. Focsa, G. Popa, Space- and Time-Tesolved Optical Diagnosis for the Study of Laser Ablation Plasma Dynamics, *Nuclear Instruments and Methods in Physics Research Section B: Beam Interactions with Materials and Atoms*, **267**, 446–450 (2009).

[12] P. Hough, C. McLoughlin, T. J. Kelly, P. Hayden, S. S. Harilal, J. P. Mosnier, J. T. Costello, Electron and ion stagnation at the collision front between two laser produced plasmas, *Journal of Physics D: Applied Physics*, **42**, 055211 (2009).

[13] D. Salzmann. Atomic Physics in Hot Plasmas, Oxford University Press, New York, (1998).

[14] D. Colombant and G. F. Tonon, X-Ray-Emission in Laser-Produced Plasmas. *Journal of Applied Physics*, **44**, (8), 3524-3537 (1973).

[15] T. P. Hughes, Plasmas and Laser Light, Hilger (1975).

[16] R. W. P. McWhirter, Plasma Diagnostic Techniques, Academic Press (1965).

[17] H. Luna, K. D. Kavangah, J. T. Costello, Study of Colliding Laser Produced Plasma by Analysis of Time- and Space-Resolved Imaging Spectra, *Journal of Applied Physics*, **101**, 033302 (2007).

[18] K. Kavanagh, Imaging and Spectroscopy of Laser-Produced Colliding Plasmas, Ph.D. Thesis, Dublin City University, (2006).

[19] J. Dardis, Interactions of Intense Optical and Extreme Ultraviolet Lasers with Atoms and Solids, Ph.D. Thesis, Dublin City University, (2009).

[20] S. S. Harilal, B. O'Shay, M. S. Tillack, C. V. Bindhu, and F. Najmabadi, Fast Photography of a Laser Generated Plasma Expanding Across a Transverse Magnetic Field, *IEEE Transactions on Plasma Science*, **33**, (2), (2005)

[21] J. Siegel, G. Epurescu and A. Perea, Temporally and Spectrally Resolved Imaging of Laser-Induced Plasmas. *Optics Letters*, **29,** (19), 2228-2230 (2004).

[22] W. Whitty, J. P. Mosnier, Diagnostic of an Expanding Laser-Produced Lithium Plasma using ICCD Frame Photography and Shadowgraphy, *Applied Surface Science*, **127**, 1035 – 1040, (1998).

[23] D. B. Geohegan, Fast Intensified-CCD Photography of $YBa_2Cu_3O_{7-x}$ Laser Ablation in Vacuum and Ambient Oxygen, *Applied Physics Letters*, **60**, 22, (1992).

[24] A. Cummings, G. O'Sullivan, P. Dunne. A Spatio-Temporal Study of Variable Composition Laser-Produced Sn Plasmas, *Journal of Physics D-Applied Physics*, **39,** (1), 73-93 (2006).

[25] P. W. Rambo and J. Denavit, Interpenetration and Ion Separation in Colliding Plasmas, *Physics of Plasmas*, **1**, (12), 4050-4060 (1994).

[26] M. E. Jones, D. Winske, S. R. Goldman, Modeling Ion Interpenetration, Stagnation, and Thermalization in Colliding Plasmas. *Physics of Plasmas*, **3**, (3), 1096 – 1108 (1996).

[27] N. M. Shaikh, S. Hafeez, B. Rashid and M. A. Baig, Spectroscopic Studies of Laser Induced Aluminium Plasma using Fundamental, Second and Third Harmonics of a Nd:YAG Laser, *The European Physical Journal D*, **44**, 371-379 (2007)

[28] H. R. Griem, Spectral Line Broadening by Plasmas, Academic Press, New York, (1974).

[29] D. Doria, K. D. Kavanagh, J. T. Costello, and H. Luna, Plasma Parametrization by Analysis of Time-Tesolved Laser Plasma Image Spectra, *Measurement Science and Technology*, **17**, 670, (2006).

[30] J. Ruiz-Camacho, F. N. Beg and P. Lee, Comparison of Sensitivities of Moire Deflectometry and Interferometry to Measure Electron Densities in z-pinch Plasmas, *Journal of Physics D-Applied Physics*, **40**, 7, 2026-2032 (2007).

[31] E. Hecht, Optics, Third Edition, Addison-Wesley, (1998).

[32] G. Pretzler, A New Method for Numerical Abel Inversion, *Zeitschrift Fur Natureforschung*, **46**, 7 (1991).

[33] http://optics.tugraz.at/idea/idea.html

[34] M. Hipp, J. Woisetschläger, P. Reiterer and T. Neger, *Measurement*, **36**, 53-66, (2004).

[35] W. O. Siewa, T. Y. Tou, K. H. Wong, Shadowgraphy of Pulsed CO_2 Laser Ablation of Polymers, *Applied Surface Science*, **248,** 281–285, (2005).

[36] J.-F. Y. Gravel and D. Boudreau, Study by Focused Shadowgraphy of the Effect of Laser Irradiance on Laser-Induced Plasma Formation and Ablation Rate in Various Gases, *Spectrochimica Acta Part B*, **64**, 56–66, (2009).

[37] H. M. Mott-Smith and I. Langmuir, The Theory of Collectors in Gaseous Discharges, *Physical Review*, **28**, 727 - 763 (1926).

[38] D. W. Koopman, Langmuir Probe and Microwave Measurements of Properties of Streaming Plasmas Generated by Focused Laser Pulses, *Physics of Fluids*, **14**, 8, (1971).

[39] M. Faraday, Experimental Researches in Electricity, Vols. i. and ii, (1839, 1844).

[40] S. S. Harilal, B. O'Shay, Y. Z. Tao and M. S. Tillack, Ambient gas effects on the dynamics of laser-produced tin plume expansion, *Journal of Applied Physics*, **99**, 8, 083303, (2006).

[41] P. T. Rumsby, J. W. M. Paul, M. M. Masoud, Interactions Between two Colliding Laser Produced Plasmas, Plasma Physics, **16**, 969 – 975, (1974).

[42] C. Chenais-Popovics, P. Renaudin, O. Rancu, F. Gilleron, J.-C. Gauthier, O Larroche, O. Peyrusse, M. Dirksmöller, P. Sondhauss, T. Missalla, I. Uschmann, E. Förster, O. Renner and E. Krousk, Kinetic to Thermal Energy Transfer and Interpenetration in the Collision of Laser-Produced Plasmas, *Physics of Plasmas*, **4**, 190-208 (1997).

[43] J. D. Huba. Naval Reseach Laboratory: Plasma Formulary. http://www.ppd.nrl.navy.mil/nrlformulary/, Naval Research Laboratory, Washington, DC 20375, Revised Edition (2004).

[44] M. Purvis, J. Grava, J. Filevich, M. C. Marconi, J. Dunn, S. J. Moon, V. N. Shlyaptsev, E. Jankowska and J. J. Rocca, Dynamics of Converging Laser-Created Plasmas in Semicylindrical Cavities Studied using Soft X-ray Laser Interferometry, *Phyisical Review E*, **76**, 046402, (2007).

[45] F. Veloso, H. Chuaqui, R. Aliaga-Rossel, M. Favre, I. H. Mitchell, and E. Wyndham, Laser-produced Annular Plasmas, *Review of Scientific Instruments*, **77**, 063506, (2006).

[46] S. S. Harilal, C. V. Bindhu, and H.-J. Kunze, Time Evolution of Colliding Laser Produced Magnesium Plasmas Investigated using a Pinhole Camera, *Journal of Applied Physics*, **89**, 9, (2001).

[47] E. Leboucher-Dalimier, P. Angelo, P. Gauthier, X-Ray Spectroscopy and Imaging of Hot Dense Plasma Created by Colliding Foils. Simulation of Spectra.

Journal of Quantitative Spectroscopy and Radiative Transfer, **58**, 4-6, 721-735, (1997).

[48] R. T. Eagleton, J. M. Foster, P. A. Rosen, and P. Graham, One-Dimensional Time Resolved Soft X-Ray Imaging of Colliding Plasmas in a Laser Heated Cavity, *Review of Scientific Instruments*, **68**, 1, (1997).

Chapter 2:

Experimental Systems

In this chapter, details regarding the experimental apparatus used to perform all the measurements completed during the project is presented including, the design, assembly and operation of the entire laboratory facility along with the experimental arrangements and layouts for all of the plasma diagnostic techniques employed.

2.1: Design and Assembly of the Main Experimental Apparatus

The project began with the design and development of a new laboratory facility with the purpose of investigating the properties and identifying potential applications of colliding laser produced plasmas. The new laboratory facility was built as part of the Centre for Laser Plasma Research (CLPR) based in the School of Physical Sciences, Dublin City University (DCU) and the National Centre for Plasma Science and Technology (NCPST). Work began in October 2006 with an old laboratory space and the first stage included design and assembly of the entire experimental system along with all other lab infrastructure *e.g.* supporting tables.

The construction part of the project was broken down into 2 phases, the design phase and the assembly phase, each with their own projected timelines as follows:

2.1.1: The Design Phase (October 2006 – December 2006)

The initial design phase had a duration of 3 months with the objective of having all the necessary equipment for the project designed by the end of December 2006. The very first task at this time included clearing out the laboratory space entirely in preparation for assembly of the new experiment. A scaled cardboard model of the empty laboratory was created from which the size and orientation of the supporting tables that would be constructed to hold the experimental apparatus was determined. This established the layout of the apparatus for all future experiments. It was decided that the main supporting table for the target chamber and associated optical elements should be fabricated from extruded aluminium. The table to hold the Reflection Time of Flight Mass Spectrometer (RETOF – utilised by another PhD. student, Mr. Conor McLoughlin) was recycled from a steel table not in use at the time and specially adapted for our purposes. The final table to support the two lasers in the lab was made from a steel frame and adapted to hold an optical table to which the lasers were bolted to ensure maximum stability.

The main interaction chamber was the centrepiece of the experimental system and all other lab infrastructure was designed and constructed around it. In the design procedure a cylindrical chamber, 400 mm in diameter, was chosen with a wide range of access ports and windows ensuring maximum flexibility for incorporating the experimental layouts for the various planned plasma diagnostic experiments. To enable access to the whole chamber easily, it was decided that the main lid would be removable. The ISO configuration of the lid comprised a rubber o-ring which sat between the lid and the chamber and a set of four clamps which secured the lid to the chamber. Figure 2.1 shows a schematic of the design of the main interaction chamber along with main dimensions and the details of access ports.

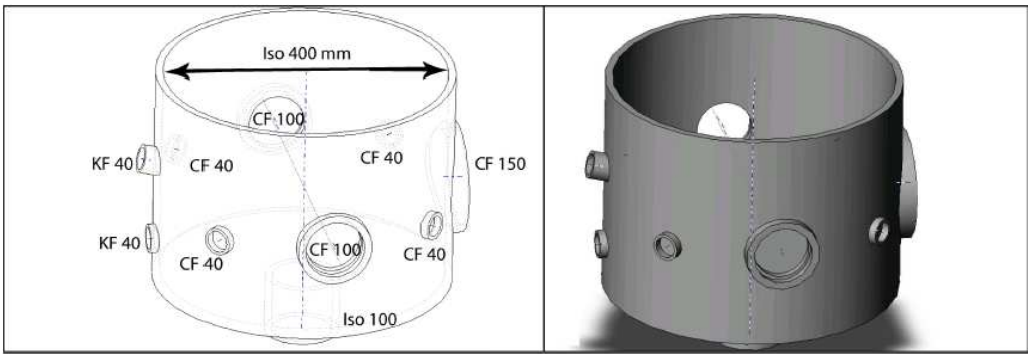

Figure 2.1: Schematic diagram of the main interaction chamber design along with main dimensions and access ports. Left: Wire blueprint. Right: 3D sketch.

This chamber was coupled to the Reflection Time of Flight Mass Spectrometer (RETOF) via a connecting straight tube and a T-piece. This is shown in figure 2.2 where the main interaction chamber along with the connecting straight, T-piece and RETOF is shown along with main dimensions. As the RETOF was operated by another Ph.D. student, its operating details and results are not included here although I was deeply involved in the integration design and commissioning of the device.

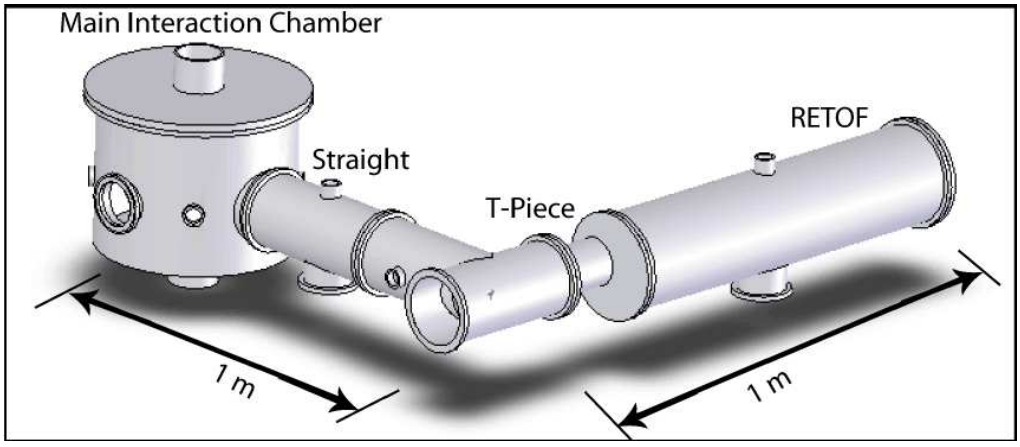

Figure 2.2: Schematic 3D drawing of the experimental system showing main interaction chamber, connecting straight, tee-piece and RETOF along with main dimensions.

A single stage differentially pumped vacuum system was designed. This system enabled the pressure in the main vacuum chamber to be varied whilst still maintaining high vacuum in the RETOF. This was necessary since it was essential to maintain the RETOF at high vacuum (better than 1×10^{-6} mbar) when in use as its Micro-Channel Plate (MCP) detector runs at high voltage (3 kV). Operating the MCP in low vacuum

could lead to electrical shorting across the detector which could cause irreversible damage. A vacuum gate valve was installed between the chamber and the RETOF so that it could be opened or closed to allow venting of the chamber whilst maintaining the RETOF under vacuum or vice versa. The differential pumping barrier was located between the RETOF and the T-piece where the only entrance to the RETOF was via a 0.5 mm hole in a conical skimmer. The RETOF was coupled to the side of the T-piece and could be accessed via a viewing port on the opposite side of the T-piece. Ions emitted from the laser produced plasma travel from the plasma chamber down along the straight and enter the RETOF. The technical drawings of the main components are given in the appendix A1. After the components were designed, the parts were ordered from various companies and construction of the experiment began.

2.1.2: The Assembly Phase (January 2007 – June 2007)

Once delivery of the components commenced, the assembly phase began. The first elements of the system to be assembled were the three supporting tables. One table needed to be refurbished and modified to support the RETOF. A new table constructed from extruded aluminium frame was assembled to hold the main interaction chamber and finally a steel frame also needed adapting and refurbishing and adapted to support the optical bench, optics and laser systems. Once assembly of the supporting tables was completed, the assembly of the RETOF began.

The main interaction chamber, straight and T-piece were ordered from ProVac Ltd., along with the various ports, flanges, vacuum electrical feed-throughs, copper gaskets *etc.* and so they were all delivered at the same time. Assembly of all these components took several weeks and once constructed vacuum testing began. A Leybold Turbovac TW250S (pumping speed of 250 l/s) turbo molecular pump was attached to the underside of the main interaction chamber via an ISO 100 flange. A

similar Leybold TW 250 l/s pump was used to pump the RETOF except that it was coupled to the RETOF via a CF100 flange. A smaller Leybold 50 l/s turbo molecular pump was used to evacuate the T-piece. Two oil sealed rotary pumps were used as backing pumps for the turbo pump mounted on the main interaction chamber and the T-piece. A third, oil free piston backing pump was used in conjunction with the turbo pump mounted on the RETOF in order to avoid any possible build up of oil on the MCP ion detector. The pressure in the main interaction chamber, T-piece and RETOF could be monitored separately using independent pressure gauges located at the different main sections. It was found that a base pressure of $\approx 5 \times 10^{-3}$ mbar was achieved throughout the whole vacuum system under backing pressure alone. With the turbo molecular pumps switched on, a base pressure of 3×10^{-7} mbar was achieved in the main interaction chamber and T-piece and 2×10^{-8} mbar in the RETOF. The turbo pump on the main interaction chamber also had variable speed capability and a gas purge to allow insertion of gas into the main interaction chamber for, firstly, studying the interaction of single and colliding plasmas in gaseous environments and, secondly, for materials growth using pulsed laser deposition in gases.

The in-vacuum, computer controlled, motorised target system was next to be assembled. It was decided to fit the target system with two axes of movement (vertical and lateral). Two vacuum translation stages were purchased (Thorlabs high precision motors, Model: T25X), both of which gave 25 mm of movement and adapted to give the vertical and lateral movement needed for experiments. A special flange with wire feed-throughs was also purchased so that the motors could be controlled under vacuum. The target system was then placed inside the chamber and positioned at its centre using alignment lasers. Figure 2.3 (left) shows a picture of the motorised target system and the base plate on which it rests. The assembled system was then located at the centre of the main interaction chamber. The white arrow defines the direction normal to the target (*i.e.* direction of plasma expansion), pointing towards the entrance of the RETOF (when in position in the experiment). The red arrows indicate

the 2 axes of movement of the motors. Figure 2.3 (right) shows the flange adapted to control the motors from outside the vacuum.

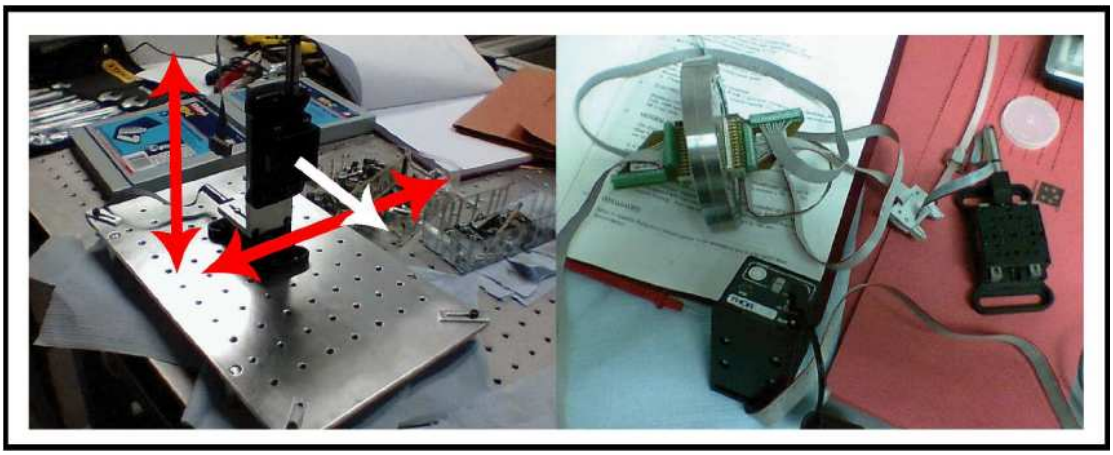

Figure 2.3: Left: Picture of in-vacuum, computer controlled motorised target system. The white arrow defines the direction normal to the target and the red arrows outline the axis of movement for the target. Right: Picture of the vacuum feed-through enabling computer control of the motor whilst maintaining vacuum.

The next task centred on locating and integrating the two laser systems (Continuum Surelite III & I) in the lab along with the associated beam guiding and focussing optics. One laser (Surelite III) was used to create the laser produced plasmas and the other (Surelite I) was employed as the source of laser light for Nomarski interferometry and shadowgraphy. Both lasers were bolted to the table with the optical bench to provide maximum stability. Three Stanford DG535 delay generators and two PCs were setup in the lab to control the entire experiment electronically. The maximum temporal jitter between the two lasers was 1 ns. This concluded the design and assembly of all the major components of the experiment. In figure 2.4 a comparison is made between the laboratory just at the start of construction (January 2007) and the laboratory in full operation (January 2009).

Figure 2.4: Comparison of the laboratory just at the start of construction (January 2007) and the laboratory in full operation (January 2009).

Once the main experimental components were assembled and installed, work began on setting up the various plasma diagnostics for experiments.

2.2: The Surelite Laser Systems

Figure 2.5 shows a schematic diagram of a Surelite laser system.

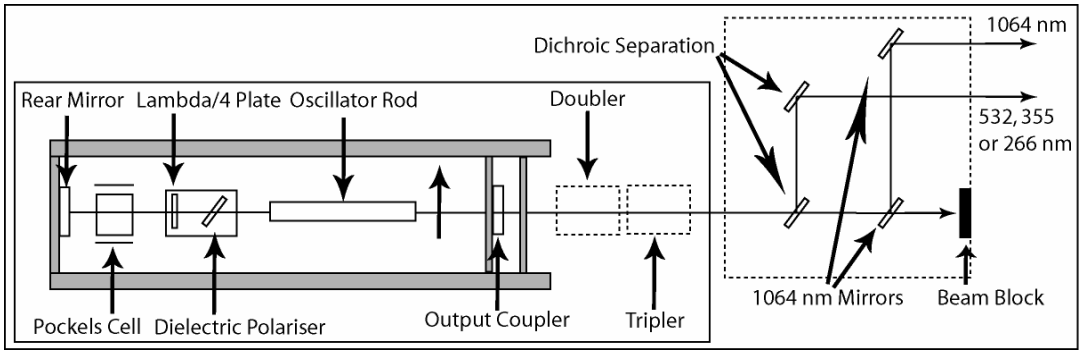

Figure 2.5: Schematic diagram of a Surelite laser system. The harmonic generating optics are shown as dashed lines as they are absent in the Surelite III but present in the Surelite I.

For general purpose use, all aspects of the Surelite lasers operated using internal electronics – i.e. the Pockels cell triggered at an optimal delay time of 180 μs after the flashlamps trigger (*cf.* figure 2.11 below). Both lasers operated at a repetition rate of 10 Hz (the optimal repetition rate). For the experimental studies presented

here, the operation of both Surelites (flashlamps and pockels cell) were controlled using Stanford DG535 delay generators in single shot mode allowing the outputs from both lasers to be synchronised with a maximum temporal jitter of 1 ns.

The Surelite I-10 laser could be operated at 1064 nm, 532 nm, 355 nm, and 266 nm producing maximum energies of 450 mJ, 230 mJ, 130 mJ and 60 mJ respectively and these energies were achieved during testing. The Full Width at Half Maximum (FWHM) of the pulse obtained from the Surelite I, operating at its fundamental frequency, was measured to be 6 ns and was *ca.* 2 ns shorter when operating the second harmonic (532 nm).

The Surelite III-10 laser only operated at its fundamental wavelength of 1064 nm and produced a pulse carrying an energy of 800 mJ with a FWHM of 6 ns. The output from each laser was linearly polarised with a Gaussian beam profile and a divergence of 0.6 mrad. The salient characteristics of both the laser systems are summarised in Table 2.1.

Table 2.1: Characteristics of the Surelite laser systems used

	Surelite I-10	Surelite III-10
Wavelength	1064, 532, 355 & 266 nm.	1064 nm
Energy	450, 230, 130 & 60 mJ	800 mJ
Pulse width (FWHM)	6 ns (4 ns for Harmonics)	6 ns.
Repetition Rate	10 Hz or Single Shot	10 Hz or Single Shot
External Trigger Jitter	1 ns	1 ns

The output pulses from both lasers were measured using a fast photodiode (1 ns risetime). These oscilloscope traces are shown below in figure 2.6 for a) the Surelite III-10 pump laser and b) the Surelite I-10 probe laser with Gaussian profiles fitted to the oscilloscope traces.

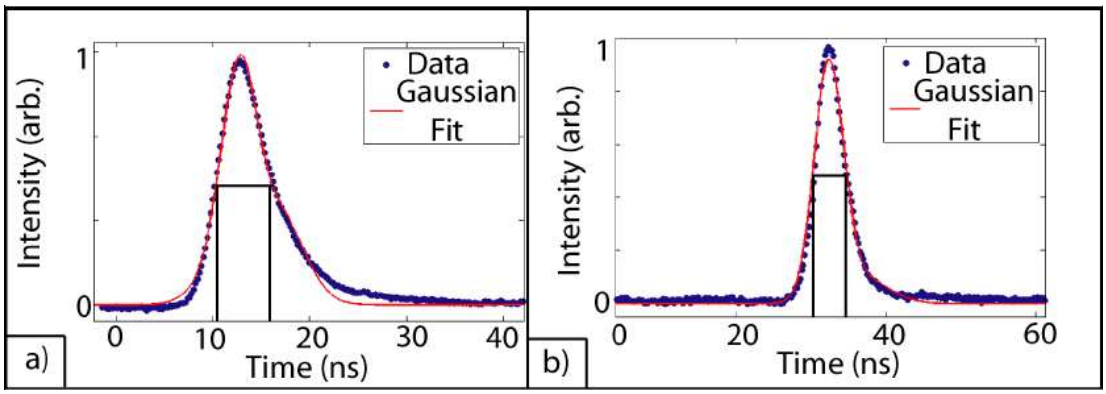

Figure 2.6: a) Fast diode trace of the output from the Surelite III-10 laser (1064 nm output). Second order Gaussian fit is shown in red. The full width at half maximum for this trace is 6 ns. b) Fast diode trace of the output from the Surelite I-10 laser. First order Gaussian fit is shown in red. The trace has a full width at half maximum of 4 ns (532 nm output).

2.3: Laser Plasma Generation

2.3.1: Single Laser Plasma Generation

To create a single laser generated plasma, a plano-convex lens with a focal length of 300 mm and a diameter of 25.4 mm with, anti-reflection coating for the 1000 nm – 1200 nm wavelength range, was used to focus the laser beam to a spot on the solid target as illustrated in figure 2.7.

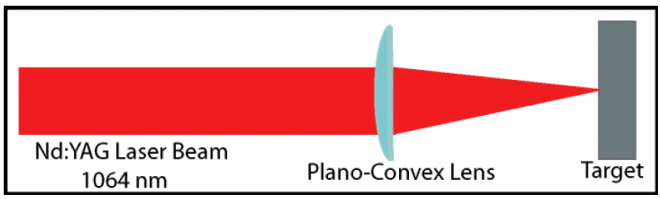

Figure 2.7: Schematic of the optical setup for creation of a single laser produced plasma.

The spot size achieved with this optical arrangement was ≈ 100 µm and using the 800 mJ output from the Surelite III laser a peak irradiance of ≈ 4×10^{11} W cm^{-2} was

achieved at the focal point. Using the simple collisional-radiative model of Colombant and Tonon [1], an initial temperature of ≈ 100 eV is obtained for such a single laser produced plasma using an aluminium target.

2.3.2: Colliding Laser Plasma Generation

The optical system used to split the colliding laser produced plasmas was similar to that used by Harilal *et al.* [2] and is depicted in figure 2.10. A 0.5° wedge prism split the laser beam into two separate beams which were subsequently focused onto the surface of an aluminium slab target by means of a 300 mm focal length plano-convex lens. The experimental setup was optimised to probe the evolution of the atom, ion and electron densities of this stagnation layer in space and time. The seed plasma plumes were created by splitting a 1064 nm wavelength, 600 mJ, 6 ns laser pulse into two parts and focusing them to two spots of diameter of 100 µm with a separation of 1.3 mm onto a flat slab of 99.99% pure aluminium. The peak irradiance at each spot was ≈ 1.6×10^{11} W cm^{-2}. A schematic drawing of the optical system used to create the colliding plasmas is shown in figure 2.8.

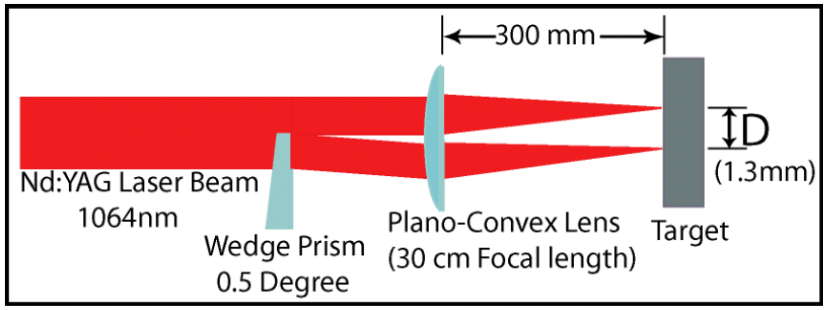

Figure 2.8: Setup used to create the colliding laser produced plasmas. The incoming laser beam from a Surelite III Nd-YAG laser is split into two beams by a 0.5° Wedge Prism and focused to two points using a plano-convex lens with a diameter of 25.4 mm and a focal length of 300 mm. The lens is placed 300 mm away from the flat aluminium target and the two laser beams are focused to points each with a spot size of ≈100µm. The separation, D, between the two spots is 1.3 mm.

2.4: Laser Based Plasma Probes

2.4.1: The Nomarski Laser Interferometer

As stated in the introduction Nomarski laser interferometry was one of the main plasma diagnostic tools employed in the new experimental laboratory. The main benefit of interferometry as a diagnostic tool is that it can diagnose the plasma accurately (specifically electron densities) in the nascent phase, *i.e.*, at very early times after plasma ignition (typically in the range of 0 – 100 ns). These early times are the most important when investigating colliding laser induced plasmas as critical plasma – plasma collisions, which can have a strong bearing on the final outcomes at the collision front or plane, occur on this time scale and so these early times are the most interesting when studying colliding plasmas.

It was decided that a Nomarski type polarisation interferometer [3] was the best choice for this application. The main advantages of the Nomarski interferometer is the simplicity of its design and the absence of stability and alignment problems associated with the other type of beam-splitting interferometers e.g. Mach Zehnder [4] or Michelson [5].

The key to the enhanced stability offered by the Nomarski design is the fact that both interfering laser beams pass through the same optical components unlike other standard interferometers. Consequently, should an event that would cause a vibration in the experiment occur e.g. people walking, talking, opening doors, vibrations from pumps *etc.*, that vibration will affect both the laser beams equally as they pass through the same optical components, thus cancelling out vibration effects in the interferograms. In effect it has common mode vibration rejection inherent in the design.

The first stage of building the interferometer was designing it. After studying similar experiments reported in the literature (e.g. those of Benattar *et al.* [3] and Beg *et al.* [6]) an initial design of the interferometer for use in this particular experiment was created. This design is shown schematically in figure 2.9.

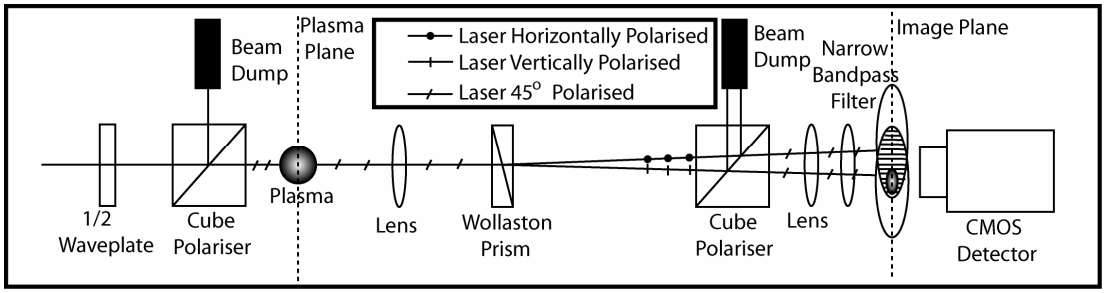

Figure 2.9: Schematic drawing of the design of the Nomarski Interferometer showing the main components (after Benattar [3]).

The principle of operation of the interferometer is as follows. The first beam-splitting cube polariser is used to set the polarisation direction of the probe laser beam to 45° and so the beam contains equal amounts of horizontally and vertically polarised components. A $\lambda/2$ waveplate is used in conjunction with the first cube polariser to divert the majority of the energy of the laser beam into the beam dump. Only a small percentage (≈ 4%) of the probe laser beam energy passes through the interferometer. This is due to the fact that the CMOS imaging chip detects the laser light directly and so if the energy of the beam were too high, irreparable damage would be caused to the imaging chip. Also, all optics positioned after the first cube polariser were designed for low power laser beams and so this is also another reason for dumping the majority of energy in the laser beam.

After passing through the plasma, the laser beam hits the Wollaston Prism. Here it is split into two laser beams (the vertically polarised component and the horizontally polarised component) separated by an angular deviation of 0.6°. The fact that the beams are orthogonally polarised at this point means that they currently cannot interfere. To enable the two laser beams to interfere and make an interference

pattern, they pass through a second polariser, again orientated at 45° to the vertical thus projecting the two laser back onto the same plane of polarisation beams (in fact selecting aligned components of the light fields). The interference pattern is located at the overlap region of the two laser beams and is detected by the CMOS camera. Two lenses image the plasma plane onto the detector plane. Finally the narrow band-pass filter, which is centred at 532 nm, rejects light due to emission from the plasma itself ensuring only light from the probe laser beam is detected by the CMOS chip. After designing the interferometer the components were ordered with construction and testing starting upon delivery.

For Nomarski interferometry the two lasers and the CMOS camera were synchronised using two Stanford DG535 delay generators with a maximum temporal jitter of 1 ns. One of the delay generators constituted the master oscillator and generated a reference +5 V TTL pulse 10 μs wide with a repetition rate of 10 Hz which was used to trigger the flashlamps on the pump laser. The second output on the delay generator provided a second similar TTL pulse 180 μs after T_0 (the optimal time delay between the laser flashlamp and the Pockels cell trigger). This output was sent through an AND box and connected to the pump laser Q-switch. The other input into the AND box came from the output from the computer which generated a TTL signal once the F5 button was pressed on the computer. Only when both inputs into the AND box were positive, was a TTL signal was sent to the pump laser Q-switch and hence the laser fired a single laser shot. A copy of this TTL pulse provided the trigger for the camera to start the exposure, with the exposure time set to 1 ms during which time it captured the 4 ns duration interferogram. It was via this technique that the laser was operated in single shot mode whilst keeping the flashlamps triggered at 10 Hz which is important as it stabilised the temperature of the laser rods and hence the laser output.

A copy of the T_0 pulse from the master oscillator of the first delay generator was used as the external trigger for the second delay generator thereby synchronising

the two delay generators. The first output from the second delay generator (+5 V TTL, 10 µs wide, 10 Hz) was utilised to fire the flashlamps on the probe laser ensuring temperature stability of the laser rod. By adding a time delay between T_0 and this output, it was possible to vary the timing between the pump and probe lasers and in this way high temporal resolution was achieved. The final output from this generator was also set to fire 180 µs after the flashlamp trigger. This TTL pulse was input into a second AND box along with a copy of the output from the computer. Again, only when both inputs into the AND box were positive, a TTL signal was sent to the probe laser Q-switch. This wiring diagram is show schematically below in figure 2.10.

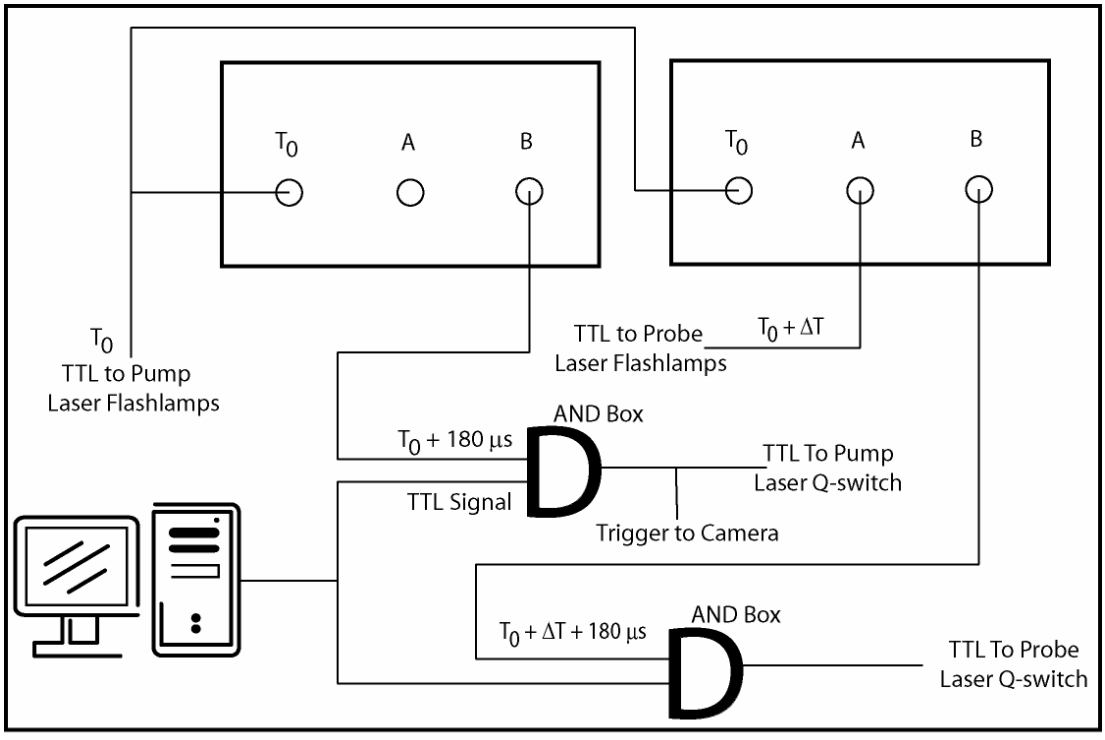

Figure 2.10: Electronic wiring diagram for synchronisation of the two Surelite laser systems and the camera.

Figure 2.11 below shows a schematic timing diagram (not to scale) of the various trigger pulses used to synchronise the laser systems and the camera.

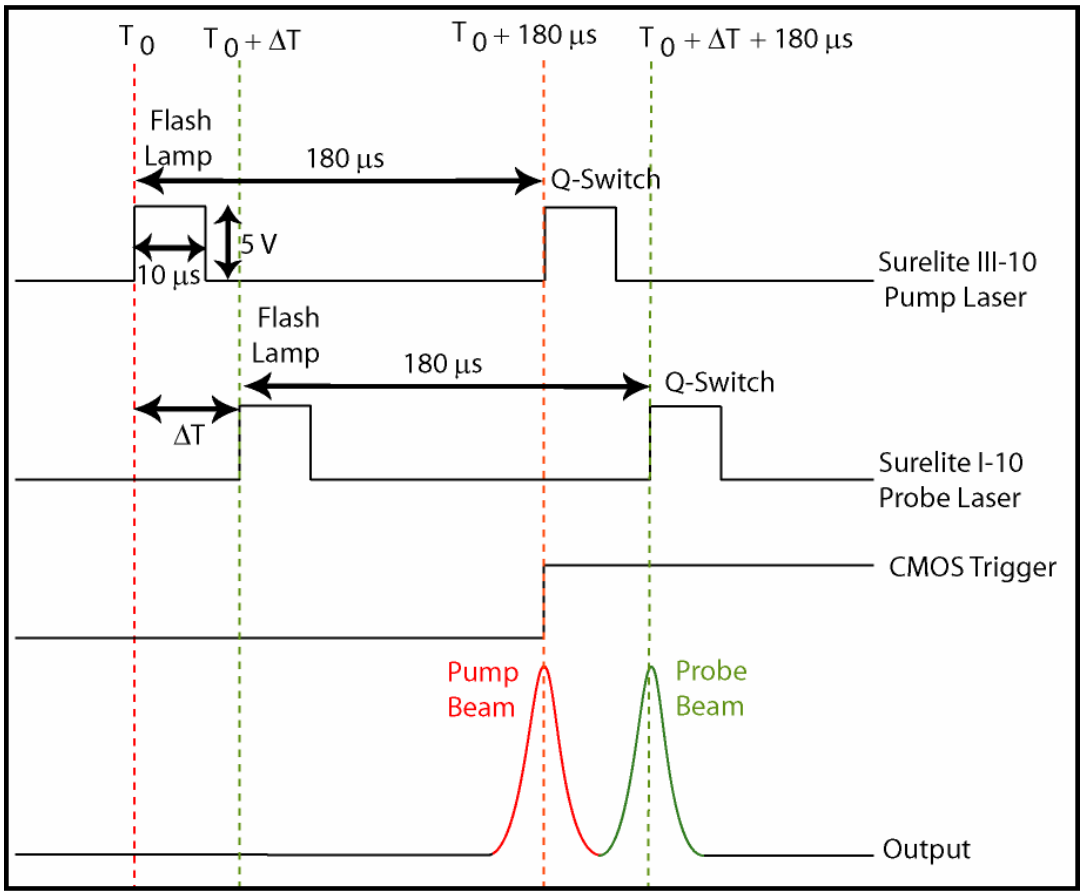

Figure 2.11: Timing diagram showing synchronisation of the lasers and the camera for interferometry experiments.

Finally, shown figure 2.12 is a schematic drawing of the entire experimental setup.

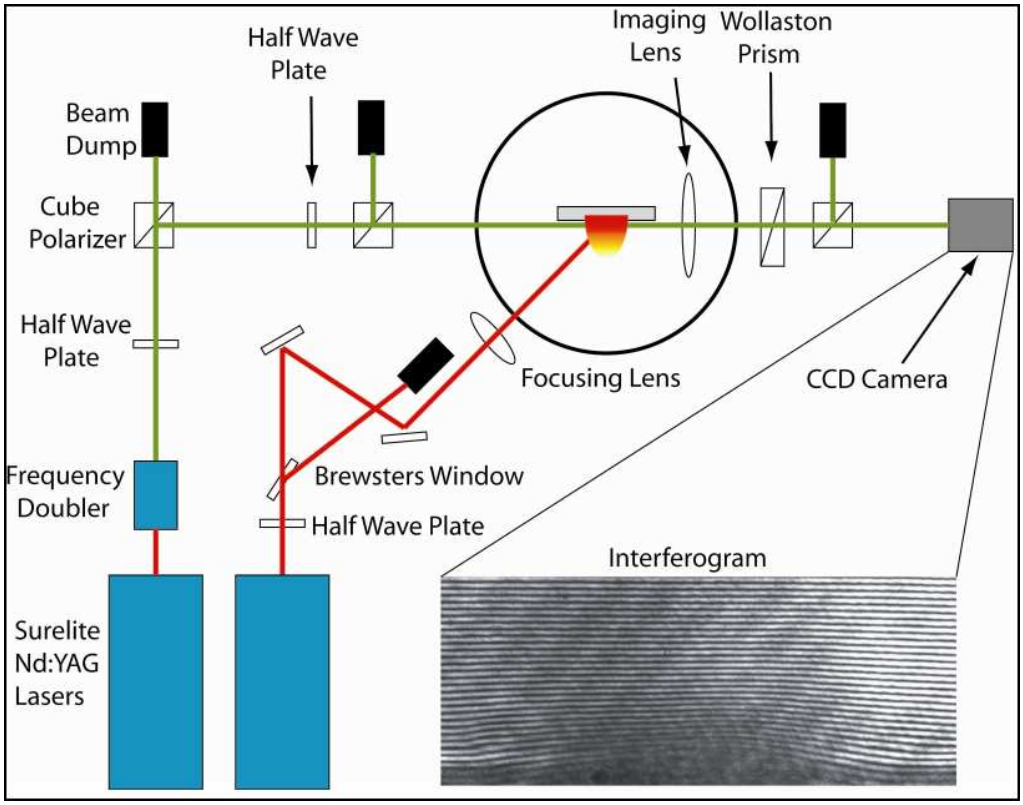

Figure 2.12: Schematic diagram showing the layout of the experimental system for performing Nomarski laser interferometry of laser produced plasmas.

The pump laser beam was incident at 45° to the target normal in order to allow expansion of the laser generated plasma into the RETOF which was orientated normal to the target. The combination of a Brewsters window and a half wave plate at the output of the pump laser beam enabled the energy of the laser beam reaching the target surface to be varied without affecting its pulsewidth.

During the testing stage, the interferometer was calibrated and tested on single laser plasma plumes, the results from which are presented in Chapter 3, Section 3.1. After the operation of the interferometer was well understood, experiments began on interferometery of laser plasmas produced in gaseous environments [7] and also experiments on colliding laser produced plasma plumes [8, 9], which were much more challenging experiments to perform.

2.4.2: Shadowgraphy

The setup for shadowgraphy experiments was the exact same as that for Nomarski interferometry except that all of the polarisation optics were removed when performing shadowgraphy. The resulting setup is referred to as a "focused shadowgraphy" system [10] where a relay lens system is used to image the shadowgram onto the CMOS imaging chip. This is shown schematically in figure 2.13.

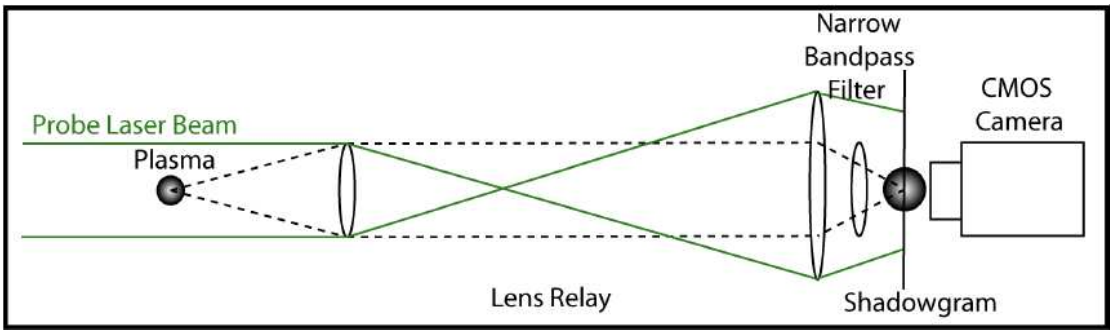

Figure 2.13: Schematic drawing of setup used for performing shadowgraphy of laser produced plasmas.

The exact same methods were used here for synchronising the laser systems and timing arrangements as were used for perform interferometry.

2.5: Optical Plasma Diagnostics

2.5.1: Spectrally Resolved Fast Imaging

Fast imaging refers to the visible imaging of the laser produced plasmas. The imaging system was spatially, spectrally and temporally resolved. Spatial resolution was obtained by using a zoom lens assembly to image the plasma onto a 2-dimensional ICCD camera.

Spectral resolution was achieved by introducing a narrow bandpass filter into the imaging system which isolated a particular transition or band of close lying transitions in a neutral atom or ion. Only radiation emitted from a particular neutral atom or ion with wavelengths within the bandwidth of the filter, reached the detector and so the spatial evolution of individual atoms or ions (in a particular state of excitation) could be tracked over time. For experiments presented in this thesis, two narrow bandpass filters were used to select isolated line emission from neutral aluminium atoms and singly charged aluminium ions.

The filter employed to select emission from neutral aluminium atoms was centred at 390 nm with a Full Width at Half Maximum (FWHM) of 10 nm. The detected line emission (which passed through the filter) has transitions at 394.4 nm ($3s^2 4s\ ^2S_{1/2} - 3s^2 3p\ ^2P_{1/2}$) and 396.15 nm ($3s^2 4s\ ^2S_{1/2} - 3s^2 3p\ ^2P_{3/2}$). The transmission curve for this filter is shown in figure 2.14 [11].

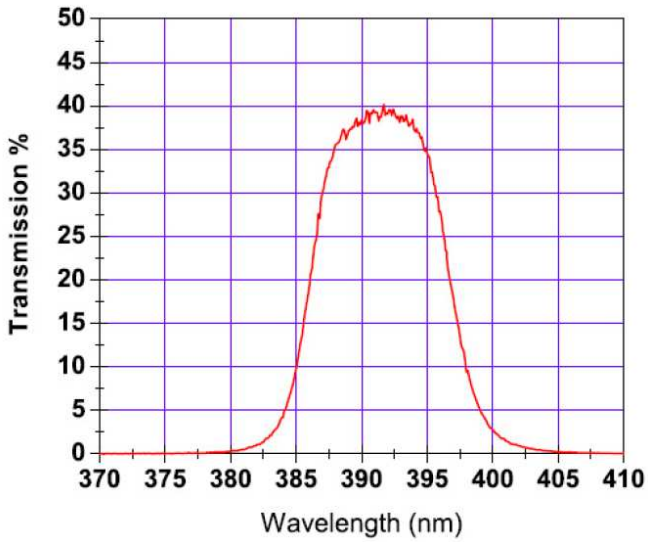

Figure 2.14: Transmission curve for the narrow bandpass filter centred at 390 nm used to isolate emission from neutral aluminium atoms [11].

For singly charged aluminium ions, the transition at 466.3 nm ($3s4p\ ^1P_0 - 3p^2\ ^1D$) was selected by employing a narrow band pass filter centred at 460 nm with a FWHM of 10 nm. The transmission curve for this filter is shown in figure 2.15 [11].

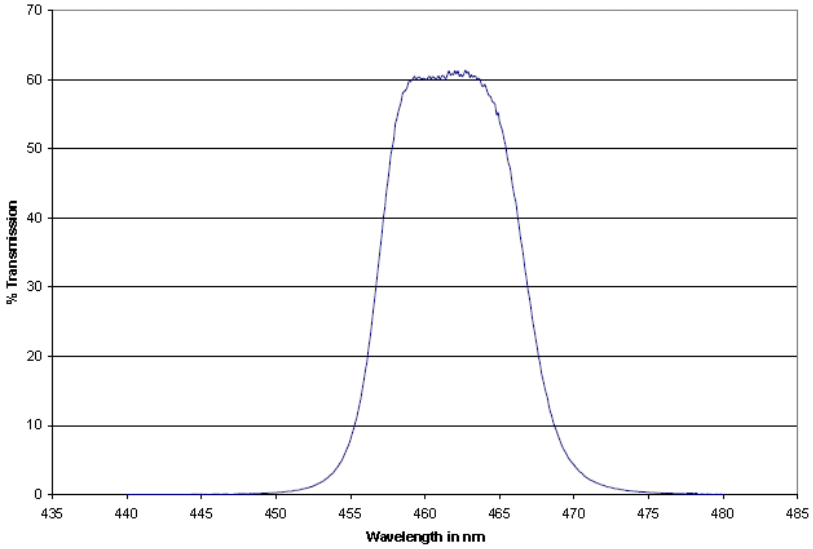

Figure 2.15: Transmission profile for narrow bandpass filter centred at 460 nm used to select emission from singly charged aluminium [11].

To observe bulk plasma emission a broadband short pass interference filter was employed which transmitted all radiation of wavelengths between 300 nm and 950 nm (so called “whitelight”). This served to block any scattered radiation from the Nd:YAG laser which had a wavelength of 1064 nm.

Time resolved imaging was achieved by employing an Intensified Charge Coupled Device (ICCD) as the framing camera. Two cameras were employed for fast imaging during the course of project. This was due to the sharing and allocation of equipment and resources in the CLPR because of high demand. Both of the cameras were supplied by Andor Technology. The first camera used was the DH5H7 model and comprised of 512 × 512 pixels with a pixel area of 24 µm × 24 µm yielding an active area of 12.3 × 12.3 mm^2. This CCD chip is coupled via a fibre optic coupler to a MCP which was gated to provide optical exposure times as low as 3 ns in duration thereby

providing very high temporal resolution. The second camera utilised was the DH534 model and comprised a CCD chip with 1024 × 1024 pixels of pixel area 13 µm × 13 µm yielding an active area of 12.3 × 12.3 mm^2. The CCD chip was lens coupled to the MCP in this camera and the minimum exposure time was also 3 ns.

A zoom lens assembly was coupled to the ICCD cameras to image the plasma onto the detector. Because the zoom lens could not be placed inside the vacuum chamber, the closest achievable distance from the zoom lens to the plasma (object distance) was ≈ 250 mm. This meant that in order to achieve high magnification (≈ 2 X) an extension tube (≈ 500 mm in length) was needed to increase the distance between the zoom lens and the camera. Without the zoom lens, the optical system would de-magnify the image of the plasma. A schematic diagram of the fast imaging setup is shown in figure 2.16 along with main dimensions.

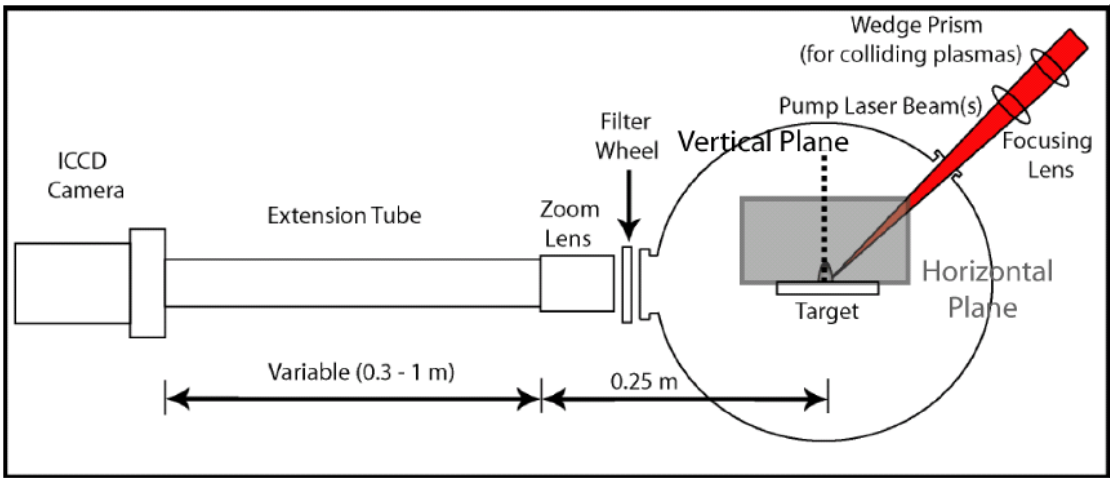

Figure 2.16: Schematic drawing of the experimental setup for fast imaging of laser produced plasmas. For better orientation, in this figure we are observing the vertical plane edge on and the horizontal plane face on.

The setup shown in figure 2.16 was employed extensively to perform fast imaging of colliding laser produced plasmas during the course of the studies reported here. The length of the extension tube could be varied between 0.3 and 1 m to adjust the magnification. A more detailed discussion of the creation of the colliding plasmas is

given in second 2.3 above. In this experimental setup the pump laser beam was split in the vertical plane and so both of the seed plasmas could be imaged using the experimental setup shown in figure 2.16.

A problem was encountered, however, when attempting to perform angle resolved fast imaging study of colliding plasmas (specifically angle resolved fast imaging of the stagnation layer), results from which are given in Section 4.5. The problem arises from the fact it was necessary that the camera, extension tube, and zoom lens remained stationary during the experiment to keep the imaging system stable and reproducible. Therefore, to perform angle resolved studies, it was necessary to rotate the colliding plasmas themselves. This was done by simply rotating the wedge prism about its centre as shown in figure 2.17 a) which results in a rotation of the deflected part of laser beam about the un-deflected portion of the pump laser beam. In doing so the plane of the colliding plasma system was changed from vertical to horizontal (see figure 2.16). As the pump laser beam was incident at 45° to the target normal, the deflected part of the pump laser beam was no longer tightly focused on the target surface resulting in 2 very different colliding plasmas. This problem is illustrated below in figure 2.17 b).

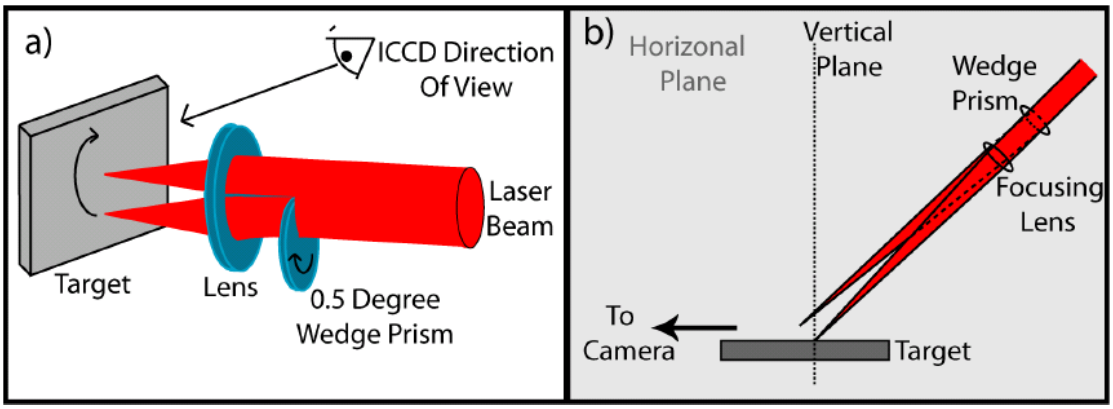

Figure 2.17: a) Illustration of the effect that rotating the wedge prism has on the deflected part of pump laser beam. b) Schematic diagram showing effect of having a 45° angle of incidence of the pump laser beam when attempting to perform angle resolved fast imaging. The vertical plane is viewed edge-on and the horizontal plane is viewed face-on in this drawing.

The only solution to this problem was to rearrange the experimental setup, specifically, the orientation of the target, so that the incident pump laser beam was always normal to the target ensuring that both laser beams were focused onto the surface of the target. Of course, in doing so, the target occludes the view of the camera. It was therefore necessary to rearrange the imaging system in order to view the colliding plasmas. Fortunately, there was a viewing port located at the required viewing angle but there was a space issue. As the RETOF location prevented a direct view of the interaction region, it was necessary to reflect the image of the plasmas with a broadband mirror to a direction away from the RETOF. A schematic drawing of the experimental setup designed to implement angle resolved imaging of colliding plasmas is shown in figure 2.18 a) along with a picture of the actual experimental setup figure 2.18 b).

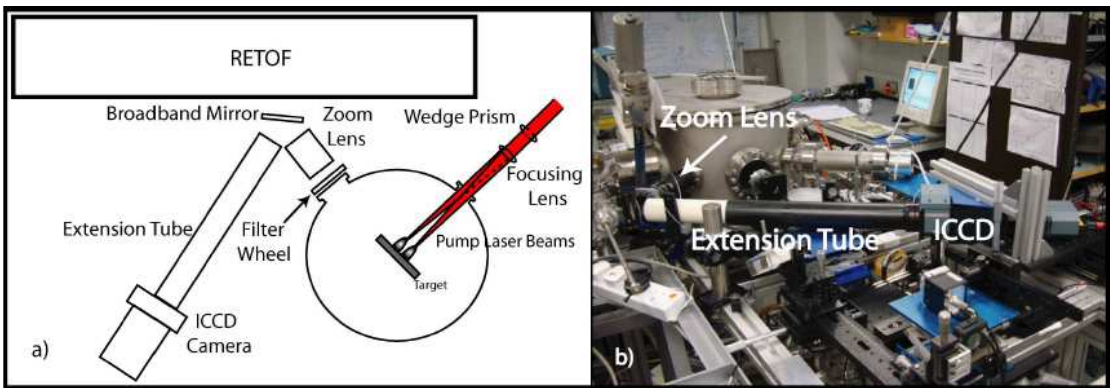

Figure 2.18 a): Schematic drawing of the optical imaging system designed to enable angle resolved fast imaging. b): Picture of actual experimental setup.

The angular resolution enabled fast imaging of the colliding plasmas with at two different viewing angles. These angles of views are defined as 0 degrees and 90 degrees as shown in figure 2.19. These studies were performed at delay times when the bulk of the visible emission originated from the stagnation layer, thus avoiding occlusion of the stagnation layer by the seed plasmas when observing along the 90 degree direction.

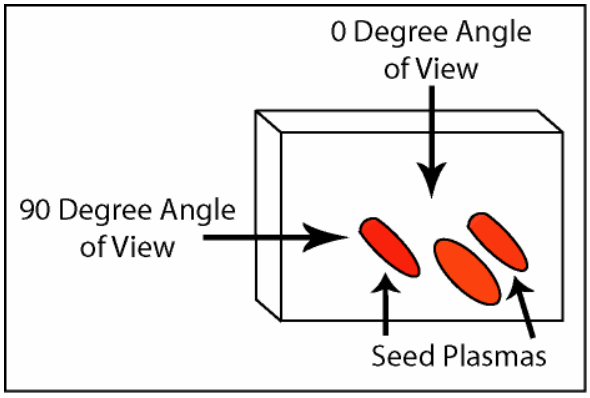

Figure 2.19: Definition of the two angles of view used for the angle resolved fast imaging of the stagnation layer.

To calibrate the magnification of the optical system it was necessary to insert an accurately graduated ruler in the plane normally occupied by the plasma. The zoom lens was then adjusted until the image of the ruler was focused onto the CCD chip and so could be clearly seen on the computer. Using an image of the ruler and knowing the physical size of each pixel it was possible to determine the magnification of the system. A calibration image for one of the experiments (imaging of colliding aluminium plasmas) is shown in figure 2.20 along with the intensity line out of the image and finally a calibration curve. The DH5H7 model camera was used for this experiment.

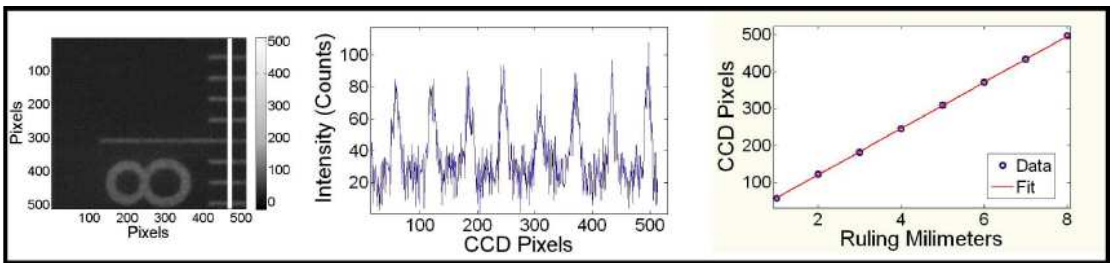

Figure 2.20: Left: Sample calibration image ruler for fast imaging experiment on colliding aluminium plasmas. The white line shows the position at which the lineout was taken. Centre: Plot of lineout intensity. Right: Calibration curve obtained from intensity lineout.

The magnification obtained with this setup was calculated to be *ca.* 1.5X although experiments presented here have been performed with magnifications as high as 3.2 X.

2.5.2: Optical Emission Spectroscopy

Spatially and temporally resolved Optical Emission Spectroscopy (OES) was performed on the stagnation layer created at the interface between the two colliding laser produced plasmas, the results from which provided the intensity distributions of the various species in the stagnation layer as described fully in Section 4.4.

The optical spectrometer consisted of a 0.5 m Chromex visible imaging spectrometer. The Andor Technology DH534 ICCD camera (1024 × 1024 pixels, lens coupled MCP) was mounted on the Chromex spectrometer. This allowed high resolution temporally resolved spectroscopy with a minimum intensifier gate width of 3 ns. The optical spectrometer was a Czerny-Turner mount with toroidal focusing mirrors which enabled aberration-corrected flat field imaging. It was operated with a 1200 line/mm diffraction grating with a blaze wavelength of 400 nm providing a resolution of 0.07 nm (FWHM) [12]. The instrument function of the spectrometer was determined using a method outlined by Kavanagh [13] using a narrow emission line (441 nm) from a cadmium lamp. Using a slit width of 60 μm, an instrument function of 0.16 nm was determined. This is the slit width that was used for all experiments presented in these studies. A schematic drawing of the experimental setup used for the optical emission spectroscopy studies is shown below in figure 2.21.

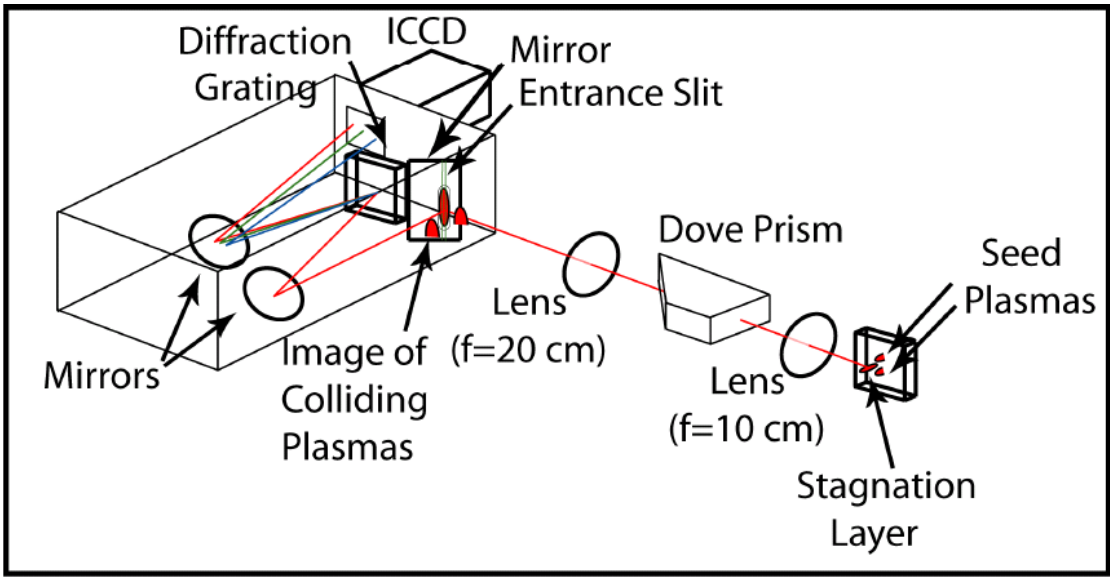

Figure 2.21: Schematic diagram showing the setup for the emission spectroscopy studies. The main components include the imaging system employed to create an image of the stagnation layer on the slit of the spectrometer. A schematic diagram of the Chromex 0.5 m spectrometer including the collimating and focusing mirrors and the diffraction grating and the ICCD camera is also given.

As can be seen in figure 2.21 a relay lens imaging system was employed to create an image of the colliding plasmas on the entrance slit of the spectrometer. The relay system comprised of a 10 cm focal length achromatic plano-convex lens located 10 cm away from the target and a 20 cm achromatic plano-convex lens positioned 20 cm away from the entrance slit of the spectrometer. The inclusion of a Dove prism served to rotate the image of the colliding plasmas so that the stagnation layer was aligned along the slit of the spectrometer. This offered spatial resolution along the stagnation layer away from the target. This is illustrated in figure 2.22 where the orientation with respect to the stagnation layer is shown.

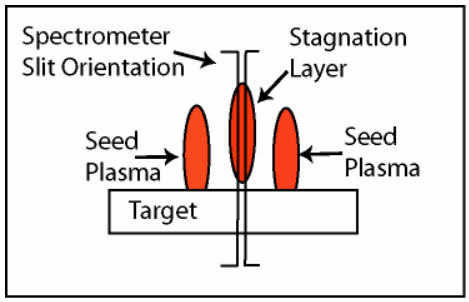

Figure 2.22: Orientation of the stagnation layer with respect to the slit of the spectrometer.

2.6: Faraday Cup Probe

As already outlined in chapter 1, a Faraday cup is a metal conductive cup capable of collecting charged particles [14]. The Faraday cup detector used during this work was completely surrounded by a grounded metal cage. This isolated the Faraday cup from electro-magnetic noise originating from the probe laser beam and the creation of the laser produced plasma. The entrance aperture was a 2 mm diameter hole and this hole was located 100 mm from the target surface. This resulted in a very low angular acceptance (≈ 1°) thus providing very high angular resolution when performing angle resolved ion emission experiments. A schematic drawing (not to scale) of the experimental setup is shown in figure 2.23.

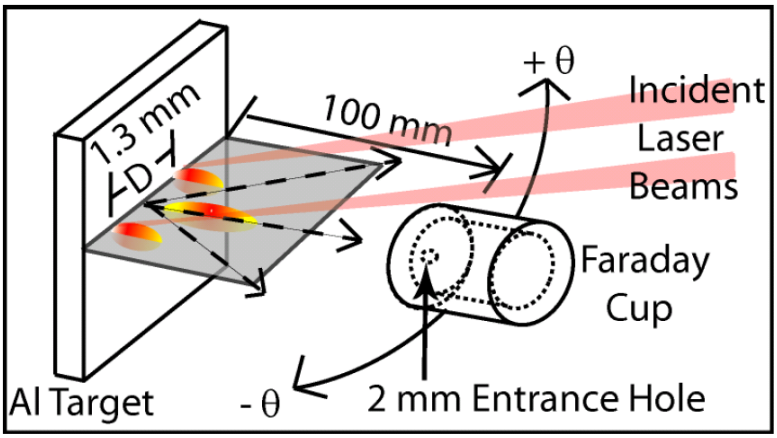

Figure 2.23: Schematic diagram of the experimental setup for Faraday cup measurements on colliding plasmas including main dimensions.

The optical system used to create the colliding plasmas is the same as that outlined in Section 2.3.2. When probing single plumes, one of the incident laser beams was blocked to compare to the probe signal from the colliding plumes. When performing angle resolved experiments, the Faraday cup was rotated about the centre of the colliding plasmas with an accuracy of ± 1°. All experiments were performed in vacuum at pressures of 1×10^{-5} mbar. The target was mounted on an in-vacuum high precision x-z motor and was moved to reveal a new surface after each laser pulse. A bias voltage

of -30 V was applied to the Faraday cup to attract ions from the laser produced plasma and + 30 V to attract electrons. The probe signals were collected across a 50 Ω resistor on a Textronix oscilloscope (Model: TDS3023, 300 MHz, 2.5 GS/s) in single shot mode triggered by a fast photodiode.

The bias circuit employed for the Faraday cup experiments presented in this thesis is shown schematically in figure 2.24.

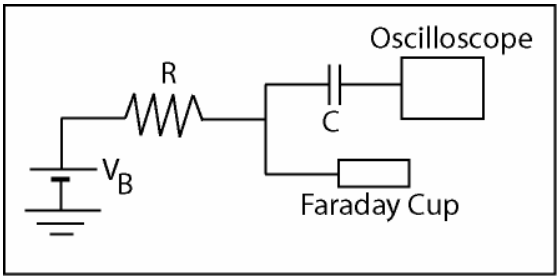

Figure 2.24: Bias circuit used with the Faraday cup.

As already outlined in section 1.6.5 the circuit allowed the transmission of the plasma signal collected by the Faraday cup but blocked the bias voltage used to collect the electrons or ions. The capacitor, C, had a capacitance of 1 μf and the resistor, R, had a resistance of 100 kΩ.

2.7: Summary

In this chapter details of the apparatus for performing experiments on single and colliding laser produced plasmas were presented. The design phase included designing all the vacuum systems, supporting tables, experimental layout, target systems and ordering the designed components from a variety of companies. The next phase comprised assembly of the entire experimental apparatus and testing e.g. vacuum testing. This phase also included location and integration of the main experimental systems such as laser systems, oscilloscopes, delay generators *etc.*

Once the main experimental apparatus was assembled work focused on designing and constructing the plasma diagnostics techniques, including fast imaging, optical emission spectroscopy, Nomarski interferometery, shadowgraphy and a Faraday cup electrical probe. The chapter included a description of the experimental apparatus for the various plasmas diagnostic techniques. The experimental setup for creation of the colliding plasmas was also presented.

References

[1] D. Colombant and G. F. Tonon, X-Ray-Emission in Laser-Produced Plasmas. *Journal of Applied Physics*, **44**, (8), 3524-3537 (1973).

[2] S. S. Harilal, C. V. Bindhu, and H.-J. Kunze, Time Evolution of Colliding Laser Produced Magnesium Plasmas Investigated using a Pinhole Camera, *Journal of Applied Physics*, **89**, 9, (2001).

[3] R. Benattar, C. Popovics and R. Sigel, Polarized-Light Interferometer for Laser Fusion Studies. *Review of Scientific Instruments*, **50**, 12, 1583-1585, (1979).

[4] M. F. Ye, and D. Y. Jiang, Multiframing Mach-Zehnder Interferometer for Spatiotemporal Electron Density Measurement in a Field-reversed Configuration Plasma, *Review of Scientific Instruments*, **70**, 1, 691-693, (1999).

[5] N. H. Cheung, L. C. Ng, and S. C. Chen, A Moving-Mirror Michelson Interferometer for Probing Transient Plasma Plumes, *Review of Scientific Instruments*, **64**, 1, 49-51, (1993).

[6] J. Ruiz-Camacho, F. N. Beg and P. Lee, Comparison of Sensitivities of Moire Deflectometry and Interferometry to Measure Electron Densities in z-pinch Plasmas, *Journal of Physics D-Applied Physics*, **40**, 7, 2026-2032 (2007).

[7] P. Hough, C. McLoughlin, T. J. Kelly, S. S. Harilal, J. P. Mosnier, J. T. Costello, Time resolved Nomarski interferometry of laser produced plasma plumes, *Applied Surface Science*, **255**, 10, 5167-5171 (2009).

[8] P. Hough, C. McLoughlin, T. J. Kelly, P. Hayden, S. S. Harilal, J. P. Mosnier, J. T. Costello, Electron and ion stagnation at the collision front between two laser produced plasmas, *Journal of Physics D: Applied Physics*, **42**, 055211 (2009).

[9] P. Hough, C. McLoughlin, S. S. Harilal, J. P. Mosnier, J. T. Costello, Emission Characteristics and Dynamics of the Stagnation Layer in Colliding Laser Produced Plasmas, Accepted, Journal of Applied Physics, December 2009.

[10] G. S. Settles, Schlieren and Shadowgraph Techniques : Visualizing Phenomena in Transparent Media, Springer, Berlin, 2001.

[11] Thorlabs Ltd. (http://www.Thorlabs.com)

[12] H. Luna, K. D. Kavangah, J. T. Costello, Study of Colliding Laser Produced Plasma by Analysis of Time- and Space-Resolved Imaging Spectra, *Journal of Applied Physics*, **101**, 033302 (2007).

[13] K. Kavanagh. Imaging and Spectroscopy of Laser-Produced Colliding Plasmas. Ph.D. Thesis, Dublin City University, (2006).

[14] S. S. Harilal, B. O'Shay, Y. Z. Tao and M. S. Tillack, Ambient gas effects on the dynamics of laser-produced tin plume expansion, *Journal of Applied Physics*, **99**, 8, 083303, (2006).

Chapter 3:

Laser and Optical Diagnostics of Single Laser Produced Plasmas

In this section the results from the experiments, on single laser produced plasmas, performed using the new laboratory facility are presented. The very first experiments were focussed on laser interferometry of single laser produced plasmas in vacuum environments and aimed to test the operation of the new laboratory (i.e. vacuum systems, laser systems, synchronisation techniques *etc.*). In addition, similar experiments had already been reported in the literature, which therefore provided a means to benchmark the results from the Nomarski laser interferometer.

Once the first experiments were completed with results analysed and benchmarked, the operation of the new laboratory was well understood and work progressed to performing more challenging experiments, such as analysis of single laser produced plasmas in gaseous atmospheres using interferometry. The results from these experiments are presented later in this chapter. These experiments are currently of particular interest to the PLD scientific community (who deposit and grow materials using laser ablation, mostly in background gases). For this reason, an elemental target and background gas, of significant topical interest to this community, were chosen for this work, namely, zinc and oxygen.

The final results presented in this chapter concern laser interferometry as a diagnostic technique for analysing the so called “shock-fronts” or, more specifically, the compressive layers of gas that are created and expand rapidly outwards after a laser produced plasma is created in a background gaseous atmosphere. Currently, shadowgraphy is the main diagnostic tool for analysing such compressive layers and the final results presented in this chapter compare and contrast both techniques.

3.1: Nomarski Laser Interferometry

3.1.1: Vacuum Environment

As stated in Chapter 2 (*cf.* Section 2.2), following construction of the laboratory the first stages involved extensive testing and calibration of the laser interferometer to ensure it was operating as expected. The easiest way to do this was to first use the laser interferometer to make measurements on individual laser generated plasma plumes in a vacuum environment. Interferometery of single laser generated plasma plumes in vacuum has already been well investigated and consequently, there is a lot of published literature readily available for comparison. The experimental details for interferometery of single laser generated plasma plumes are also described in Chapter 2 (*cf.* Section 2.3.2).

Densities in the range 10^{18} – 10^{20} cm^{-3} in the regions close (< 1 mm) to the target normal were expected from the literature, [1-4]. This provided a good comparison for our calibration purposes. Figure 3.1 shows the results from one such calibration experiment. The plasma plumes were generated by focusing the output of a Nd:YAG Surelite III working at its fundamental wavelength of 1.064 μm with an energy of 700 mJ onto a solid 99.99% pure Zn solid target using a 30 cm plano-convex lens.

The spot size had a diameter of 100 μm and the pulse width of the laser pulse was 6 ns. The background pressure in the chamber was 1 X 10^{-4} mbar. The error associated with the electron density was determined by finding the minimum detectable fringe shift and extracting its corresponding electron density. A value of ± 0.22 × 10^{19} cm^{-3} has been obtained for the minimum detectable fringe shift.

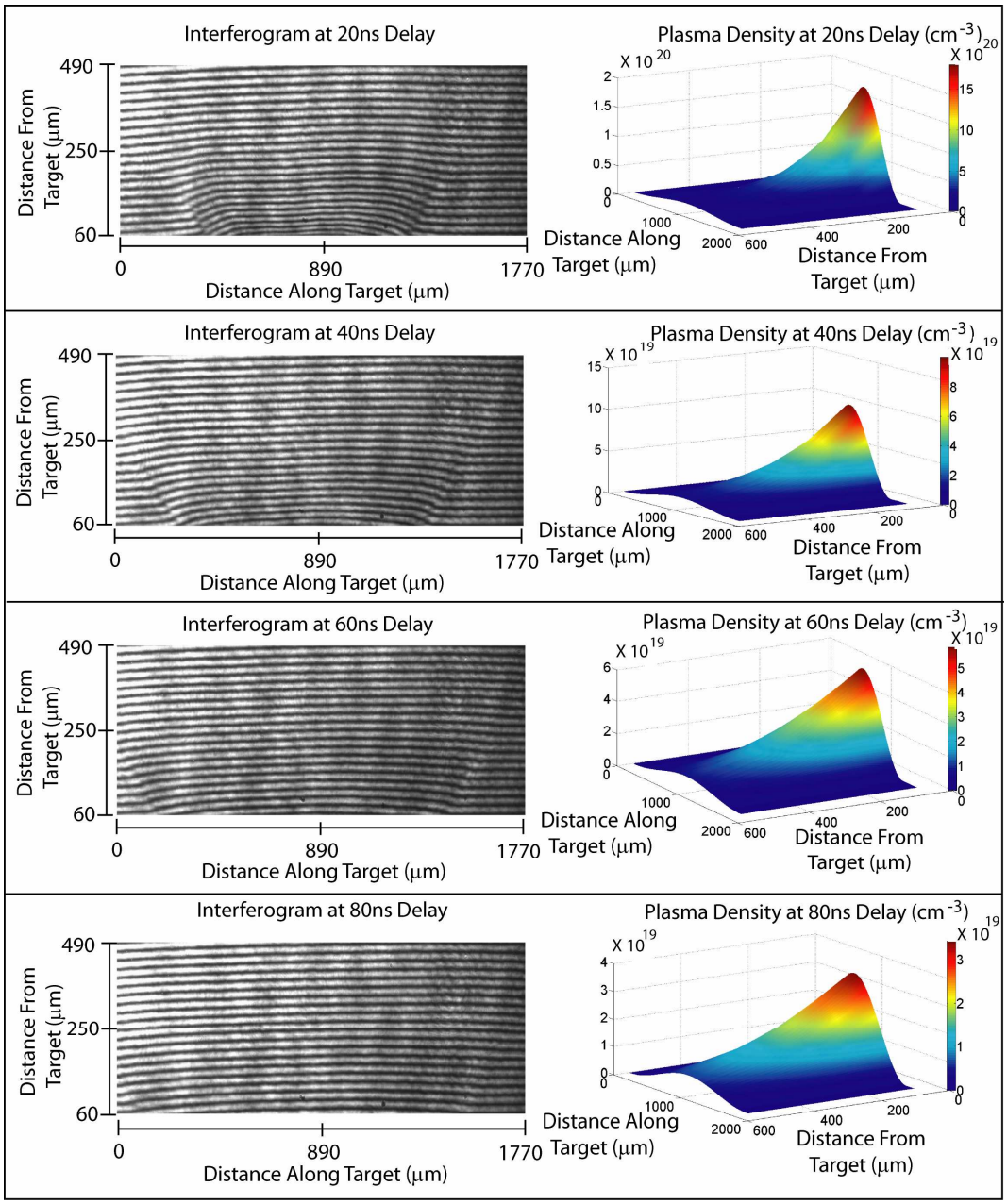

Figure 3.1: Comparison of the electron density profile of a single Zn plasma plume at delay times of 20, 40, 60 and 80 ns after the peak of the pump laser beam.

The results from the Nomarski interferometer compare very well with previous published work [1 - 4] and allowed for much deeper understanding of the operation and limitations of the interferometer and the analysis of the interferograms. The testing provided a good starting point to attempt more complex and difficult experiments – *e.g.* interferometery of plasmas in gaseous environments and colliding laser generated plasmas.

However, before attempting such experiments, the interferometer was utilised to perform more detailed experiments on single laser produced plasmas in a vacuum environment. First of all, an investigation was conducted to analyse the spatial and temporal behaviour of the electron density profile of laser produced aluminium whilst varying the energy of the incident plasma producing laser beam. The energy of the pump beam was varied several times between 130 mJ and 800mJ. The one dimensional (1D) spatial behaviour of the electron density, normal to the target was extracted from the interferograms at a delay time of 10 ns after the peak of the pump laser pulse for the various laser energies studied. The results of this analysis are shown below in figure 3.2.

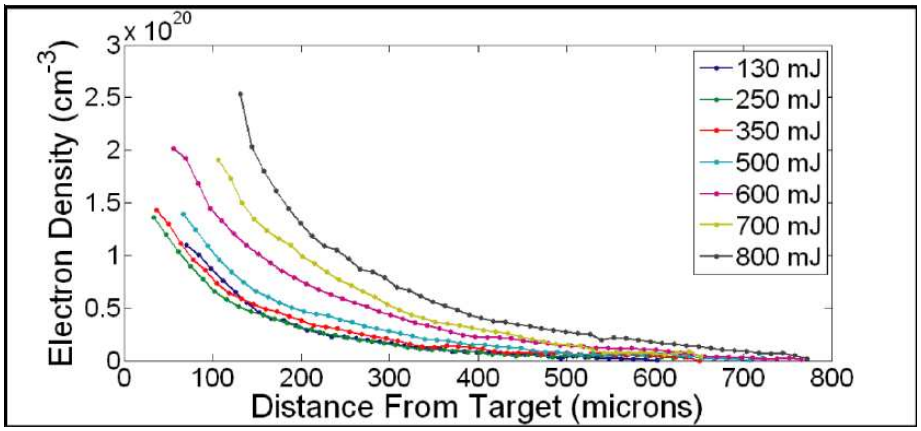

Figure 3.2: Spatial behaviour of the electron density for a variety of laser energies for an aluminium plasma at a delay time of 10 ns after the peak of the plasma producing laser pulse.

As one would intuitively expect, as the incident laser energy is increased, the electron density increases. Figure 3.13 shows the increase in electron density as a function of laser energy at a distance of 200 microns from the target.

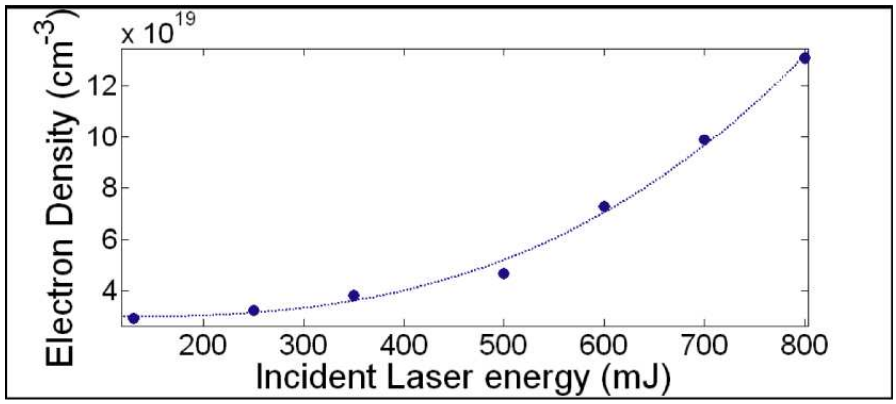

Figure 3.3: Variation of electron density with incident laser energy at a distance of 200 microns from the target surface at a delay time of 10 ns. The blue curve is a best spline fit to the data.

At the low end of the energy scale, an increase in the energy of the laser has a small effect on the electron density, increasing it only slightly. The same energy increment on the higher end of the scale has a significantly larger effect on the electron density. With the higher laser energies there is much more plasma ablation and ionisation and also, there is a stronger interaction of the preformed plasma with the trailing edge of the heating laser beam [5] which leads to higher degrees of ionization and a concomitant increase in electron density as shown in figure 3.3.

Presented in figure 3.4 below is the spatio-temporal evolution of the electron density for a laser produced aluminium plasmas created with an incident laser pulse energy of 600 mJ where the full capability of the interferometer with its high temporal and spatial resolution can be demonstrated.

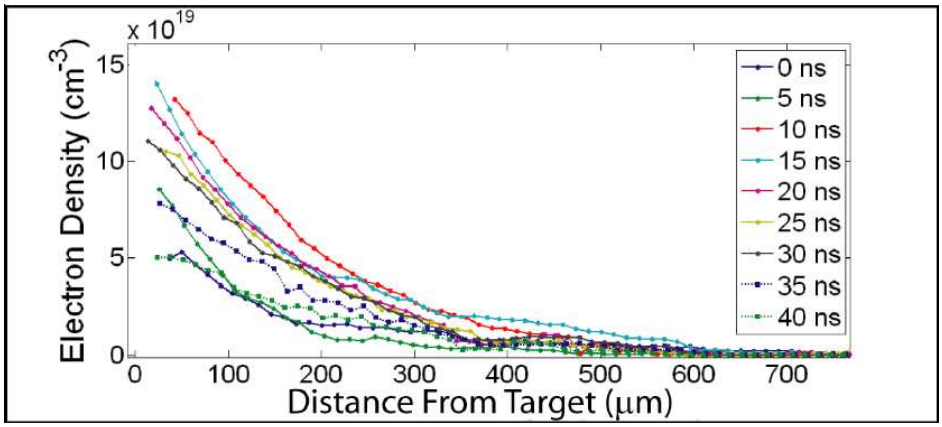

Figure 3.4: Spatio-temporal evolution of the electron density for a laser produced aluminium plasma with a pump pulse energy of 600mJ.

As can be readily seen from figure 3.4, the density of the plasma peaks at a delay time of 10 ns after the peak of the pump pulse. By 40 ns, the density of the plasma has dropped and its profile is similar to that at a delay time of 5 ns.

Interferometric experiments were performed on plasmas produced from a variety of targets. The purpose was to elucidate the variation of the electron density with atomic number, Z. This study not only helped with insight in designing later experiments but the dataset also provided a solid comparison for future interferometric studies of plasmas. The targets studied include, magnesium (Mg), aluminium (Al), silicon (Si), titanium (Ti), iron (Fe), copper (Cu), tin (Sn) and tungsten (W). The energy of the laser was kept at a constant value of 800 mJ and the spotsize was maintained at 100 μm during the experiments. The vacuum pressure was kept at better than 1×10^{-5} mbar for all experiments. Again, the one dimensional spatial distribution of the electron density profile has been analysed at a constant delay time of 15 ns for the various targets. This is shown in figure 3.5 below.

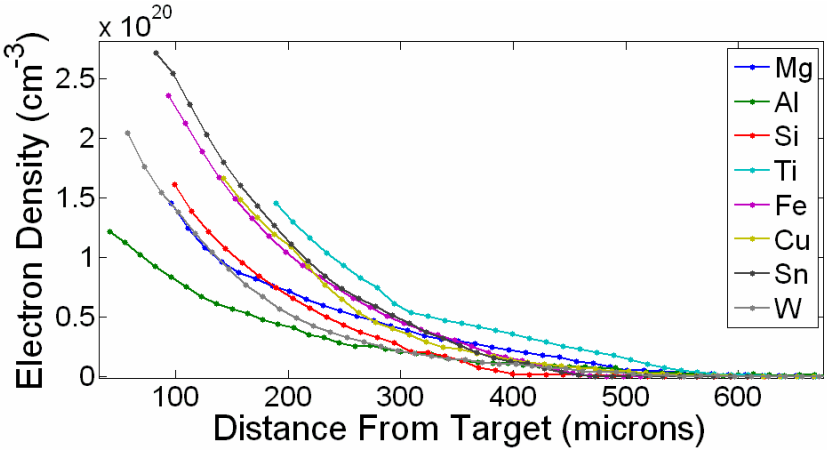

Figure 3.5: Spatial distribution of the electron density for different targets for a laser energy of 800 mJ.

It is clear from figure 3.5 that there is a dependence of the electron density on the target used. Using different targets can increase or decrease the density of the plasmas substantially with Sn and Ti producing the largest densities and Al and W producing the smallest densities. Figure 3.6 shows the variation of the electron density at a distance of 200 μm from the target as a function of a) atomic number (Z) and b) ionisation potential of the element.

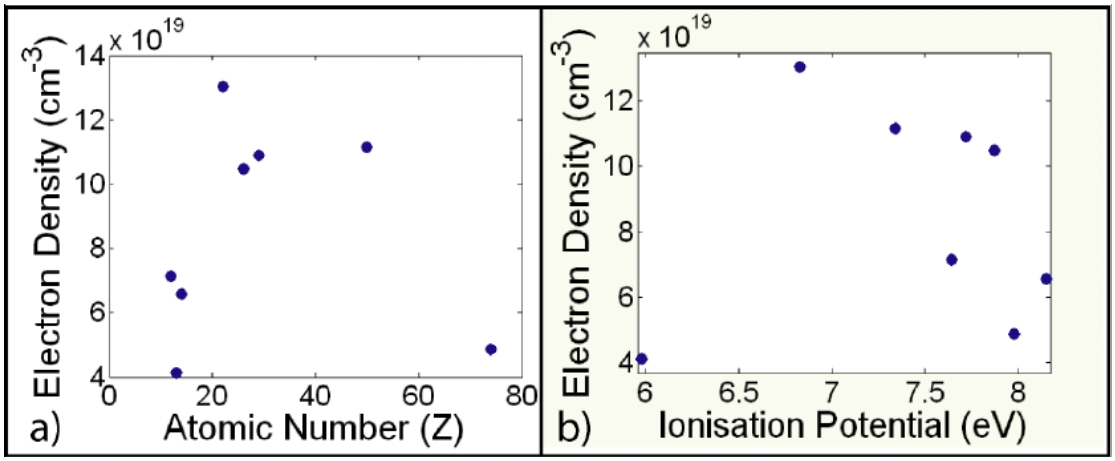

Figure 3.6: Variation of the electron density at a distance of 200 mm from the target at a delay time of 15 ns with a) atomic number Z, and with b) ionisation potential.

As can be seen from figure 3.6 there is no clear dependence of the electron density on atomic number or ionisation potential. Any dependence would require investigation of complex dynamics including laser absorption, ionisation,

recombination, expansion *etc.* for the various targets which was beyond the scope for these preliminary studies of single plumes in vacuum environments. The main objective of the project was to study plasma dynamics involving collisions (e.g. plasma – plasmas collisions and plasma – background gas collisions) but the results presented here provide a useful comparison for the vast and growing repository of studies (both experimental and theoretical) on single plasma plumes in vacuum. The results can also provide useful insight for the design of future experiments, e.g. target selection *etc.* This concluded the work on interferometry of single plumes in vacuum.

3.1.2: Gaseous Environments

The interferometer was, at this point, employed to study the effect of creating a single laser produced plasma in a gaseous atmosphere. This was the first major study to be published using this new experimental system [6] and aimed to probe the spatio-temporal behaviour of the electron density profile of a single plasma plume expanding into a gaseous atmosphere and compare it with that of a single plume expanding into vacuum. In this experiment, a blank silicon substrate was also placed in front of the plasma to gather the plasma debris in order to observe the effect that the presence of a background gas has on materials deposition when compared to a vacuum environment. The experiment was conducted in two different atmospheres, namely vacuum (vacuum maintained at better than 1×10^{-5} mbar) and high pressure O_2 (10 mbar pressure) and the results were compared.

Oxygen was chosen as the background gas for all the studies involving gaseous atmospheres because it is widely used in the area of materials growth using laser produced plasma (to be precise, Pulsed Laser Deposition – PLD). Studies involving the interactions of O_2 with laser produced plasmas is therefore of great interest in the PLD community [7, 8] as oxygen is widely used as a background ambient medium for

materials growth provides further motivation for carrying out such work. In this experiment, a slab of 99.99% pure zinc (of dimensions 25 mm × 25 mm × 1 mm) was chosen to be the target. Experiments on zinc and zinc oxide (ZnO) in oxygen rich environments are currently of major interest to the materials community. Specifically, considerable focus is currently been placed on the growth and characterisation of ZnO as it possesses excellent electrical, chemical and optical properties [9]. The fact that ZnO has a large excition binding energy of 60meV could also lead to lasing action at room temperature [10]. It also has a large bandgap, 3.37eV at room temperature and a concomitantly shorter wavelength, a very attractive trait for applications requiring shorter wavelength sources. These confer on ZnO potential applications in a wide range of areas such as UV opto-electronics devices [11], thin film transistor devices [12], anti-bacterial surfaces [13] and nano-structures [14]. Some groups have recently reported success in the production of ZnO nano-structures, for example nano-wires [15], nano-pyramids [16], and nano-dots [17] using PLD as the preferred method of growth. For these reason the first major experiments focused on this topical area of research.

During the experiment, a high precision gas flowmeter was used to introduce 99.999% pure O_2 into the vacuum chamber at a rate of 400 sccm (standard cubic centimetres per minute) creating a stable pressure of 10 mbar. The Zn target was mounted on a high precision in-vacuum motorised X-Z stage and set to move continuously during the period of deposition in order to avoid laser drilling of the target. Plasma debris was collected over a period of 30 minutes encompassing some 18000 laser shots at room temperature. The silicon substrate was mounted at a distance of 5 cm from the target surface and was orientated to face the laser produced plasma.

Interferograms of the plasma plumes were taken at 5 ns intervals up to a delay of 100 ns after plasma formation starting at the peak of the plasma producing pulse

(i.e. 0 ns time delay). In figure 3.7 the results from the laser interferometric study are shown for the two different regimes (vacuum and 10 mbar O_2). The area of interest in the interferogram selected for analysis (200 – 800 µm from target surface) is free from probe laser beam light absorption near the target surface where the electron density is greater than the critical density of the 532 nm probe laser beam.

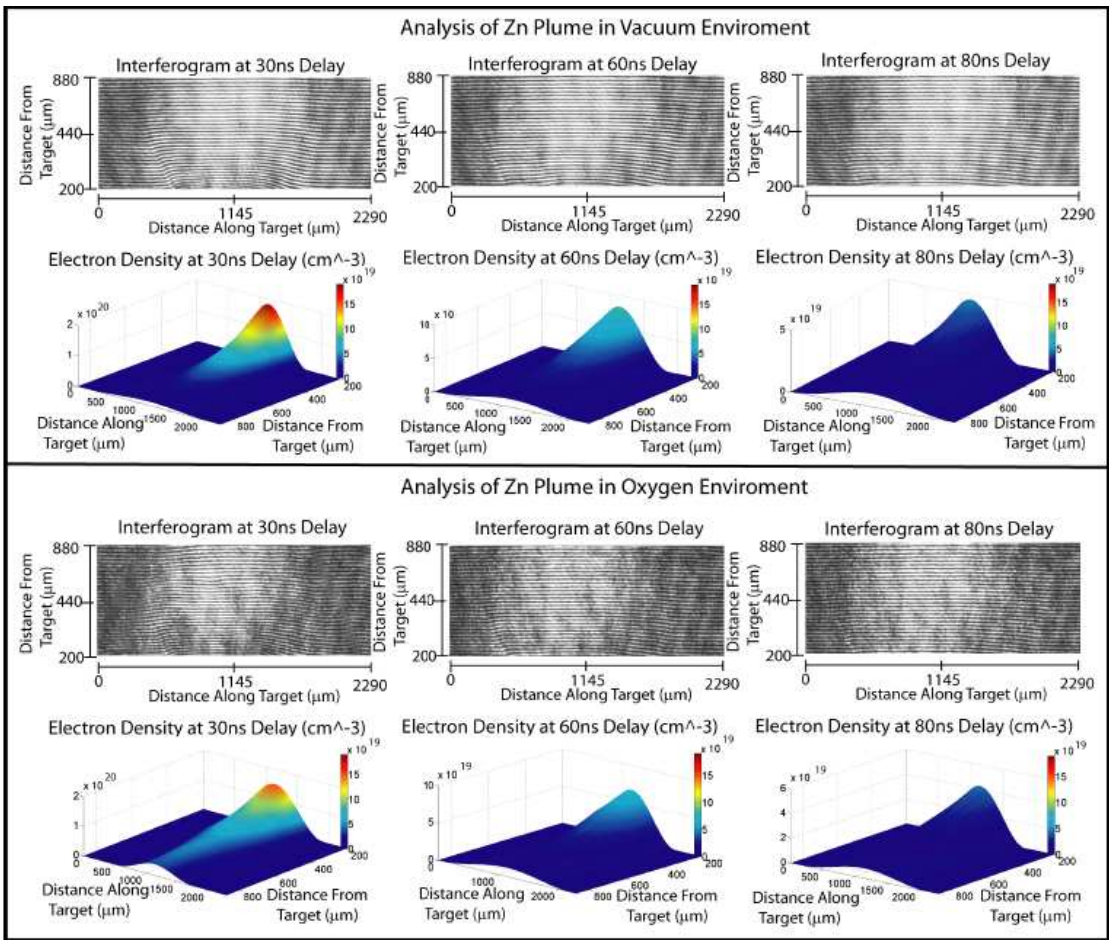

Figure 3.7: Comparison of results obtained from optical interferograms taken at delay times of 30, 60 and 80 ns for the Zn plume in vacuum and in O_2 at a pressure of 10 mbar.

What is immediately clear from figure 3.7 is that the peak electron density is very high in the early stages of the plasma lifecycle (≈ 30 ns) and lies just above 1×10^{20} cm^{-3} for both scenarios, albeit the vacuum case is slightly higher (≈ 20% higher at 200 µm see figure 3.2 (Top)). It is also apparent from figure 3.7, that the spatial profile

(normal to the target) of the electron density of the plumes is different for the vacuum and oxygen cases at early times (30 ns). This is emphasised in figure 3.8 where the 1D lineouts of the electron density normal to the target for vacuum and oxygen environments are compared for delay times of 30 ns (a) and 80 ns (b).

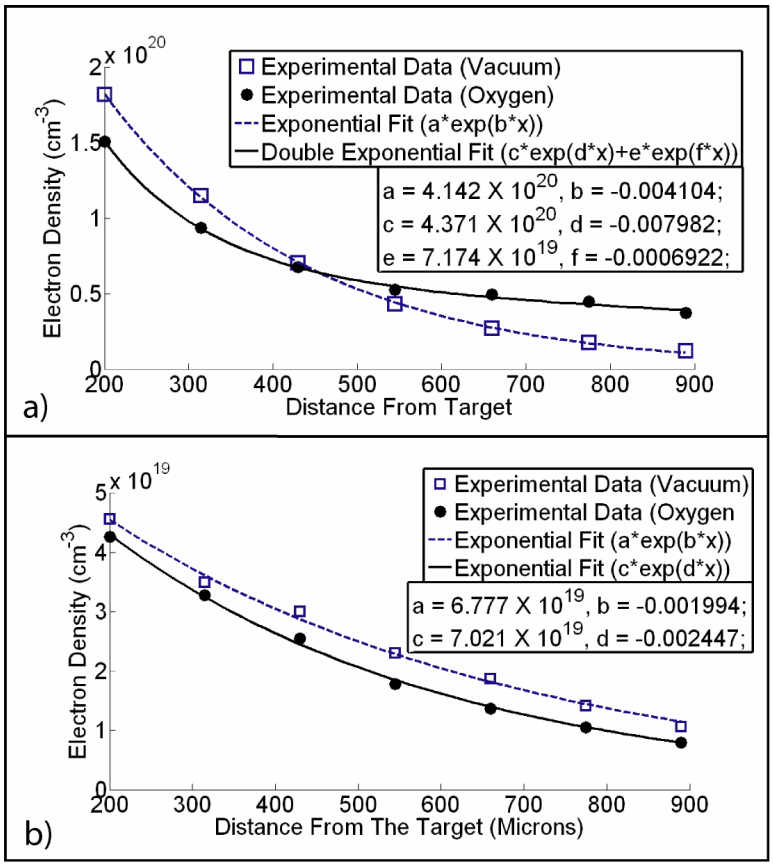

Figure 3.8: Comparison of the electron density profile normal to the target for vacuum and oxygen environments at a) Delay time of 30 ns, b) Delay time of 80ns. Exponential functions are fitted to the data and there is very good agreement between the fitted curves and the data points. The exact details of the fits along with fit constants are also supplied.

In the vacuum case a simple single exponential function makes a good fit to the experimentally observed electron density spatial profile, as the plasma is freely expanding in vacuum. To calculate the plasma density scale length we follow the same convention as Santala *et al.* [18] where they show that a first order estimate for the plasma density scale length, L, can be extracted by assuming an exponential electron density profile given by,

$$n_e(x) = n_{e,0} \exp\left(-\frac{x}{L}\right) \qquad \text{Equation 3.1.}$$

where $n_e(x)$ is the plasma density at a distance from the target, x, $n_{e,0}$ is an estimate of peak electron density, and L is the plasma density scale length.

Employing the method of Santala *et al.,* we obtain a value for the density scale length of 240 μm for the vacuum case at a time delay of 30ns. In the O_2 environment the density profile cannot be fitted with a single exponential. In fact a double exponential with a rapidly decaying term (scale length = 125 μm) superimposed on a slowly decaying term (scale length = 1440 μm) works best. It is proposed that these observations are due to the effects of the strong plasma confinement which can be expected when a plasma expands into a background ambient gas. With an increase in gas pressure, an increase in the frequency of electron and ion collisions with background atoms and molecules takes place [19], which results in increased ionisation, density, recombination and plasma emission [20-23]. In particular Lui *et al.* [20] and Leboeuf et al [21] have predicted, using 2D particle hydrodynamic plume expansion models, that as a result of the confinement of the plasma, the plasma density remains higher inside the shock wave than in the free expansion case. The studies shown here endorse the finding of Lui *et al.* and Leboeuf *et al.* More precisely, the electron density is found to be approximately three times higher at 900 μm from the target (figure 3.8 a)). To make a direct comparison between the spatial density profiles it is observed that in vacuum the density drops by a factor of 1/e at a distance of 240 μm from the target and it drops by a factor of 2/e at 495 μm. 1/e and 2/e values of 310 μm and 740 μm respectively are obtained in the in O_2 environment. So it can be clearly seen that there is a fast decay component and a slow decay component in the O_2 case at a time delay of 30 ns.

In figure 3.8 b), the spatial profiles of the electron density normal to the target are shown for both vacuum and oxygen ambient atmospheres at a time delay of 80 ns. Although the density in the vacuum case is slightly higher, the main observation here is that both profiles can be fitted using a single exponential function. From these fits density scale lengths of 500 μm and 410 μm are obtained for the vacuum and oxygen atmospheres respectively at a time delay of 80 ns. It is clear that by 80 ns the shock wave, behind which the density has grown, has dissipated sufficiently for its confinement effect to have largely disappeared in the region close to the target.

The temporal evolution of the electron density at a distance of 200 μm from the target is given in figure 3.9 for both vacuum and O2 environments.

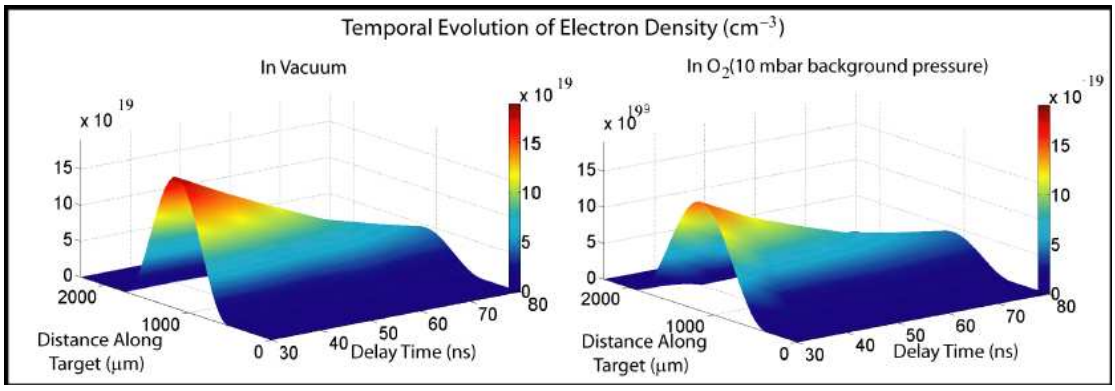

Figure 3.9: Temporal evolution of the electron density in the plasma plume at a distance of 200 microns from the Zn target surface.

It is clear from figure 3.9 that the electron density for the Zn plume expanding into vacuum, decays much more quickly than in the oxygen ambient atmosphere case. This makes physical sense as without a background gas present the plume expansion is faster and so the density drops more rapidly.

As reported by Lui *et al.* [20] and Leboeuf *et al.* [21], the key signature of this plasma confinement is the development and evolution over time of shock waves as the plasma plume expands into the gaseous environment. The shock wave acts as a compressive layer of gas formed at the interface between the plasma plume and the

background gas and is observed to expand outward normal to the target over time. It manifests itself in the interferograms as a blurring of the fringes due to the gas compression in the region. The blurring of the fringes originates from the fact that the refractive index of the compressed gas layer changes rapidly, so rapidly in fact, that the temporal resolution of the interferometer (4 ns) is not sufficient to resolve the prompt increase in refractive index of the layer. This causes a blurring of the fringes which can then be exploited as a signature of the spatial distribution of the compressed layer of gas. Shown in figure 3.10 are interferograms taken at time delays of 0, 5 and 10 ns after the peak of the pump laser beam. The spatial distribution of the compressed layer of gas is clearly visible and is observed to develop rapidly over time.

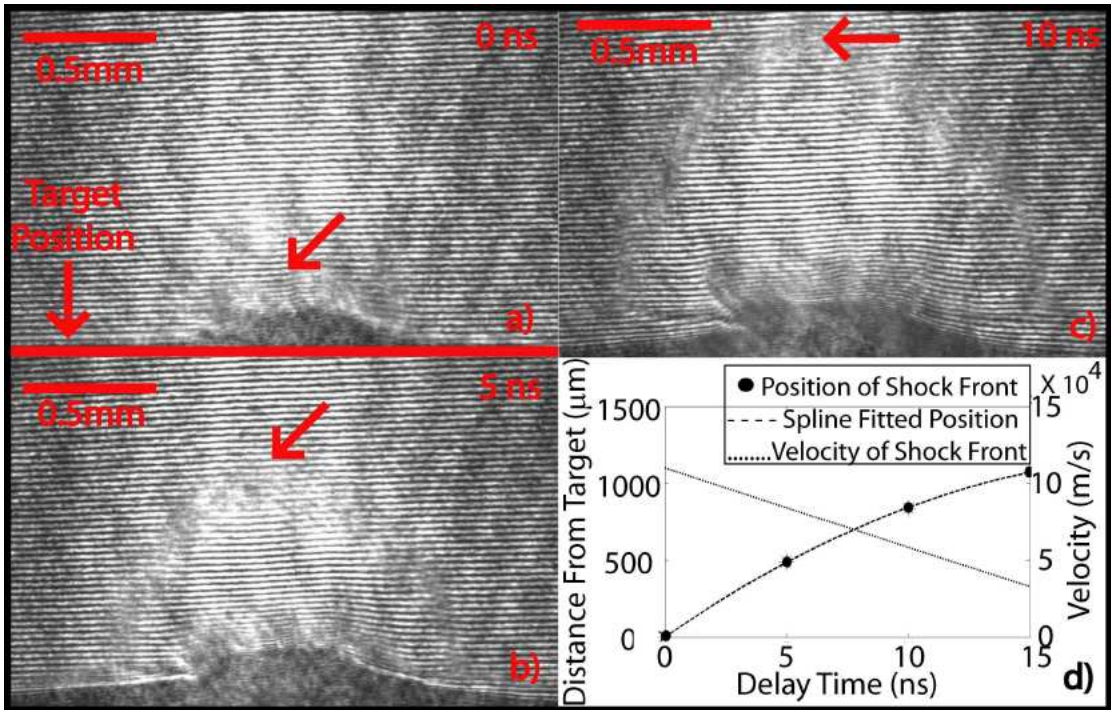

Figure 3.10: Comparison of interferograms for a): 0 ns, b): 5 ns and c): 10 ns with the shock front. The arrow marks the peak (largest distance from target) of the shock front. d): Plot of the position of the leading edge of the shock wave at a function of time with a fitted spline curve and the resulting velocity of the shock wave.

Although these shock waves that occur when plasma expands into gaseous atmospheres, are well documented in the literature (*e.g.* [19, 23]), these results reveal the creation of this shock wave at the earliest times of the plume lifecycle starting at

the peak of the laser producing pulse. A sharpening of the shock wave (the so called "snowplow" effect) is observed in the 10 ns interferogram which has been predicted [21, 25] and observed at later times (100's of ns) using fast imaging [24]. The observations here show its formation at very early times. In figure 3.10 d) the position of the leading edge of the compressed layer as a function of time is plotted. One observes that the shock wave starts with quite a large velocity of 1.1 x 10^5 ms^{-1} but over time drag causes a deceleration and the velocity drops to 3.2 x 10^4 ms^{-1}. This deceleration has also been observed and predicted previously in the literature [20, 21] and is caused by a viscous force causing drag on the particles as it expands in the background gaseous environment although the observations presented here are at very early times.

In figure 3.11, Scanning Electron Microscope (SEM) images taken of the silicon substrates for the two samples grown are shown for a) debris collected on the silicon substrate in a vacuum atmosphere and b) debris collected on a silicon substrate in an O_2 rich environment.

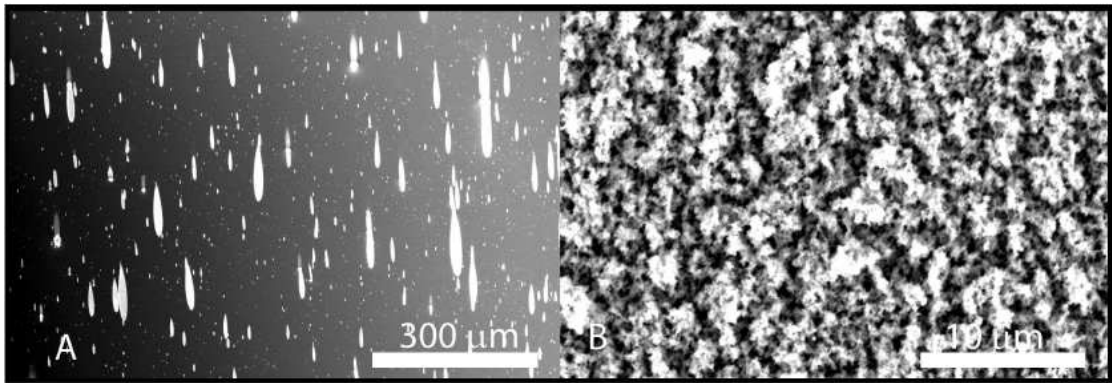

Figure 3.11: A: SEM images of surface of Si substrate after deposition of a Zn plume *in vacuo*. B: SEM image of surface of Si substrate after deposition of a Zn plume with O_2 at a pressure of 10 mbar as the background gas.

From the SEM analysis it can be seen that there are quite different mechanisms of growth involved in the two distinct regimes. Under vacuum, in effect mainly plasma debris, *i.e.* melted target material, is observed on the substrate. This would be expected as the Zn plume is freely expanding into a vacuum with nothing to buffer the plasma blow-off that follows from the violent interaction at the target surface. With O_2 as a background gas, however, a carpet-like, nano-structured layer has developed on the surface of the Si substrate. This is due to the interaction of the Zn plume with the ambient O_2 gas. It is proposed that the ambient gas acts as a buffer assisting the growth of clustered structures in the plasma plumes which are subsequently deposited in a more orderly fashion onto the surface of the substrate. The result is related to the analysis of the interferometry where it has already been seen that there is a very rapid interaction between the ambient gas and the plasma plume resulting in more moderate plasma gradients likely to be signatures of the more placid plume expansion than in the vacuum case.

3.2: Interferometry and Shadowgraphy

After performing the experiments involving laser plasma creation in gaseous atmospheres outlined in Section 3.1.2, it was observed that laser interferometry could be used as a diagnostic tool for analysing the expansion of shock wavefronts present after the creation of a laser produced plasma in a gaseous atmosphere. It is worth noting that in the literature, one of the main diagnostic tools employed for analysing such compressive layers is the shadowgraphy diagnostic technique [26, 27]. The brightness profile in a shadowgram is responsive to the second spatial derivative of the refractive index. As already described in Chapter 1, variations in the refractive index in the field of view of the shadowgram manifest themselves by the redistribution of light intensity. In this way the development of compressive gas fronts can be tracked and measured. Figure 3.12 shows an example of a shadowgram taken using the

experimental setup employed for the studies presented in this thesis. The experimental setup has been described more fully in Section 2.4.2.

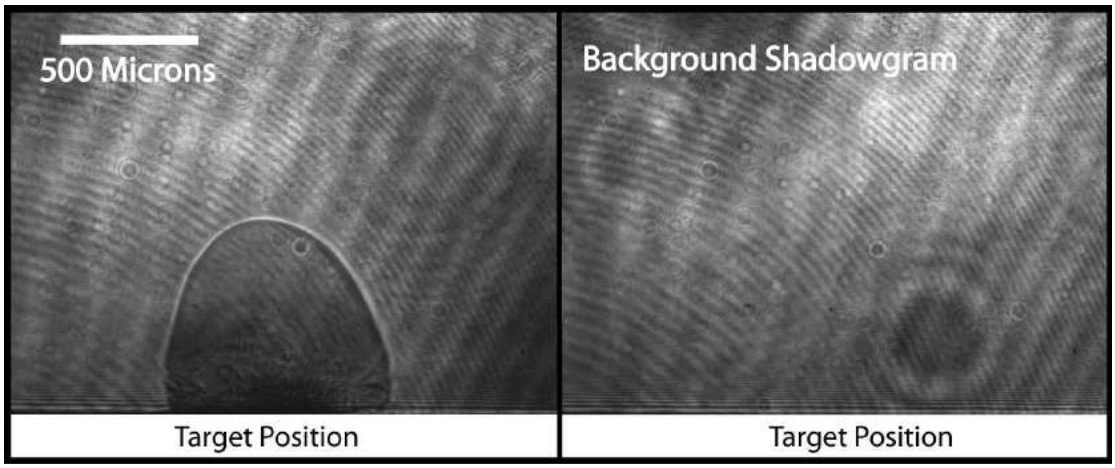

Figure 3.12: Left: Sample shadowgram taken 30 ns after the peak of the pump laser pulse. The incident laser pulse had an energy of 100 mJ and the background pressure was 1000 mbar of air. The outline of the shock front at the plasma – gas interface is clearly visible. Right: Background shadowgram with no plasma present for reference. The visible variations in intensity are inherent in the probe beam and induced by the intervening optics.

Figure 3.12 shows a shadowgram taken 30 ns after the peak of the pump laser beam (100 mJ in 6 ns FWHM). The target comprised of a flat slab of aluminium of dimensions 25 mm × 25 mm × 1 mm. Also shown for comparison is a blank shadowgram with no plasma present for comparison. The pressure of the background gas was 1000 mbar of air.

Given the ability to perform both shadowgraphy and interferometry with the one setup, it was logical to perform some experiments which compared the ability of shadowgraphy and interferometry as diagnostic tools for the purpose of compressive layer observations. Interferometric and shadowgraphic experiments were performed on single laser produced plasma expansion into gaseous atmospheres for a variety of incident laser energies and a variety of background gas pressures.

Presented in figure 3.13 below is a comparison of interferograms and shadowgrams for single plasma expansion into a background gas at three different

delay times (20, 100 and 200 ns) after the peak of the pump laser pulse. The experimental conditions are the same as those used to obtain figure 3.12. In short, the incident laser pulse had an energy of 100 mJ focused to a spotsize of diameter 100 μm on the surface of a flat slab of Al in 1000 mbar of background air. The target was moved after each laser pulse to reveal a new surface.

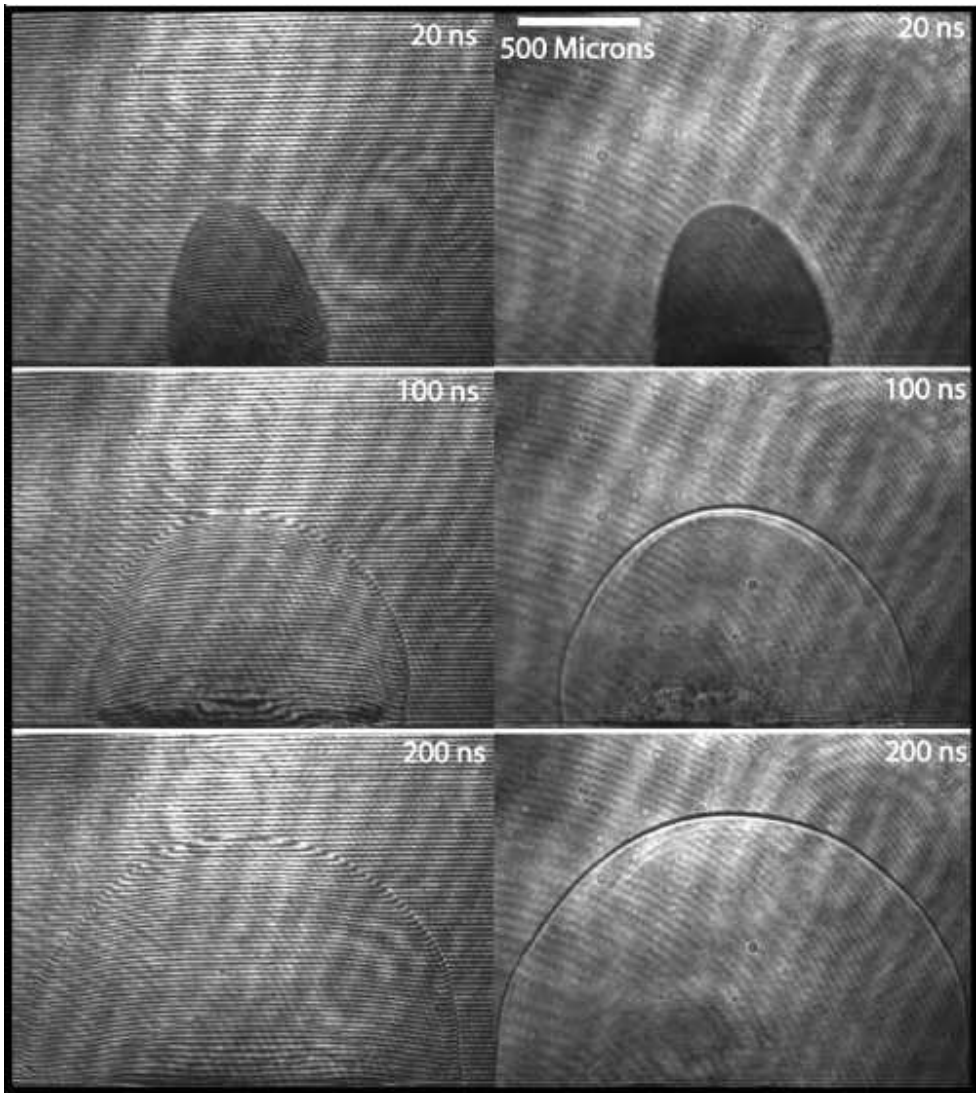

Figure 3.13: Comparison of interferograms (left panels) with shadowgrams (right panels) at 3 different delay times, 20, 100 and 200 ns after the peak of the pump laser pulse. The incident laser beam had an energy of 100 mJ and the background gas comprised of 1000 mbar of air. The development of the shockwave is clearly visible in both the interferograms and shadowgrams.

As a result of the high spatial and temporal resolution of both the interferograms and shadowgrams, it was possible to extract the spatio-temporal evolution of the shockfront (defined here to be the locus of points of the shock wave furthermost from the target surface). This has been done for the above experiment presented in figure 3.13. The results are plotted in figure 3.14 a) where the position of the front of the shockwave is plotted as a function of delay time after plasmas creation. The shock is analysed for varying delay times between 5 ns and 300 ns from the interferograms (blue dots) and shadowgrams (red dots). Simple spline fits (solid lines) are also plotted. Both techniques show a consistent behaviour in the spatio-temporal evolution of the shockfront.

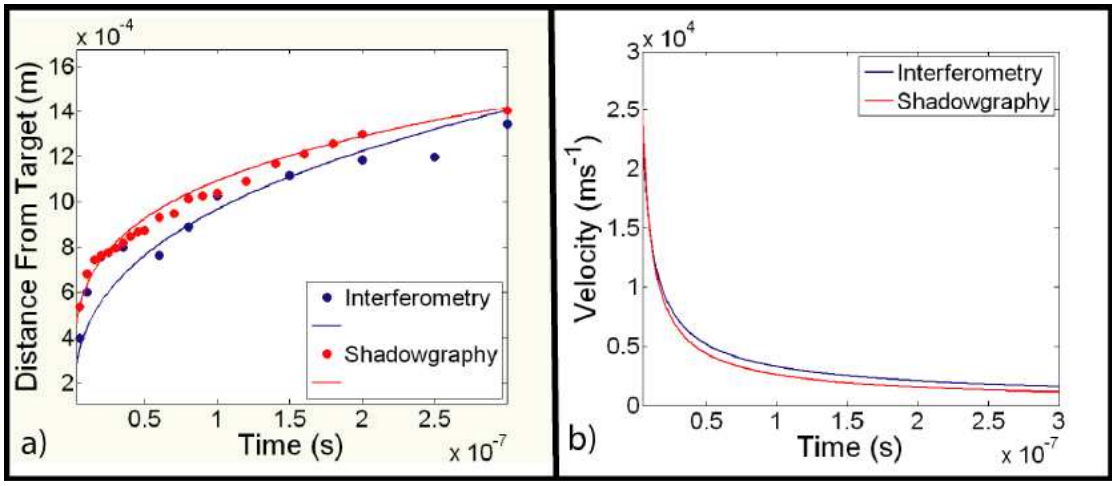

Figure 3.14: a) Comparison of the spatio-temporal evolution of the front of the shockwave as observed using interferometry (blue dots) and shadowgraphy (red dots) along with best fit spline curves. b) corresponding temporal behaviour of the velocity of the shock front extracted from the interferometric (blue) and shadowgraphic (red) data.

Shown in figure 3.14 b) is the temporal evolution of the velocity of the shock front obtained from an analysis of the interferograms (blue curve) and shadowgrams (red curve). It is clear that the interferometry data is consistent within reason with that of the shadowgraphy. The extracted velocities from the interferometry analysis and shadowgraphy analysis are in very good agreement with each other. These results are also consistent with those from similar experiments published in the literature, for example, Thiyagarajan *et al.* [27] have found shock front velocities in the region of 10's

of kms^{-1} for similar experimental parameters which are very much in keeping with the observations presented here.

It is clear from the results shown above in figure 3.13 and figure 3.14 that interferometry can be utilised to diagnose the spatio-temporal development of the compressive gas layers formed when plasmas expand into background gases. There remains the question of whether there is any benefit of employing interferometry as a diagnostic tool for such applications compared to shadowgraphy which is currently the main shock wave diagnostic tool.

There are limitations to the shadowgraphic technique, in that, when the background gas pressure becomes relatively low (defining low background gas pressure here as between ≈ 1 mbar and ≈ 100 mbar), it becomes more difficult to detect the compressive gas layer. This is because there is less compression at the plasma – gas interface and so the variation of refractive index at the shock front decreases with decreasing background gas pressure. Therefore, when employing shadowgraphy as a diagnostic technique, the re-distribution in image brightness due to the change in refractive index in the compressed gas layer is significantly reduced and is hence difficult to detect in low pressure regimes.

In these low pressure regimes the velocity of the compressive gas layers are also noticeably higher, up to an order of magnitude in some cases, than the velocity of compressed gas layers created at higher background pressures (100's - 1000 mbar). This also makes it difficult to detect the compressed gas layers at lower pressures using shadowgraphy.

For these reasons, further investigations of compressive gas fronts using interferometery and shadowgraphy focused on the relatively lower background ambients comprised of O_2 at pressures in the regime of 1 - 100 mbar with the objective

of comparing the viability of diagnosing gas layers more accurately and extensively at these intermediate background pressures. Presented in figure 3.15 are the results from one such experiment where interferometery and shadowgraphy were performed on a laser produced plasma expanding into a background gas maintained at a pressure of 10 mbar. The energy of the incident laser beam was 100 mJ with a focal spotsize of 100 μm. The target was a flat slab of aluminium and the background gas was oxygen. The target was moved to reveal a new surface after each laser shot.

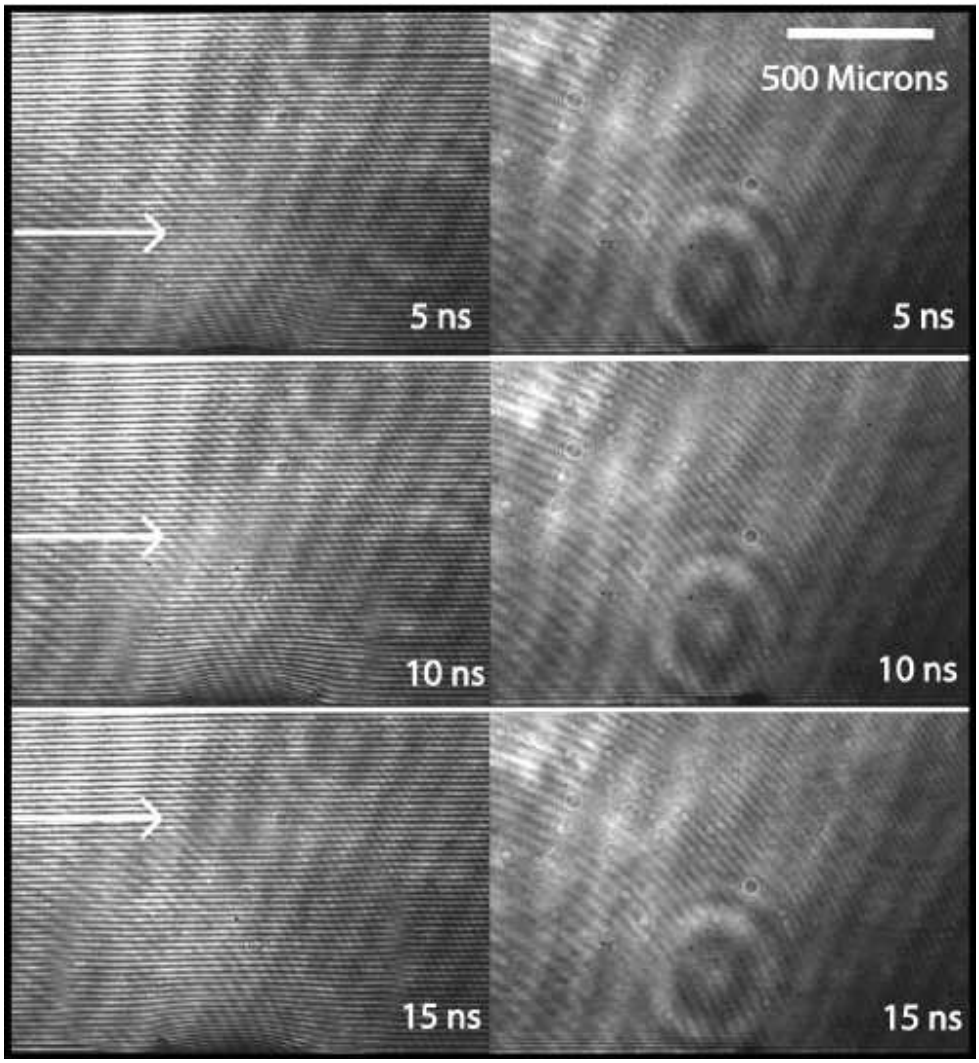

Figure 3.15: Comparison of interferometry (left panels) with shadowgraphy (right panels) of a laser produced aluminium plasma expanding into a background gas of oxygen maintained at a pressure 10 mbar at 3 different time delays after the peak of the pump laser pulse, namely 5, 10 and 15 ns. The white arrows in the interferograms point out the front of the compressive gas layer.

On close inspection of figure 3.15, some very interesting findings were revealed. Looking at the shadowgrams (right panels), there is no evidence of a compressive gas layer expanding at the plasma – gas interface. On the other, when looking at the interferograms (left panels) there is some evidence of a compressive gas layer rapidly expanding outwards from the target. As already described, the compressive gas layer manifests itself in the interferograms as a blurring of the fringes. This fringe blurring is more easily observable than very small redistributions in illumination levels that occur in shadowgraphy. However, it can also be argued that the blurring of the fringes is also difficult to observe and certainly needs very close inspection to reveal the presence of the compressive layer. Fortunately, it is possible to enhance the signature of the gas layer. This can be done by employing a simple "Find Edges" algorithm which can detect changes in image brightness to enhance features such as discontinuities by differentiating the image. This can be done using any widely available image processing package but the processing package employed during this study to perform the find edges algorithm was a freeware software package called "ImageJ" [28]. Figure 3.16 shows comparison of the interferogram and shadowgram from figure 3.15 at a time delay of 10 ns before and after applying the find edges algorithm.

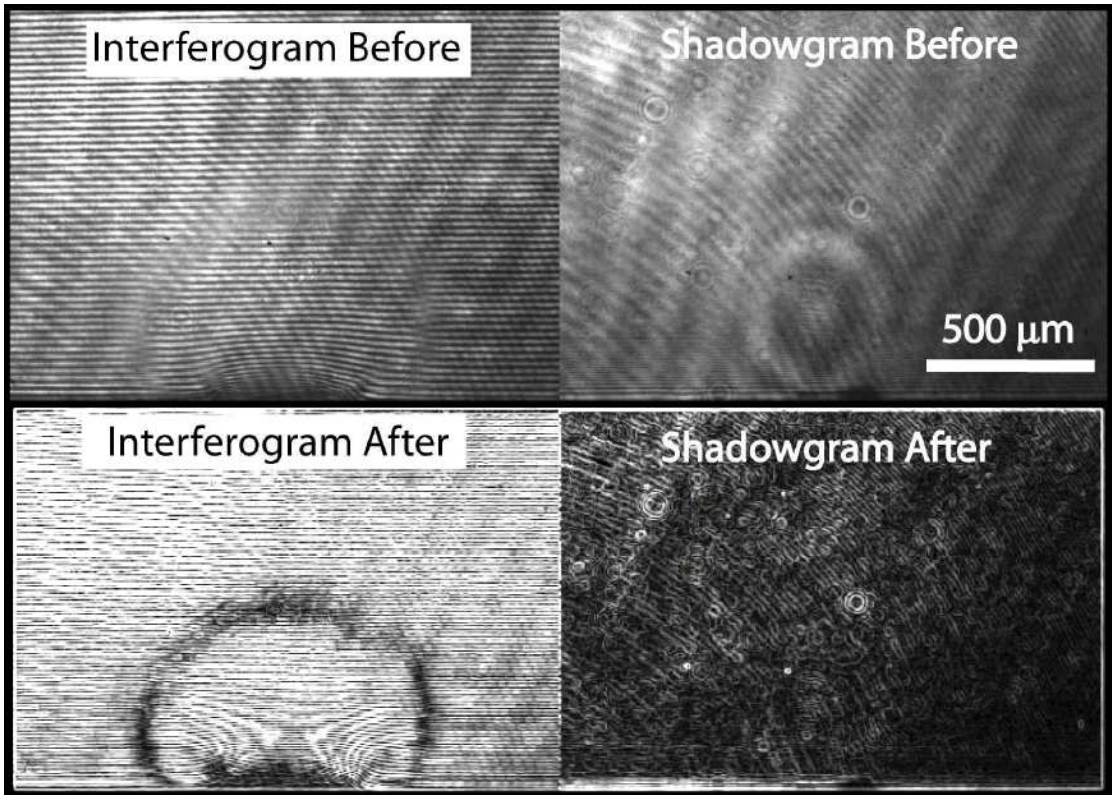

Figure 3.16: Comparison of the interferograms (left) and shadowgrams (right) from figure 3.10 taken at a time delay of 10 ns before and after applying the 'find edges' algorithm in the ImageJ image processing software package.

The presence of the shock wave is now much clearer following application of the find edges algorithm. The algorithm enhances the discontinuities of the blurred fringes at the position of the compressive gas layer. No evidence of the layer is visible from the shadowgram even after applying the algorithm.

With the ability to observe the expansion of compressive gas layers in these plasma regimes, it is possible to extract the spatio-temporal evolution of the front of the compressive gas layer. This spatio-temporal analysis, performed on the experimental data in figure 3.15 is presented in figure 3.17.

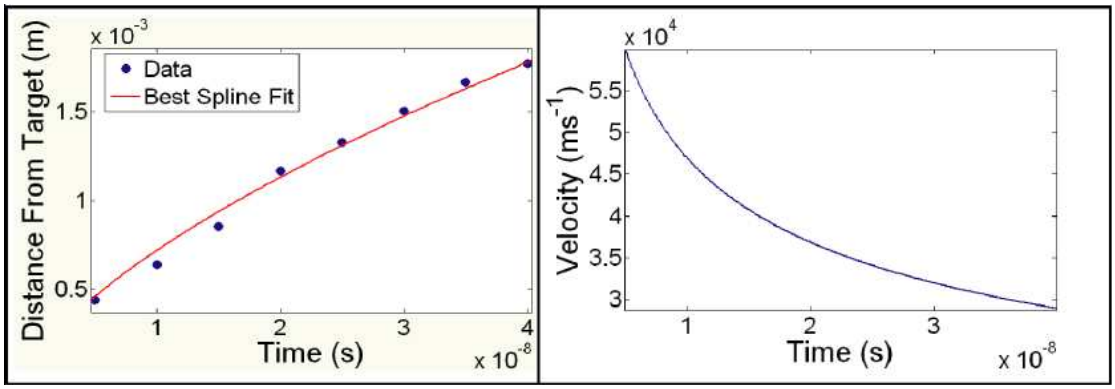

Figure 3.17: Spatio-temporal analysis of the interferograms presented in figure 3.15. Left: Distance Vs. time plot of the peak position of the compressive layer (blue dots) between 5 and 40 ns after the peak of the pump laser pulse. Also shown is a best fit curve to the data (solid red line). Right: Velocity of the compressive layer (extracted from fitted curve in left panel). The background pressure is 10 mbar.

Comparing figure 3.14 to figure 3.17, i.e. same incident laser pulse but in a background pressure of 1000 mbar, it is clear that the velocity of the shock wave in 10 mbar is much higher. In fact, the peak velocity of the compressive layer at a gas pressure of 10 mbar is just over a factor of 2 higher than that in the same ambient gas at a pressure of 1000 mbar. The shock front present in 1000 mbar pressure background gas remains in the field of view of the interferogram up to a delay time of 300 ns after the peak of the plasma producing laser pulse. In contrast in a gaseous atmosphere at a pressure of 10 mbar, the shock wave present in the interferogram remains in the field of view of the camera only for a few 10's of nanoseconds.

By employing interferometry as the diagnostic tool to analyse compressive gas fronts formed during laser plasma expansion into a background gas, it is possible to probe background pressure regimes where the reliability of shadowgraphy begins to fade. Interferometery has, in fact, been employed in pressures as low as 1 mbar, where the faint signs of the expansion of a compressive gas front are still visible in the corresponding interferogram with no visible indication whatsoever in the shadowgram. The results of one such experiment are shown in figure 3.18 below. In this experiment an incident laser beam of energy 100 mJ was again focused onto a flat slab of

aluminium, in a background pressure of 1 mbar of O_2. This creates a very weak compressive gas layer that expands extremely rapidly. The results from shadowgraphy are also shown for comparison.

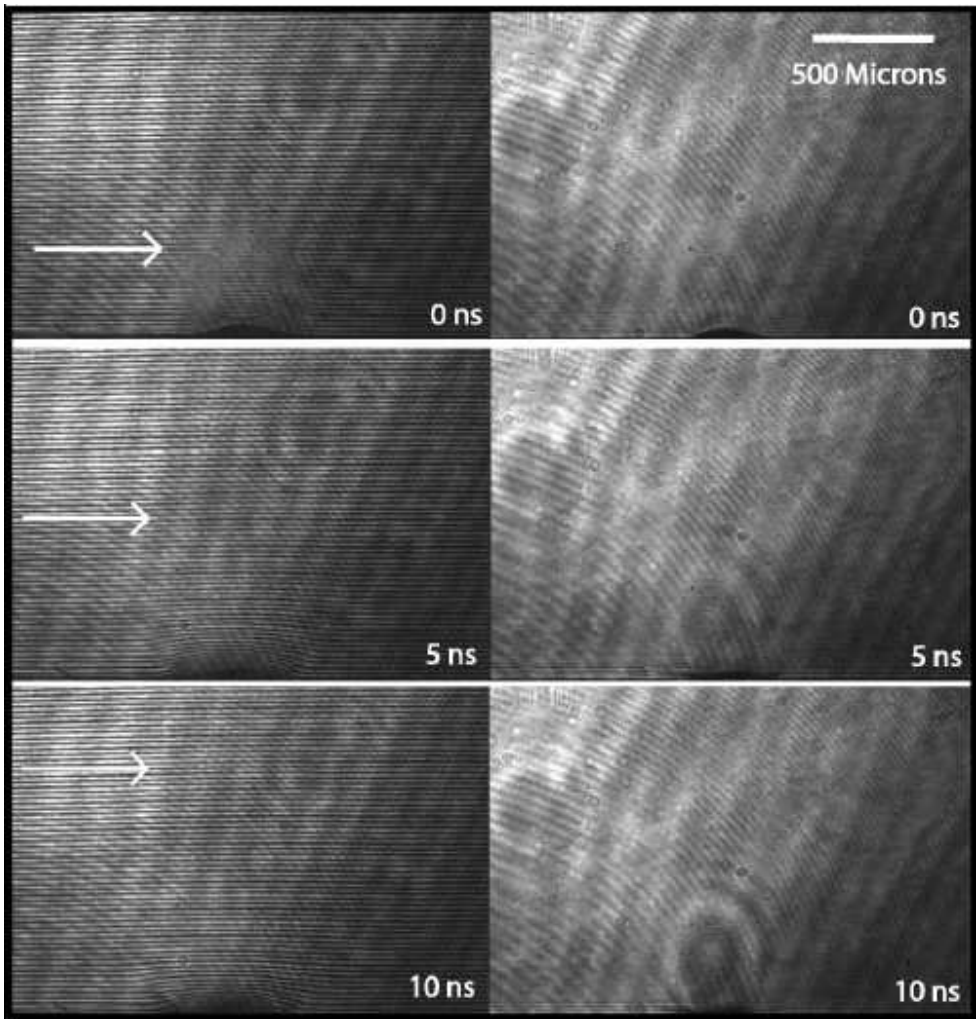

Figure 3.18: Comparison of interferograms (left panels) and shadowgrams (right panels) for a laser produced plasma expanding into a background oxygen gas pressure of 1 mbar. The white arrows mark the faint signature from the front of the compressive layer.

Upon application of the find edges algorithm, the weak compressive locus of the gas front becomes visible. At later times (> 10 ns) under these experimental conditions the signature of the compressive layer becomes harder to detect as it does not produced blurred fringes with discontinuities, rather, the expansion of the layer can be detected due to the subtle bending of the fringes as a result of the presence of

the compressive layer. Figure 3.19 shows a comparison of the interferograms and shadowgrams presented in figure 3.18 after application of the find edges algorithm.

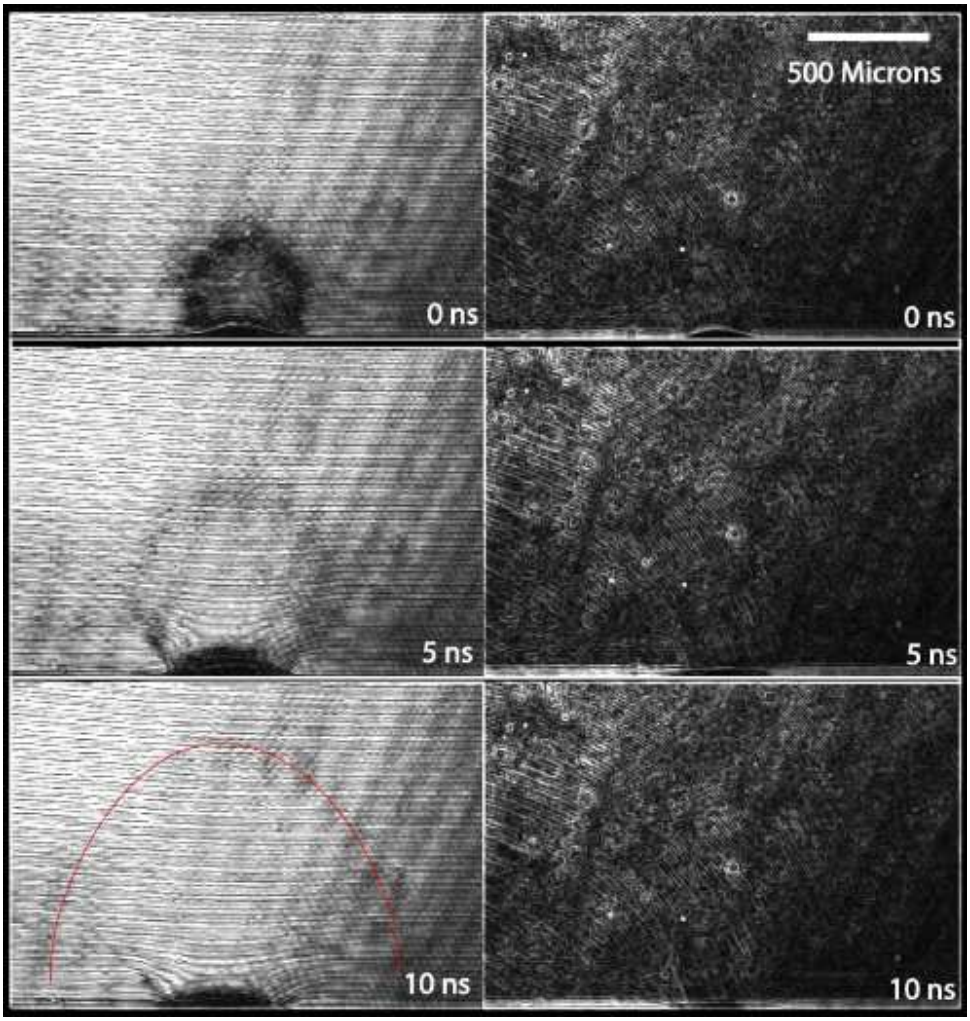

Figure 3.19: Comparison of the interferograms and shadowgrams from figure 3.12 (1 mbar) following application of a find edges algorithm. The compressive gas front visible as the red curve in the 10 ns interferogram serves to further highlight the position of the fringe shifts due to the presence of the compressive gas layer.

Once again it is possible to obtain the spatio-temporal evolution of the weak compressive gas front from the interferometry study in 1 mbar of background gas. This is not possible using shadowgraphy. The results are shown in figure 3.20 below.

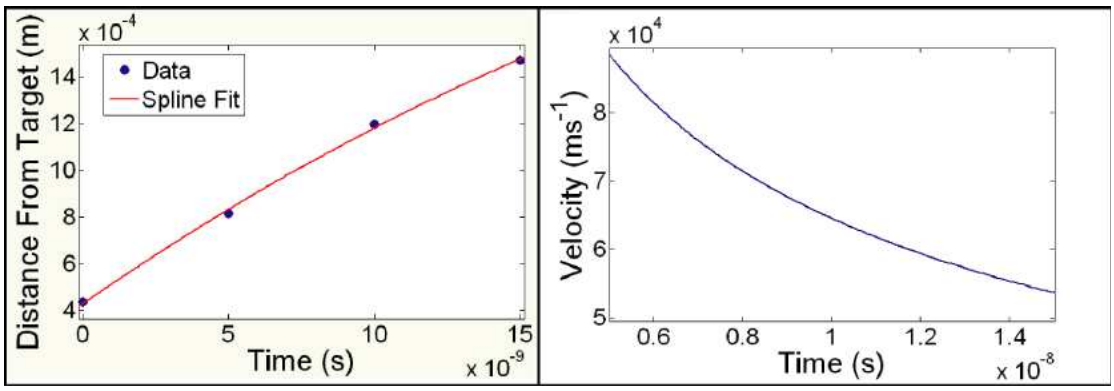

Figure 3.20: Spatio-temporal analysis of the interferograms presented in figure 3.12. Left: Displacement of the peak position of the compressive layer (blue dots) in the range 0 to 15 ns after the peak of the pump laser pulse. Also shown is a best fit curve to the data (solid red line). Right: Velocity of the peak of the compressive layer (extracted from fitted curve in left panel). The background gas was O_2 at a pressure of 1 mbar.

It is evident again here that the velocity of the compressive layer has increased by a significant amount. The peak velocity is, in fact, about a factor of 3 times larger that of expansion into a background pressure of 1000 mbar. Using interferometry, one is able to gain insight into the dynamics of plasma-gas interactions that are otherwise difficult observe. Further it will be shown later on that it is possible to observe high velocity compressive gas fronts travelling at speeds of over 100 kms^{-1}.

The interferometric analysis of the spatio-temporal expansion of compressive gas fronts presented above has been performed for a variety of background gas pressures (O_2 at pressures of 1, 10 and 100 mbar and air at a pressure of 1000 mbar) and pump laser energies (100, 200, 400 and 600 mJ). Before the results are presented, a comparison is made between the compressive gas layer visibility in the interferograms and shadowgrams for the different experimental conditions studied. The compressive gas layer visibility is summarised in table 3.1.

Table 3.1: Visibility of Compressive Gas Layer

Gas Pressure	Diagnostic	100 mJ	200 mJ	400 mJ	600 mJ
1 mbar O_2	Interferometry	✓	✓	✓	✓
	Shadowgraphy	×	×	×	×
10 mbar O_2	Interferometry	✓	✓	✓	✓
	Shadowgraphy	×	×	×	✓
100 mbar O_2	Interferometry	✓	✓	✓	✓
	Shadowgraphy	×	×	✓	✓
1000 mbar air	Interferometry	✓	-	-	-
	Shadowgraphy	✓	-	-	-

Table 3.1: Comparison of the visibility of the compressive gas layer using interferometry and shadowgraphy for various experimental parameters. Legend: ✓ = Visible, × = Not Visible, - = Experiment Not Possible (due to gas breakdown).

Presented next in figure 3.21 is a comparison of spatio-temporal evolution of the compressive layer for a variety of gas pressures with a constant incident pump laser energy of 100 mJ along with a comparison of the extracted velocity profiles.

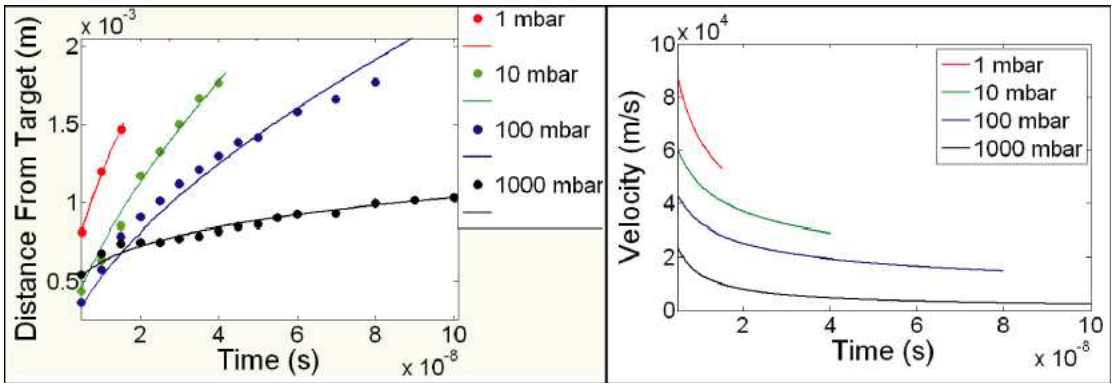

Figure 3.21: Left: Comparison of the spatio-temporal evolution of the shock front at varying background gas pressures of 1, 10, 100 (O_2) and 1000 mbar (air) at a constant laser energy of 100 mJ. Also shown are the best spline curve fits. Right: The temporal evolution of the velocity extracted from the spline fits.

Close inspection of figure 3.21 reveals that at a gas pressure of 10 mbar, the velocity of the compressive layer at 10 ns after the peak of the plasma producing laser is ≈ 25% lower than that created in a pressure of 1 mbar. Similarly, the velocity of the compressive gas layer in 100 mbar is 30% lower than that in 10 mbar and finally, the velocity of the shock front in a background pressure of 1000 mbar is 60% lower than that in 100 mbar.

The same analysis as that presented in figure 3.21 has been performed for incident laser energies of 200 and 400 mJ for experiments in O_2 at pressures of 1, 10 and 100 mbar. These results are shown in figure 3.22.

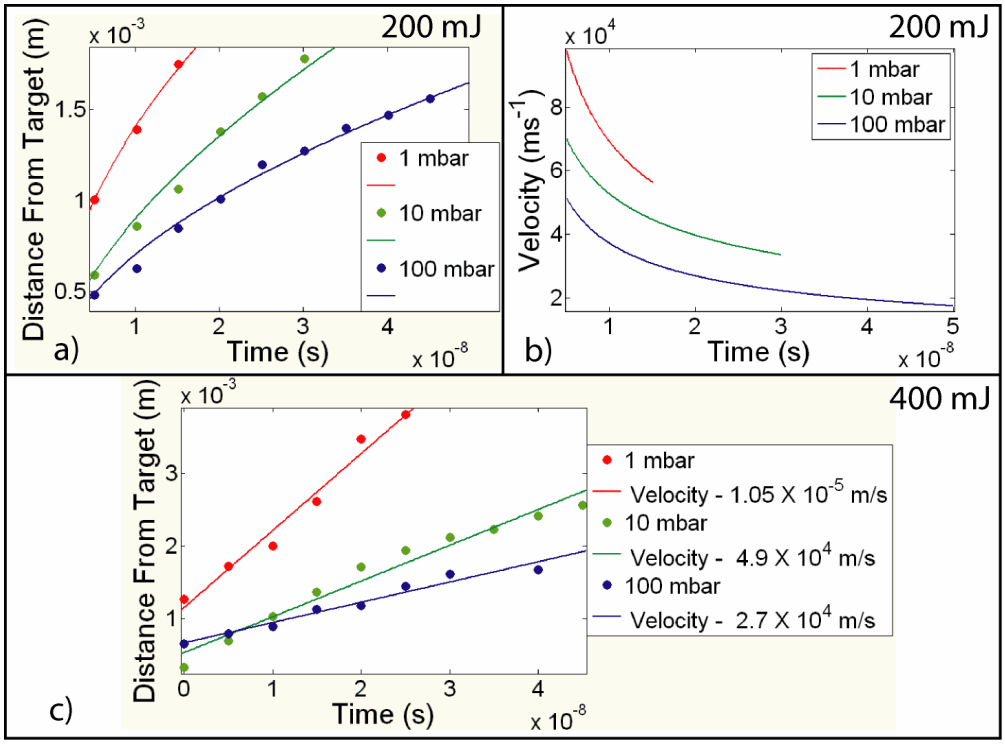

Figure 3.22: Spatio temporal analysis of the compressive layer of gas for laser energies of 200 mJ and 400 mJ. a) Evolution of the shock front position as a function of time for an incident laser energy of 200 mJ and background gas of O_2 at pressures of 1 mbar, 10 mbar and 100 mbar. b) Extracted velocity profiles from best curve fits in a). c) Temporal evolution of the compressive gas layer for an incident laser energy of 400 mJ and background gas pressures of 1 mbar of O_2, 10 mbar and 100 mbar. Included are extracted velocities from best straight line fits.

The evolution of the compressive layer of gas created with a laser energy of 200 mJ follows very much the same profiles as that created using 100 mJ (figure 3.15) with the exception that the velocity of the compressive gas layer is somewhat higher for all gas pressures. This is expected as the pump laser energy is doubled. In particular the velocity of the compressive gas layer created by the 200 mJ pulse in 1 mbar background pressure is 9 % higher than that created by the 100 mJ pulse in the same background gas. Similarly, in 10 mbar background gas pressure, the velocity of the compressive layer of gas created by the 200 mJ pulse is 12 % higher than that of the 100 mJ pulse and in 100 mbar it is 13 % higher.

Finally, considering the compressed layer of gas created by the 400 mJ pulse, it is clear that the velocity is much larger than the previous observations. Firstly, with the laser energy at 400 mJ in a background pressure of 1 mbar, the velocity of the compressed gas layer reaches speeds of over 100 kms^{-1}, nearly an order of magnitude greater than in the previous observations (figure 3.15). In these cases at such early times the best fit was a straight line fit from which the velocities were obtained.

3.3: Summary

In this section, the experimental results from interferometric and shadowgraphic probing of single laser produced plasmas were presented. Firstly the results from interferometry of single plumes in vacuum environments were presented and typical densities in the range of $10^{18} – 10^{20}$ cm^{-3} were obtained which is in keeping with results published in the literature. The interferometer and data processing methodology was thus observed to be working as expected.

A useful dataset on the behaviour of the electron density was obtained for single plasma plumes in vacuum environments for a range of laser energies and for a

range of target compositions. The data could be useful for future studies of laser produced plasmas including comparisons with model outputs.

The next experiment was the first study to be published using the new experimental facility. The experiment concentrated on probing single plasma plumes in vacuum using the Nomarski interferometer and comparing with those from created in a gaseous atmosphere. The target was a flat slab of 99.99% pure zinc. The gaseous atmosphere was created by introducing oxygen to the chamber to create a background pressure of 10 mbar. The choice of target and background gas was related to the fact that there is currently a large amount of research being conducted on creation of zinc oxide materials, in particular using the pulsed laser deposition method. The experiment was thus particularly interesting for that research community.

Two-dimensional spatially and temporally resolved laser interferograms were taken of the Zn plasma plume revealing the structure and evolution of the electron density profile and the differences between the two scenarios. The plumes were simultaneously utilised for pulsed laser deposition where Si substrates were used to grow the sample. Analysis of the samples grown was conducted via scanning electron microscopy (SEM) where comparisons between both the vacuum and background gas cases have been made. It was found that the electron density remained higher at larger distances from the target for the gaseous environment compared to the vacuum environment. This is related to confinement of the plume by the background gas. A shock front was also observed to be created at the plasma – gas interface that expanded outwards over time. The shockfront manifested itself as a blurring of the fringes in the interferograms.

It has been shown that this method can be used to probe the dynamics of laser plumes used for pulsed laser deposition at early stages (< 100 ns) in its lifecycle in different gaseous environments. This has been a somewhat neglected parameter

regime until recently due to the high levels of continuum emission which makes traditional plasma diagnostics based on line-ratio and line-width measurements very difficult but is of vital importance as the plasma parameters of the plume at this early stage undoubtedly determine the parameters at later times when materials deposition take place. It is also at this early stage that interaction between the plume and any background gases (in particular ionisation of and mixing with background gases) takes place as revealed by our analysis of the interferometry.

After it was observed that the expansion of a compressive layer of gas at the plasma – gas interface was visible in the interferograms, some experiments were performed on analysing the expansion of the compressive layers of gas for a variety of laser energies and background gas pressures. The standard method for analysing such layers has been shadowgraphy and so, as a comparison, shadowgraphy was also performed along with interferometry.

It was found that the compressive layer was visible in both shadowgraphy and interferometery for high background gas pressures (≈ 100 – 1000 mbar) and the spatio-temporal analysis of the layer using both techniques gave similar results. The velocity of the expansion of the compressive gas layer was relatively low at these pressures (≤ 10 km s^{-1}). When the pressure of the background gas was lowered, however, in the region of 1 – 100 mbar, it was observed that the compressive gas layer was not detectable using shadowgraphy. In fact interferometry was the only technique utilised that was capable of detecting the compressive layer in these regimes. The expansion of the compressive layer here had a much higher velocity (up to 100 km s^{-1}) and manifested itself as a blurring of the fringes in the interferogram. This blurring of the fringes was visible in the bare interferograms but needed close inspection. The application of a find edges algorithm revealed the presence of the compressive gas layer much more clearly. It was shown that interferometry can be used to diagnose the

interaction of laser produced plasmas in gaseous environments in pressure regimes where other techniques such as shadowgraphy are not sensitive.

References

[1] A. Sagisaka, H. Daido, K. Ogura, S. Orimo, Y. Hayashi, M. Nishiuchi, M. Mori, K. Matsukado, A. Fukumi, Z. Li, S. Nakamura, K. Takagaki, H. Hazama, M. Suzuki, T. Utsumi, S. V. Bulanov and T. Esirkepov, Characterization of preformed plasmas with an interferometer for ultra-short high-intensity laser-plasma interactions, *Applied Physics B – Laser and Optics*, **78**, 919-922, (2004).

[2] L. A. Doyle, G. W. Martin, A. Al-Khateeb, Electron number density measurements in magnesium laser produced plumes. *Applied Surface Science*, **129**, 716-720, (1998).

[3] M. Purvis, J. Grava, J. Filevich, Dynamics of converging laser-created plasmas in semicylindrical cavities studied using soft x-ray laser interferometry. *Physical Review E – Statistical, Nonlinear and Soft Matter Physics*, **76**, 4, (2007).

[4] F. Veloso, H. Chuaqui, R. Aliaga-Rossel, Laser-produced annular plasmas. *Review of Scientific Instruments*, **77**, 6, (2006).

[5] J. F. Ready, Effects of High-Power Laser Radiation, Academic Press, New York, (1971).

[6] P. Hough, C. McLoughlin, T. J. Kelly, S. S. Harilal, J. P. Mosnier, J. T. Costello, Time resolved Nomarski interferometry of laser produced plasma plumes, *Applied Surface Science*, **255**, 10, 5167-5171 (2009).

[7] Z.G. Zhang, F. Zhou, X.Q. Wei, M. Liu, G. Sun, C.S. Chen, C.S. Xue, H.Z. Zhuang, B.Y. Man, Effects of Oxygen Pressures on Pulsed Laser Deposition of ZnO films, *Physica E – Low Dimensional Systems and Nanostructures*, **39**, 253-257, (2007).

[8] X. S. Gao, J. M. Xue, J. Lib, C. K. Ong, J. Wang, Ferroelectric $Pb(Mg_{1/3}Nb_{2/3})O_3$ Thin Films by PLD at Varying Oxygen Pressures, *Microelectronic Engineering*, **66**, 926–932, (2003).

[9] D Rajesh, K. Adhikary and S. Ray, Comparison of Electrical, Optical, and Structural Properties of RF-Sputtered ZnO Thin Films Deposited Under Different Gas Ambients, *Japanese Journal of Applied Physics*, **47**, 3, 1501-1506, (2008).

[10] T.-W. Kin, T. Kawazoea, S. Yamazakib, J. Limb, T. Yatsuia and M. Ohtsua, Room Temperature Ultraviolet Emission from ZnO Nanocrystallites Fabricated by the Low Temperature Oxidation of Metallic Zn Precursors, *Solid State Communications*, **127**, 21-24. (2003).

[11] F. Li, D.-I. Son, J.-H. Leem, T. W. Kim, W. Dong and Y.-H. Kim, Enhanced Ultraviolet Emission from ZnO Nanocrystals Embedded in a Hybrid Polymer Composite Layer, *Journal of Applied Physics*, **103**, 073511, (2008).

[12] P.-K. Shin, Y. Aya, T. Ikegami, K. Ebihara Application of Pulsed Laser Deposited Zinc Oxide Films to Thin Film Transistor Device, *Thin Solid Films*, **516**, 3767-3771, (2008).

[13] K. Ghule, A. V. Ghule, B.-J. Chen and Y.-C. Ling, Preparation and Characterization of ZnO Nanoparticles Coated Paper and its Antibacterial Activity Study, *Green Chemistry*, **8**, 1034-1041, (2006).

[14] Ü. Özgür, Ya. I. Alivov, C. Liu, A. Teke, M. A. Reshchikov, S. Doğan, V. Avrutin, S.-J. Cho, and H. Morkoç, A Comprehensive Review of ZnO Materials and Devices, *Journal of Applied Physics*, **98**, 041301, (2005).

[15] T. Okada , J. Suehiro, Synthesis of Nano-structured Materials by Laser-Ablation and their Application to Sensors, *Applied Surface Science*, **253**, 7840–7847, (2007).

[16] R. O'Haire, E. McGlynn, M. O. Henry, J. P. Mosnier, ZnO Nanostructured Thin Films Grown by Pulsed Laser Deposition in Mixed O2/Ar Background gas, *Superlattices and Microstructures*, **42**, 468-472, (2007).

[17] R. O'Haire, A. Meaney, E. McGlynn, M. O. Henry, J.-R. Duclère, J. P. Mosnier, Growth of crystalline ZnO nanostructures using pulsed laser deposition, *Superlattices and Microstructures*, **39**, 153-161, (2006).

[18] M. I. K. Santala, M. Zepf, I. Watts, F. N. Beg, E. Clark, M. Tatarakis, K. Krushelnick, and A. E. Dangor, T. McCanny, I. Spencer, R. P. Singhal, and K.W. D. Ledingham, S. C. Wilks, A. C. Machacek and J. S. Wark, R. Allott, R. J. Clarke, and P. A. Norreys, Effect of the Plasma Density Scale Length on the Direction of Fast Electrons in Relativistic Laser-Solid Interactions, *Physical Review Letters*, **84**, 7, (2000).

[19] S. Amoruso, J. Schou, J. G. Lunney, Multiple-Scattering Effects in Laser Ablation Plume Propagation in Gases, *Europhysics Letters*, **76**, 3, 436-442, (2006).

[20] C.L. Liu, J. N. Leboeuf, R.F. Wood, D. B. Geobegan, J. M. Donato, K. R. Chen, A. A. Puretzky, Computational Modeling of Physical Processes During Laser Ablation, *Materials Science and Engineering*, **B47**, 70-77, (1997).

[21] J. N. Leboeuf, K. R. Chen, J. M. Donato, D. B. Geohegan, C. L. Liu, A. A. Puretzky, R. F. Wood, Modeling of Plume Dynamics in Laser Ablation Processes for Thin Film Deposition of Materials, *Physics of Plasmas*, **3**, 5, 2203-2209 (1996).

[22] J. Gonzalo, F. Vega, C. N. Alfonso, Plasma expansion dynamics in reactive and inert atmospheres during laser ablation of Bi(2)Sr(2)Ca(1)Cu(2)O(7-y), *Journal of Applied Physics*, **77**, 12, 6588-6593 (1995).

[23] R. K. Singh, A. Kumar, B. G. Patel, K. P. Subramanian, Role of Ambient Gas and Laser Fluence in Governing the dynamics of the Plasma Plumes Produced by

Laser Blow Off of LiF-C Thin Film, *Journal of Applied Physics*, **101**,103301, (2007).

[24] S. S. Harilal, C. V. Bindhu, M. S. Tillack, F. Najmabadi, A. C. Gaeris, Plume Splitting and Sharpening in Laser Produced Aluminium Plasma, *Journal of Physics D: Applied Physics*, **35**, 2935-2938 (2002).

[25] C. V. Budtz-Jorgensen, M. M. Mond, B. Doggett, J. G. Lunney, Model for Laser Ablation Plume Expansion in Gas, *Journal of Physics D: Applied Physics*, **38**, 12, (2005).

[26] J.-F. Y. Gravel and D. Boudreau, Study by Focused Shadowgraphy of the Effect of Laser Irradiance on Laser-Induced Plasma Formation and Ablation Rate in Various Gases, *Spectrochimica Acta Part B*, **64**, 56–66, (2009).

[27] M. Thiyagarajan and J. Scharer, Experimental Investigation of Ultraviolet Laser Induced Plasma Density and Temperature Evolution in Air, *Journal of Applied Physics*, **104**, 013303, (2008).

[28] ImageJ: http://rsbweb.nih.gov/ij/

Chapter 4:

Laser and Optical Diagnostics of Colliding Laser Produced Plasmas

In this chapter, the results from laser (*i.e.* interferometry) and optical (*i.e.* fast imaging and optical emission spectroscopy) diagnostics of colliding plasmas are presented. The results from spatially, temporally and spectrally resolved fast imaging are presented and spatially and temporally resolved laser interferometry are a major focus of this chapter. These techniques complement each other extremely well, revealing information about the atoms, ions (imaging) and electrons (interferometry).

The results from optical emission spectroscopy are also presented revealing detailed information about the neutral atom and ion structure and composition of the stagnation layer. The chapter concludes with a presentation of results from angularly, temporally, spatially and spectrally resolved fast imaging which reveals more detailed information on the distribution of atoms and ions around the stagnation layer.

4.1: Fast Imaging

The experimental details for production and fast imaging of colliding laser produced plasmas are as described in Section 2.5. The results presented here in sections 4.1 – 4.3 are based on results from our first major study of colliding plasmas using the new experimental facility [1]. Fast imaging provided a means to track the 2-dimensional spatial evolution of the laser produced plasmas with very high temporal and spatial resolution. The flexible optical imaging system (based on a simple zoom

lens) provided variable magnification (1X - 4X) and concomitant control over spatial resolution versus field of view. The minimum shutter width of the intensifier was 3 ns and so the tracking of the spatial evolution of the plasma with very high temporal resolution was also possible. Finally, with the aid of narrow bandpass filters, it was possible filter out emission from a particular neutral atom or ion and track their evolution independently.

Figure 4.1 shows a sequence of optical images taken at different time delays following the instant at which the peak of the laser pulse creating the two seeds plasmas impinges on a flat aluminium slab target (the location of the target surface is depicted on each image as a white bar). The seed plasma plumes were created by dividing a 1064 nm wavelength, 600 mJ, 6 ns (FWHM) laser pulse into two parts with the aid of a 0.5° wedge prism and focusing it onto two spots, each of 100μm diameter, by means of a f/6 plano-convex lens located at 45° to the target normal. The peak irradiance at each spot was $\approx 1 \times 10^{11}$ Wcm^{-2}. The seed plasmas had a separation of 1.3 mm and the target was a flat slab of 99.9% pure aluminium which was mounted on a high precision in-vacuum motorized X–Z stage so that the target could be moved to reveal a new surface after each shot. The pressure in the interaction chamber was maintained at better than 1×10^{-5} mbar.

The camera, an intensified charged coupled device (or ICCD), comprised a gated intensifier coupled to a front illuminated (CCD) camera via a high quality relay lens system. As discussed in Section 2.5.1, it was supplied by Andor Technology Ltd. (Model No. DH5H7) and had 512×512 pixels with a pixel area of 24 μm × 24 μm yielding an active area of 12.3 × 12.3 mm^2. Using a telephoto lens system, the camera was able to capture a field of view (FOV) of ≈ 3.8 × 3.8 mm^2. The magnification was measured by placing a graduated target at the plasma position which resulted in a value of 3.2X. The ICCD was synchronized with a Surelite III laser using a Stanford DG 535 delay-gate generator with a total trigger jitter of less than 1 ns which was verified using a fast

sampling digital oscilloscope. For all experiments the time delay is defined to be the time interval following the peak of the seed plasma producing laser pulse.

An optical filter centred at 460 nm with a bandwidth of 10 nm (described in Section 2.5) was placed in front of the ICCD to isolate emission from the Al^+ ions in the seed plasmas and stagnation layer. This spectral range is free from emission due to atomic aluminium and also multiply charged ions which may be present in the seed plasmas and stagnation layer. The optical gate width for each image was 3 ns and a stagnation layer first appeared in these images at a time delay of 20 ns after the emission of first light from the seed plasmas which we take to be the instant of creation.

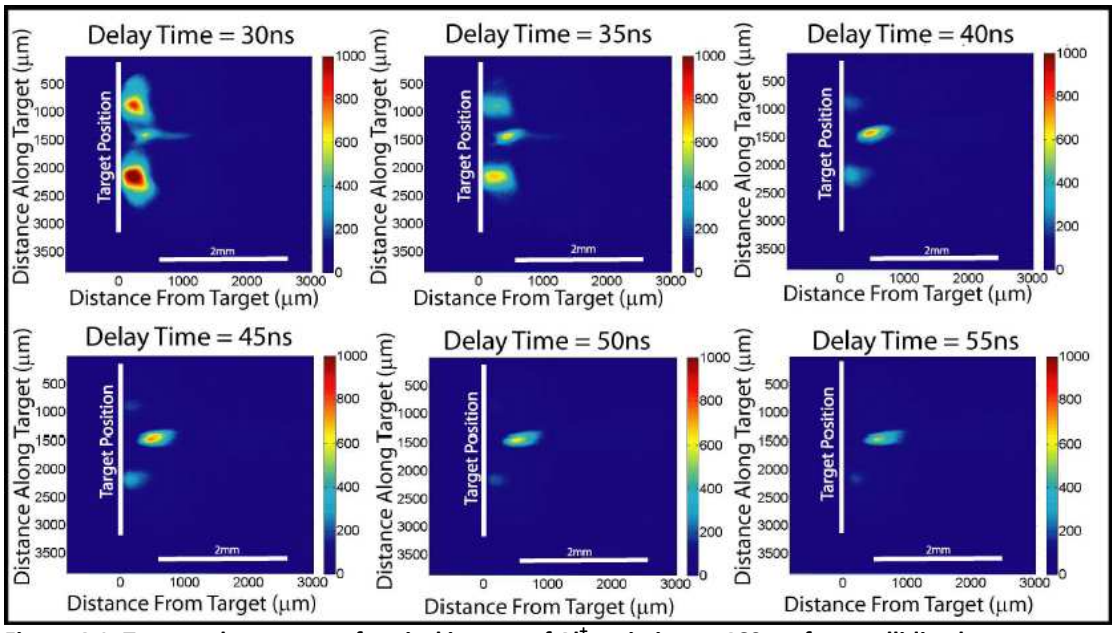

Figure 4.1: Temporal sequence of optical images of Al^+ emission at 460nm from colliding laser produced plasmas. Each image has a field of view or FOV of 3.84mm X 3.84mm.

The stagnation layer grows outwards in time as plasma species (here singly charged ions) from the seed plasmas meet at time delays determined by their time of flight from each source point. So the layer appears first in the space directly between the two seed plasmas as that corresponds to the shortest ion time of flight and

subsequently grows outwards from the target surface,. At stagnation, the ion kinetic energy is converted into excitation energy and the stagnation layer begins to glow, the intensity growing with time into a bright strip of light. It is clear that the excitation energy has to be high as the upper and lower levels of the selected transition at 466 nm lie almost 18 eV and 15 eV respectively above the ground state. The expansion of the Al^+ ions over time has also been measured along trajectories normal, at 45° and parallel to the flat target surface in order to extract the range of ion velocities in the expanding seed plasmas. The trajectories are drawn in figure 4.2(a) for the image recorded some 30 ns after the peak of the laser pulse. The plume expansion in all three directions is shown in figure 4.2(b).

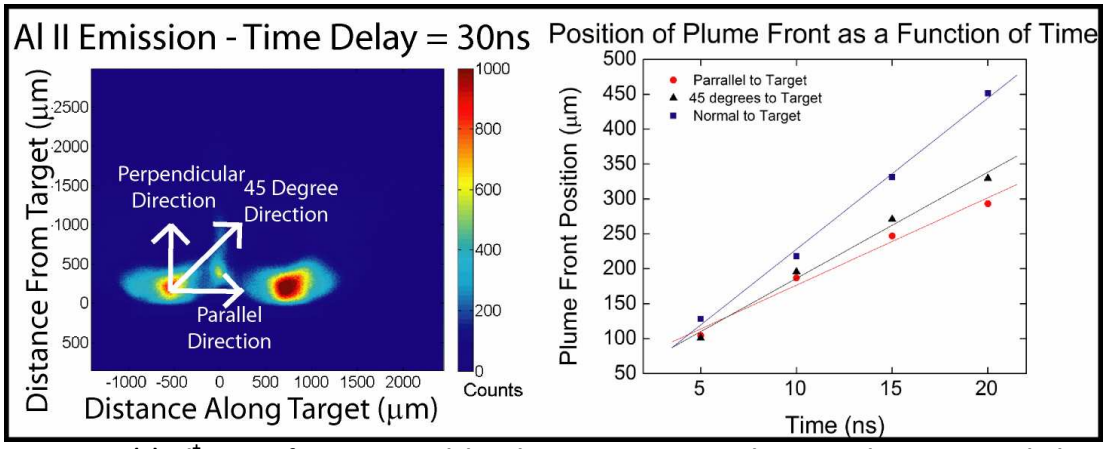

Figure 4.2: (a) Al^+ image for one time delay showing trajectories chosen to determine seed plume expansion velocities. (b) Plume expansion traces for trajectories normal, parallel and at 45° to the target surface.

The values obtained were 2.17 ± 0.1 x 10^6 $cm.s^{-1}$, 1.53 ± 0.12 x 10^6 $cm.s^{-1}$ and 1.22 ± 0.12 x 10^6 $cm.s^{-1}$ respectively. These values represent the bulk motion of Al^+ ions in the seed plasmas. The fastest ions reach the collision front quite quickly and their velocity can be estimated by noting that the stagnation layer starts to form and heat up just 20 ns after the seed plasmas are created. As the ions travel an average distance (to the centre of the layer) of ca. 1 mm, this group of ions has a peak velocity of 4.0 x 10^6 $cm.s^{-1}$.

4.2: Laser Interferometry

One of the main objectives of the entire project was to probe colliding laser produced plasmas at very early times with the intention of observing the nascent phase of the stagnation layer. For this reason, Nomarski laser interferometry was one of the main plasma diagnostic tools employed as it permitted us to probe the spatio-temporal behaviour of the electron density in the stagnation layer at very early times with high spatial resolution.

The first experiment aimed to probe the structure of the free electrons distribution at the mid-plane, i.e. in the region of the stagnation layer. All experimental conditions were kept exactly the same as those for the fast imaging results presented in Section 4.1. For laser interferometry, as described in chapter 2, the two lasers and the (CMOS) camera (C Cam Ltd, Model: BCi4) were synchronized using two Stanford DG535 delay generators which resulted in a maximum temporal jitter of 1 ns. This value was verified during the experiment using fast photodiodes (Thorlabs model no.: DET10A) and a fast sampling digital oscilloscope (TDS3032, 300 MHz, 2.5 GS/s). A TTL master pulse was sent to trigger the Surelite III laser (6 ns, 1064 nm) to create the seed plasmas. The delay to firing the probe laser (Surelite I, 4 ns, 532 nm) was scanned to interrogate the stagnation layer at different times before, during and after its formation. The camera was triggered synchronously with the probe laser beam and the shutter was left open for 1 μs during which time it captured the 4 ns duration interferogram. In performing the analysis of the interferograms we have assumed that the plasma is distributed uniformly around an axis normal to the target. This assumption is justified having performed fast photography in the broadband regime at angles of 0°, 45° and 90° (*cf.* section 4.5, figure 4.12) to the axis normal to the target surface. The results show the broadband plasma emission to be symmetric to a high degree about this axis and one would not expect the free electron distribution to depart significantly from this.

In figure 4.3 a series of stagnation layer interferograms and corresponding 2D electron density maps is shown for six time delays ranging from 20 to 80 ns. The density scales on each image are chosen to best illustrate the general features of each frame. Comparisons on an absolute scale are made later (Section 4.3). The error associated with the electron density was determined by finding the minimum detectable fringe shift and extracting its corresponding electron density. A value of $\pm 0.22 \times 10^{19}$ cm^{-3} has been obtained for the minimum detectable fringe shift.

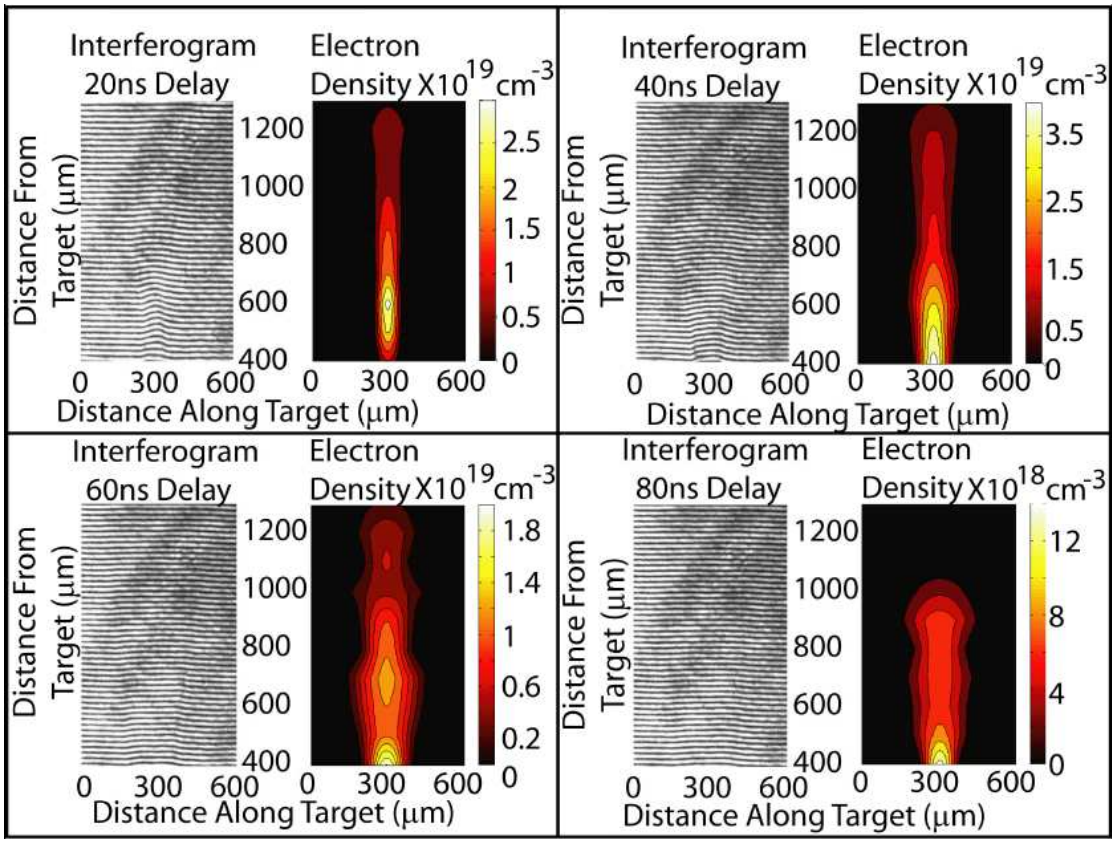

Figure 4.3: Sequence of interferograms showing the temporal and spatial evolution of the electron density in the stagnation layer created at the interface between two colliding laser produced plasma plumes.

What is immediately clear from the image sequence is that the electrons form tightly confined structures reminiscent of ion stagnation layers at the collision front between the two seed plasma plumes and are observed to first form at a time delay of 10 ns. At 20 ns the fringe shift pattern and corresponding electron density distribution

are quite confined but also reasonably uniform. One can see that the fringe pattern is pinched close to the target at a position where it is sandwiched directly between the two seed plasmas. The electron density is greatest at a distance of approximately 0.4 mm from the target surface where it reaches a peak value in excess of $4 \pm 0.22 \times 10^{19}$ cm^{-3} at a time delay of 40 ns (*cf.* figure 4.4, page 117). The electron density begins to fall from that point onwards, so that by 80 ns its peak value has dropped significantly and the distribution has flattened somewhat.

In figure 4.4 the temporal evolution of the electron density profile at a distance of 0.4 mm from the target surface is plotted for delay times ranging from 10 to 80 ns after the peak of the seed plasma laser.

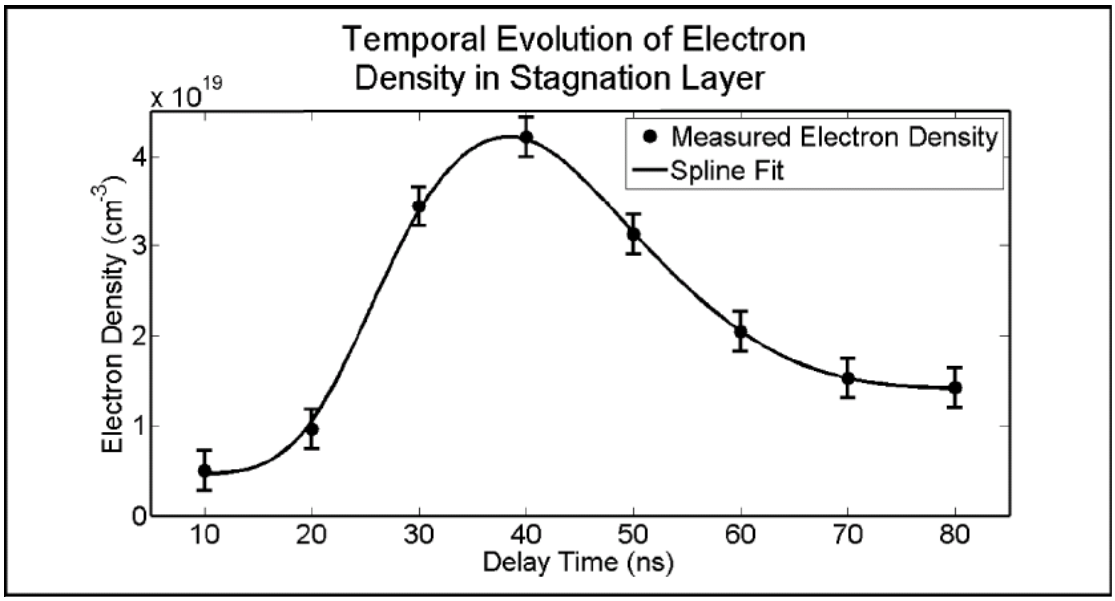

Figure 4.4: Time evolution of the stagnation layer electron density at a distance of 0.4 mm from the target surface.

The first detectable fringe shift occurs at a delay of 10 ns following the creation of the seed plasmas. As time proceeds, a soft electron stagnation (e.g. 10 ns frame) followed by rapid further stagnation, which peaks at 40 ns or so, is observed. After that point the electron layer becomes broad and damped. As noted above, by 80 ns the

peak electron density has dropped to a value in the low 10^{19} cm^{-3} range and soon after drops further to a density below the minimum detectable value of the interferometer.

4.3: Comparisons: Fast Imaging and Interferometry

The results from the spectrally resolved fast imaging in Section 4.1 reveals the spatio-temporal behavior of the singly charged ions in the region of the stagnation layer. Broadband fast imaging has also been performed and reveals the spatio-temporal behavior of the plasma as a whole in the region of the stagnation layer. The results from the laser interferometry in Section 4.2 reveal the spatio-temporal behavior of free electrons in the region of the stagnation layer. It is therefore instructive to make a direct comparison of the ion spatial distribution with the whole plasma spatial distribution and with the free electron distribution. This is done in figure 4.5 where a 2-D space-time montage of electron density, Al^+ ionic and broadband optical emission distributions is presented. The density (upper row) and intensity (lower rows) scales are the same for each panel to aid direct comparison.

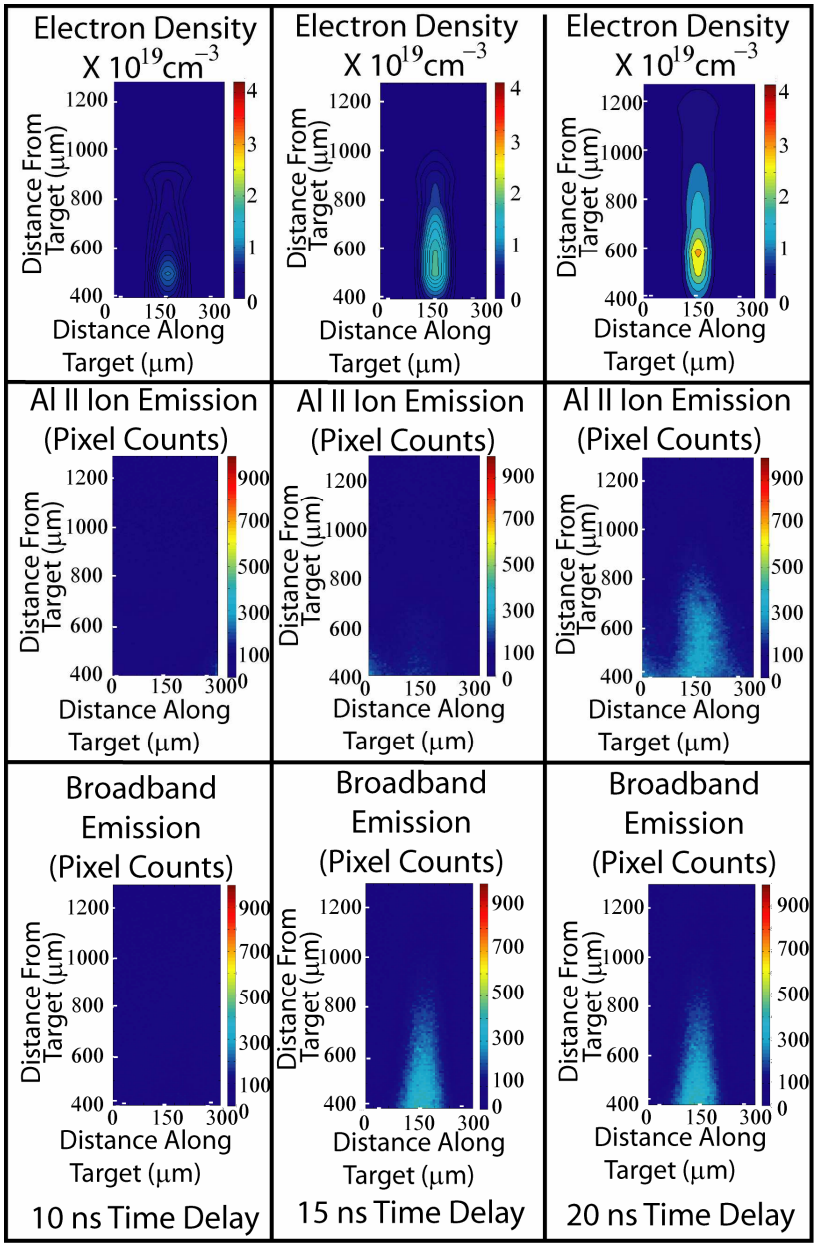

Figure 4.5: 2D temporally and spatially resolved electron density and ion distribution maps. The top panels show the 2D electron density profile in the stagnation region between the two seed plasmas for time delays of 10, 15 and 20 ns. The centre panels show the Al^+ ion emission in the corresponding region at the same time delays while the bottom panels show the corresponding broadband emission.

Looking at the free electron maps, one can see a broad, long and weakly stagnating layer in the electron density distribution at 10 ns resulting from a fringe shift induced by electron localization and stagnation at this time delay. The broadband images display evidence of nascent plasma stagnation at a time delay of 15 ns. The

singly charged ions are observed to stagnate in the vicinity of the collision front at 20 ns which is approximately 10 ns after that of the electrons and 5 ns after the first signs of broadband plasma emission from the collision front. The broadband images contain emission from a range of ion stages and so will be characteristic of the plasma as a whole. The observations in figure 4.5 are attributed to the separation of charge in space in the seed plasma plumes. Immediately after the seed plasmas are formed, the fast electrons try to move towards the mid-plane leaving behind the heavier ions, thus creating a space charge potential (otherwise know as an ambipolar potential and associated field). This field induces an acceleration on each ion depending on its charge. For this reason more highly charged ions will acquire a higher velocity at early times.

Images were also taken of the neutral atom species and the results are shown in figure 4.6. They are in keeping with the observations above where first evidence of stagnation of the neutral species occurs at a time delay of 30 ns and so are the slowest moving species (as one would expect).

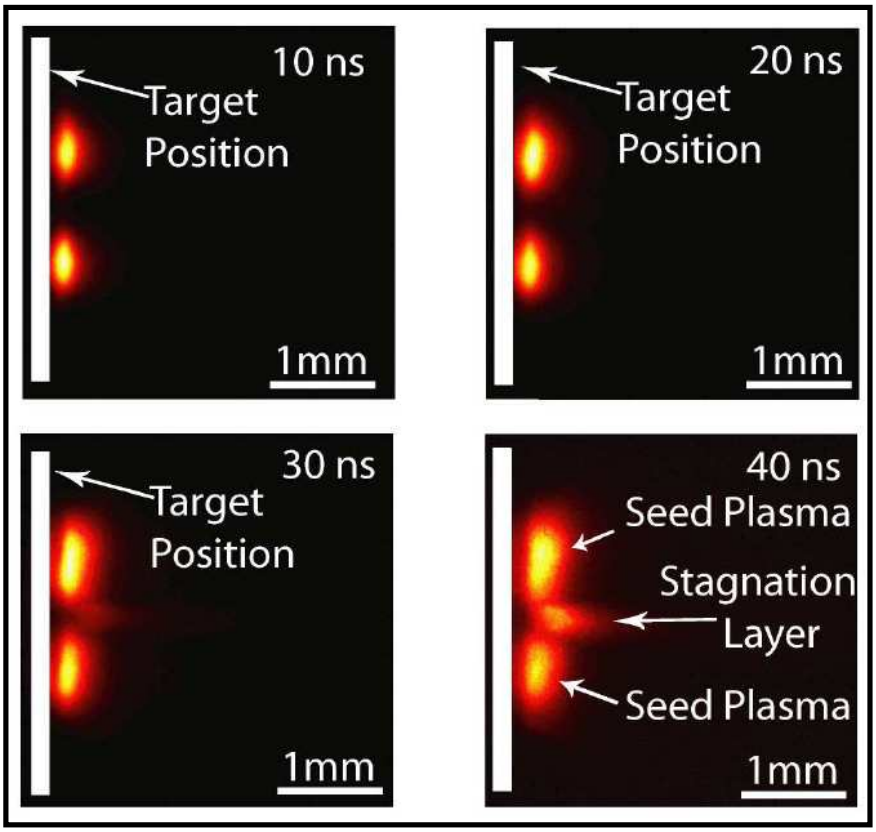

Figure 4.6: Comparison of the results of fast imaging at time delays of 10, 20, 30 and 40 ns for neutral atom species revealing first evidence of their stagnation at a time delay of 30 ns.

Fast electron generation and transport has been studied for intense and ultra-intense laser interactions (10^{15} – $>10^{20}$ W cm^{-2}) with solids and dense plasmas [2]. There is also, however, evidence of the separation of charge in space occurring in expanding plasma plumes (single seed plumes) produced by 'longer' laser pulses (> 100 ps). For example, Okano *et al.* [3] infer space charge separation to explain the results of a time resolved electron shadowgraphy measurements on an expanding copper plasma plume. They found that a fast electron bunch leads the expansion of the laser produced plasma. Ursu *et al.* [4] have shown how the expansion velocities of the ionised species in single laser produced plasmas (for plasmas very similar to those presented in this thesis) are found to increase with the degree of ionisation. Not unexpectedly then, they found that excited neutral species were the slowest moving particles [4]. In their experiment they also employed an ICCD camera coupled to an

optical spectrometer to identify and track over time, line emission for neutral, singly and doubly charged ions emitted from a single laser produced aluminium plasma. They concluded that the electrons are first species leave the target after laser excitation. Subsequently, ions are ejected on a very short time scale through interaction with the very intense electric field formed by initial electron laser excitation and detachment. In the experiment presented here (Section 4.1 – 4.3), by allowing a pair of plasma plumes to collide and using both 'ion and electron imaging', this separation is shown optically.

Returning to figure 4.5 above, as the electron front leads the ion front one expects stagnation of the electrons to occur before ion stagnation and indeed the stagnation of more highly charged ions before that of lowly charged ions. Of course any electron – ion separation is mediated by the ambipolar field which will limit it to a dimension less than the Debye length [5], λ_D, which will be on average ≈ 100 μm for the seed plasmas in these experiments. λ_D for the stagnated plasma can be expected to change in space and time as it evolves but this variation will be significantly smaller than in the case of an expanding laser plasma plumes. The time delay of 10 ns between electron and singly charged ion stagnation is consistent with the transit time obtained by dividing the Debye length by the average ion velocity obtained from figure 4.2. The time delay of 5 ns between electron stagnation and broader plasma stagnation is also well within the limits set by the Deybe length. It can be further speculated that the early stagnation of the electrons at the mid-plane collision front induces a significant 'screening' effect which permits the ions (especially more highly charged ions) to approach each other quite closely leading to a tight ion stagnation layer, especially at 40 ns where the electron density reaches quite a high value (≈ 4.5 ± 0.22 × 10^{19} cm^{-3}).

4.4: Optical Emission Spectroscopy

Optical emission spectroscopy has been employed to observe the spatial distribution of neutral atomic, singly and doubly charged aluminum in the stagnation

layer [6] with the same experimental conditions that pertained when creating the colliding laser produced plasmas in Section 4.1. In summary, the laser energy was kept constant at 600 mJ and focused to two spots separated by 1.3 mm. The pressure in the vacuum chamber was maintained at a pressure of better than 1×10^{-5} mbar.

The optical system used to perform the OES studies has been fully described in Section 2.5.2. Briefly an Intensified Charged Coupled Device (ICCD, Andor Technology, Model No. DH534, 1024 × 1024 pixels with pixel size of $13 \times 13\ \mu m^2$) was employed to perform the spatially and temporally resolved optical emission spectroscopy measurements. The camera was mounted on a Chromex 0.5 m optical 1:1 imaging spectrometer with a 1200 l/mm grating resulting in a relative wavelength measurement accuracy of +/-0.1 nm. The plasma was imaged onto the slit of the spectrograph using achromatic imaging lenses with a magnification of 2X. The stagnation layer was orientated to lie along the spectrometer slit as previously illustrated in figure 2.22. The spectrometer was used to analyse line emission from neutral, singly and doubly charged aluminium. The slit width was set to a width of 60 μm and all spectra were averaged over 10 laser shots. The gate width for each shot was set to 5 ns.

The spectral studies, presented here indicate that the emission features within the stagnation layer comprise (mainly) excited neutrals along with singly and doubly charged ions. Corresponding spectra are shown in figure 4.7 where line emission for neutral, singly and doubly charged aluminium are compared as a function of distance from the target for two different delay times (80 and 150 ns). The birth of the stagnation layer occurs at a time delay of 10 – 30 ns or so depending on experimental parameters and it usually dissipates into the surrounding environment at a time delay of ≈ 200 ns. Thus observing the stagnation layer at a time delay of 80 ns and 150 ns reveals the structure of the layer at relatively early and late times respectively.

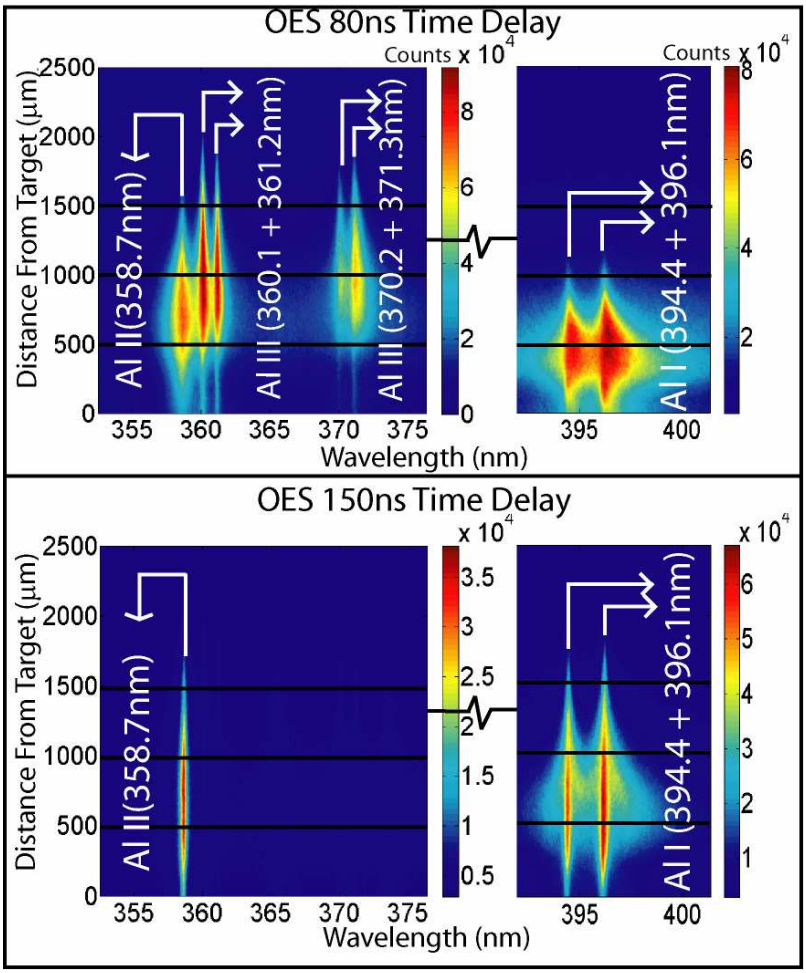

Figure 4.7: Comparison of the optical spectra obtained showing line emission from neutral, singly and doubly charged aluminium as a function of distance from the target at two different delay times (80 and 150 ns). The black lines serve to illustrate distances of 0.5, 1 and 1.5 mm from the target surface.

Spectra in the region of 365 nm capture line emission from both singly charged and doubly charged ions. The line at 358.7 nm is a 4f $^3F_3$-3d $^3D_3$ transition in singly charged aluminium. The other lines present in the spectra originate from transitions in doubly charged ions at 360.19 nm ($2p^6 3d\ ^2D_{3/2} - 2p^6 4p\ ^2P_{3/2}$), 361.23 nm ($2p^6 3d\ ^3D_{3/2} - 2p^6 4p\ ^2P_{1/2}$), 370.2 nm ($2p^6 4p\ ^2P_{1/2} - 2p^6 5s\ ^2S_{1/2}$) and 371.31 nm ($2p^6 4p\ ^2P_{3/2} - 2p^6 5s\ ^2S_{1/2}$) [7]. This wavelength region is well suited to the task of making a comparison of the spatial distributions of singly and doubly charged ions. From figure 4.7 it is clear that at a delay time of 80 ns (top panel), the spatial extent of singly charged ion emission is limited to a region extending outwards to a distance of ca. 1.5 mm from the target surface with a maximum value ca. 0.7 mm from the target surface. The doubly

charged ions can be seen at larger distances (up to 2 mm) from the target with an emission distribution which peaks at a distance of 1 mm.

The emission from neutral aluminium comprises transitions at 394.4 nm ($3s^2 4s\ ^2S_{1/2} - 3s^2 3p\ ^2P_{1/2}$) and 396.15 nm ($3s^2 4s\ ^2S_{1/2} - 3s^2 3p\ ^2P_{3/2}$) [7]. At 80 ns, again looking along the direction normal to the target surface, the neutral atom distribution is found to be less extended than either the singly or doubly charged ions. In fact neutral species reach a maximum distance of only ≈ 1 mm from the target with the peak emission originating from a region lying at a distance of ≈ 0.5 mm from the target.

Figure 4.8 shows a comparison of the spatial distribution of the line emission from Al^0 (396.15 nm), Al^+ (358.65 nm) and Al^{2+} (360.19 nm) at a delay time of 80 ns and clearly highlights the spatial dispersion of plasma species along the stagnation layer.

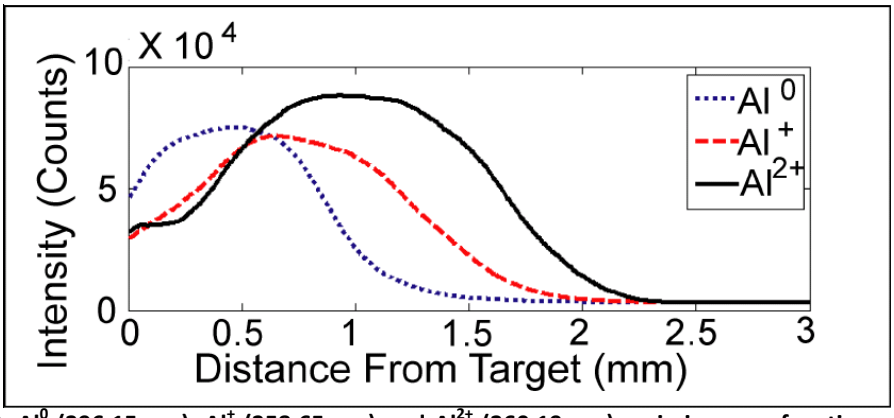

Figure 4.8: Al^0 (396.15 nm), Al^+ (358.65 nm) and Al^{2+} (360.19 nm) emission as a function of distance from the target at a time delay of 80 ns providing evidence of the space charge effects where the doubly ionised aluminium extends to the furthest distances from the target followed by singly ionised aluminium with the neutral species remaining close to the target.

As already mentioned, Ursa et al. [4] have shown that the expansion velocities of ionised species in single laser produced plasmas are found to increase with their degree of ionisation. It was already shown in this study (*cf.* Section 4.1 - 4.3 [1]) that the separation of charge in space can become manifest at very early times (<20 ns) in plasma – plasma collisions just prior to and during stagnation. In the present

spectroscopic experiment, however, one can observe that the development of the stagnation layer at later times (≈ 80 ns – compared to the very early times studied at the start of this chaper) is still influenced by the mechanisms of expansion in the seed plasmas resulting in variations in the spatial distribution of ions of different charge in the stagnation layer. This is clear in figure 4.7 and figure 4.8 where specifically the emission from doubly charged ions is evident at the furthest distances from the target as the more highly charged ions expand away from the seed plasmas with a larger velocity than either singly charged or neutral atomic species. Similarly emission in the stagnation layer from singly charged ions predominates at greater distances from the target than the excited neutral species.

At later times (150 ns - Figure 4.7 - bottom panel) most of the emission originates from neutral atoms and singly charged ions suggesting that the doubly charged ion density has been significantly reduced via processes such as recombination at this stage. The Al atoms and Al^+ ions are observed to emit from very similar regions (at later times) implying that the stagnation layer has developed into a more uniform plasma with neutral atom and ion species more uniformly distributed.

Figure 4.9 shows the stagnation layer luminous front expansion trace (distance vs. time) of neutral, singly and doubly charged aluminium emission obtained from optical emission spectroscopy. The selected emission lines were 396.15 nm, 358.65 nm and 360.19 nm for Al^0, Al^+ and Al^{2+} respectively. The luminous front is defined to be the position of the plasma front where the emission is measured to be 10% of the peak value. An important point for one to bear in mind is that this trace is indicative of the *spatial development* (normal to the target – *cf.* figure 2.22) of various species in the stagnation layer. Ions leaving the seed plasmas travelling on different trajectories will reach the stagnation layer at a variety of positions and times. Hence inferring an 'expansion velocity' for any one species expanding outward in the stagnation layer or indeed the stagnation layer as a whole would be somewhat misleading.

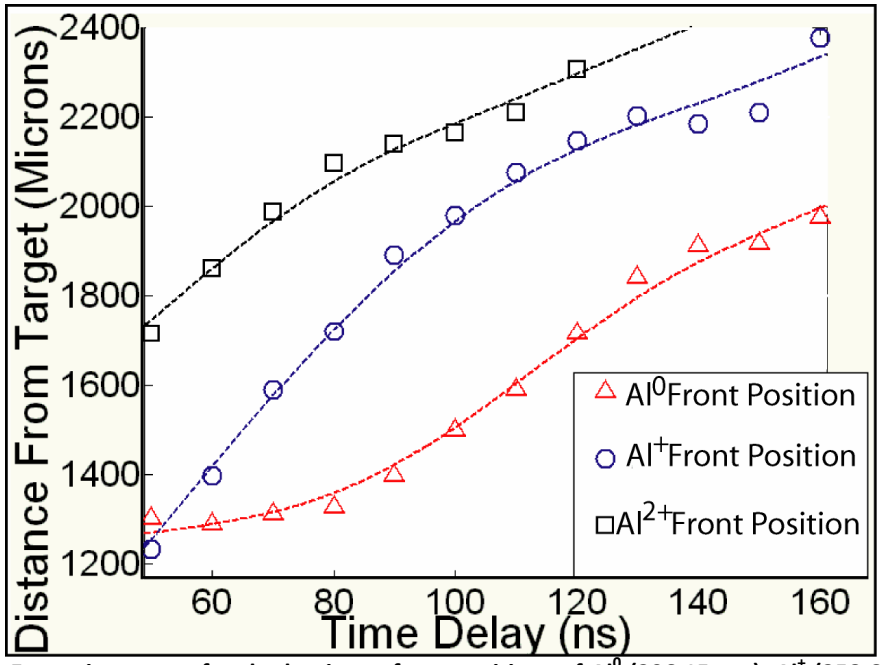

Figure 4.9: Expansion traces for the luminous front positions of Al^0 (396.15 nm), Al^+ (358.65 nm) and Al^{2+} (360.19 nm) emphasising the differences in the spatial evolution of the three ion stages. The smooth curves are best fitted spline curves.

It can be clearly seen from figure 4.9 that the temporal evolution of the emission front for the neutrals and the two ion stages differ substantially. The emission front for doubly charged Al extends furthest from the target surface. Similarly the emission front of singly charged aluminium extends farther from the target than that for neutral aluminium. To complement these spectroscopy studies, angle and spectrally resolved ICCD imaging has been performed; results are shown in the following section.

4.5: Angle Resolved Fast Imaging

2D spatial emission features of the stagnation region have been investigated using ICCD fast imaging at two orthogonal camera angles [6]. The angles of view were defined previously in figure 2.20 and are again defined below in figure 4.10 for easy

recollection. As before in the previous fast imaging experiments, two narrow bandpass filters were employed to select line emission from neutral and singly charged aluminium.

Images of colliding plasmas were obtained at two orthogonal camera angles, namely 0 degrees and 90 degrees. The 0° angle of view is the standard viewing angle for studying colliding laser produced plasmas [8, 9] but this method is limited in that it only captures emission in the lateral expansion plane, defined to be the plane that cuts through the seed plasmas and the stagnation layer. This is illustrated in figure 4.10 below.

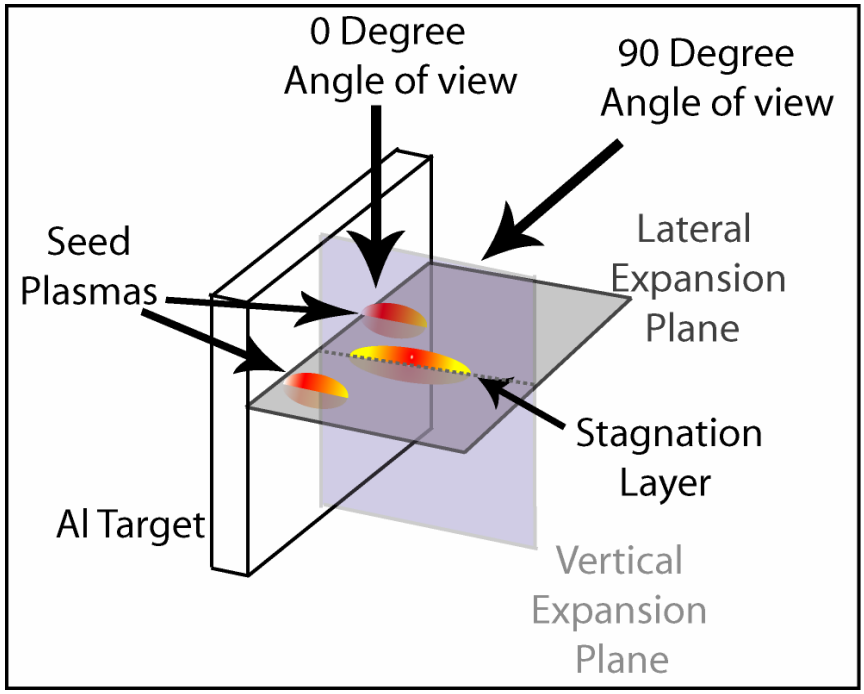

Figure 4.10: Diagram illustrating the orientation of the colliding plasmas with respect to the lateral and vertical expansion planes of the colliding plasmas. Also defined are the two orthogonal angles of view which were used for the angle resolved fast imaging experiments, i.e., 0° and 90°.

Viewing the stagnation layer from the 90° angle of view reveals the structure of neutral atoms, singly charged ions and whole plasma broadband emission from the stagnation layer in the vertical expansion plane. It is worth noting that it was necessary to record images at time delays when the majority of the radiation emanated from the

stagnation layer alone in order to ensure that emission from the seed plumes did not overlay emission from the stagnation layer.

The first results of this fast imaging study are presented in figure 4.11 where emission from the stagnation layer for the 2 orthogonal angle of views are compared for Al^0, Al^+ and broadband emission. The time delay for each image was 90 ns, by which time emission from the seed plasmas had faded and so they did not obstruct the view of the ICCD from the stagnation layer. Also included are the normalised lineouts (parallel to the target) to compare the spatial distributions of the atoms, ions and broadband emission at a distance of 1 mm from the target for the two different viewing angles. The white lines in the images serve to illustrate the locations where the lineouts were taken.

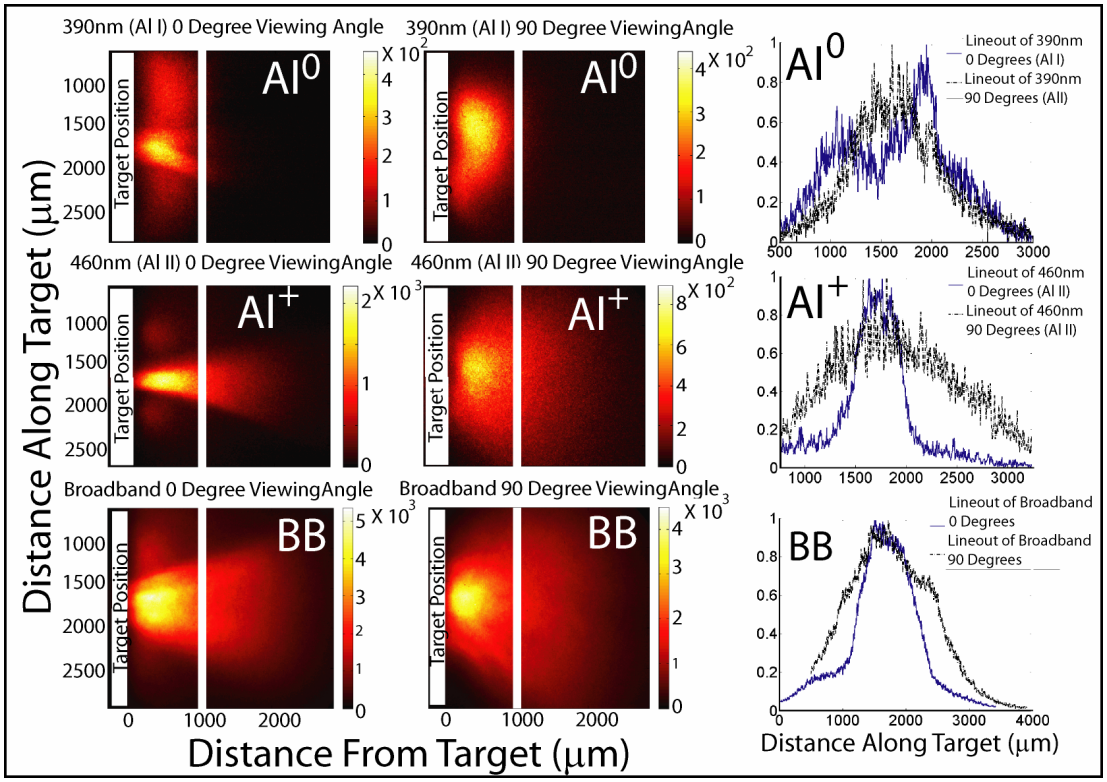

Figure 4.11: Comparison of the angle resolved spatial emission from neutral Al atoms with that of singly charged Al ions and broadband emission for the two viewing angles (0 degrees – left panel and 90 degrees – centre panel) defined in figure 1b (recorded at a time delay of 90 ns). The right hand panel shows the comparison of the emission distribution (lineouts) from the two viewing angles along a line parallel to, but separated from, the target surface by a distance of 1 mm. The white lines in the images define the positions where the lineouts were taken for comparison.

The most prominent feature in figure 4.11 is the asymmetry of the emission from Al^+ in the stagnation layer when viewed from the two orthogonal directions. The singly charged ions form a narrow elongated layer at the interface between the two seed plasmas. Pressure from the two seed plasmas, in the lateral expansion plane (0° angle of view), pinches the stagnation layer at early time delays (<80 ns) when plasma expansion from the seed plasmas is very strong. It therefore serves to enhance Al^+ expansion in the orthogonal direction (along the vertical expansion axis observed from the 90° angle of view). This is further illustrated by the corresponding lineouts (right panel) for the Al^+ emission in figure 4.10.

The broadband emission, characteristic of the relevant range of ion stages emitting in the 300 – 950 nm spectral window indicate the overall stagnation layer to be quite cylindrically symmetric about an axis normal from the target. To further emphasise this point, broadband images taken at a time delay of 80 ns have been compared for viewing angles of 0°, 45° and 90°. These are shown in figure 4.12 a), b) and c) respectively.

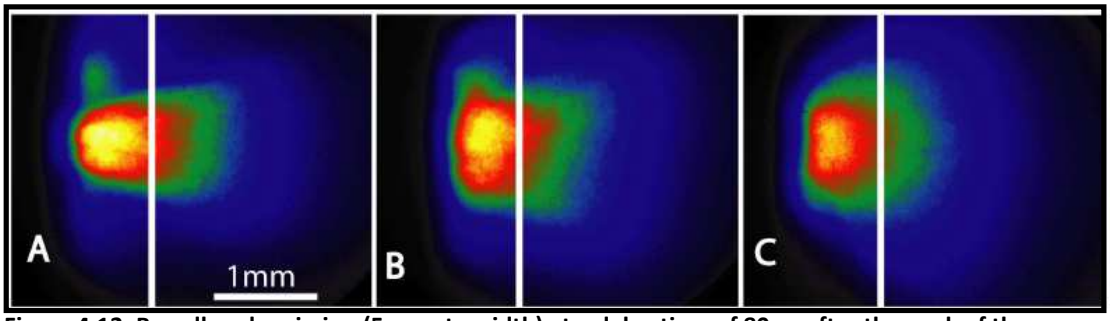

Figure 4.12: Broadband emission (5 ns gate width) at a delay time of 80 ns after the peak of the pump laser beam for an angle of view of a) 0°, b) 45° and c) 90°. The white lines indicate the position at which lineouts were taken for comparison (shown in figure 4.13 below).

To compare the results in more detail 1-D lineouts of each image at a distance of 0.8 mm from the target surface have been extracted and compared. These lineouts are indicated by the white lines in figure 4.12 and corresponding traces are compared below in figure 4.13.

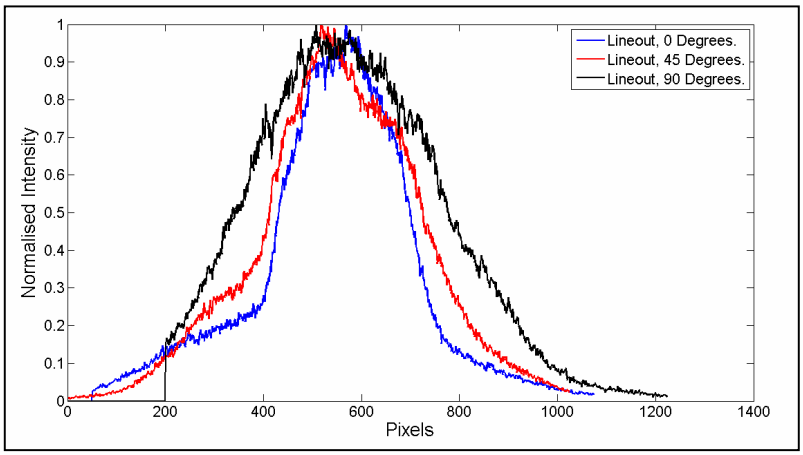

Figure: 4.13: Comparison of normalised intensity lineouts for broadband images at a distance of 0.8 mm from the target surface for angles of view of 0°, 45°, and 90°.

It can be seen from figure 4.13 that the whole plasma emission from the stagnation layer is reasonably cylindrically symmetric. The broadband images are signatures of the whole excited plasma distribution (emission due to all processes including electron excitation and recombination) and concomitantly one should expect that the electron spatial distribution also should not depart radically from this profile.

Returning to figure 4.11, emission from neutral atoms also displays a somewhat, symmetric profile with the lineouts from both viewing angles having similar profiles. There is, however, evidence of a "V" shaped profile in the image recorded at the zero degree viewing angle (*cf:* central dip in blue lineout in top right panel – figure 4.11). This V shaped profile is much more prominent at later times (> 100ns) as can be seen below in figure 4.14 where the emission images (all taken at 0° angle of view – the lateral expansion axis) of Al^0, Al^+ and whole plasma are given for two delay times (80 and 150 ns).

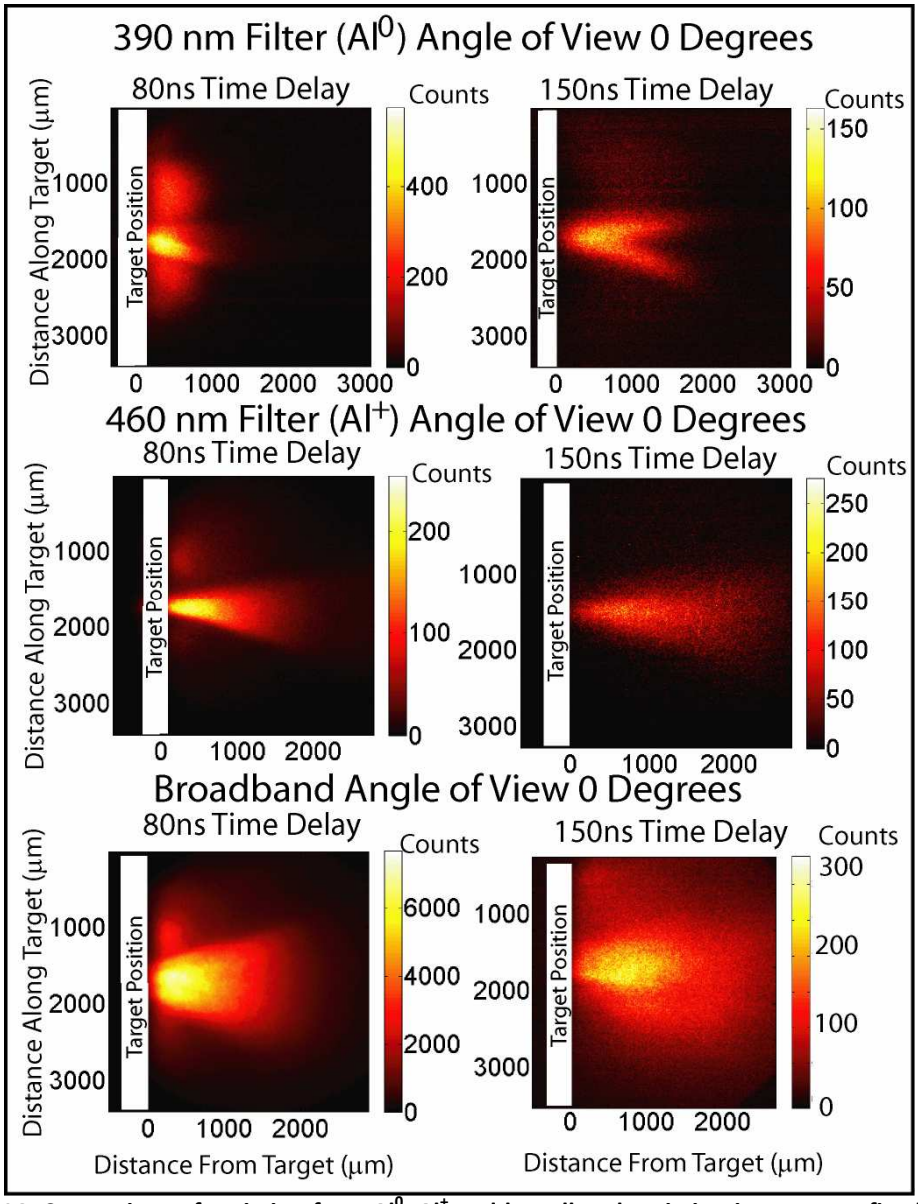

Figure 4.14: Comparison of emission from Al^0, Al^+ and broadband emission images at a fixed viewing angle (0 Degrees) and two different time delays (80 ns – left panels and 150 ns – right panels).

Similar V-shaped structures were noticed in laterally colliding plasmas previously with X-ray [10] diagnostics. In that study Farley *et al.* have observed high energy colliding plasmas (10^{15} W cm^{-2}) in the X- ray region and found that large radiative losses in the denser central region reduced its luminosity giving rise to the appearance of a V-shaped emission feature just after plasma formation (1.1 ns).

It is proposed that the bifurcation of the neutral emission in figure 4.14 can be explained as follows. The ion stagnation, as already discussed in the previous sections, precedes the arrival of the slower neutral species and hence they do not penetrate the ion stagnation layer to any great degree. Rather they collide preferentially with the outer region of the pinched layer where they emit strongly giving rise to a V-shaped neutral feature – in effect the preformed ion layer acts as a wedge preventing neutral-neutral collisions and the emission observed is due, at least in part, to neutral atom collisions with the preformed stagnation hard core.

4.6: Summary

The electron and ion distributions of the stagnation layer formed at the interface between two laterally colliding laser produced aluminium plasmas have been investigated with high temporal and spatial resolution. The plasmas were created by splitting a 6 ns, 600 mJ pulse from a Nd:YAG laser into two parts and focusing them to two spots on a flat slab of aluminum. 2D spatially and temporally resolved interferograms of the stagnation layer were obtained, from which corresponding electron density distributions were extracted. Optical imaging with an ICCD provided 2D maps of the spatial distribution of the ion emission in the stagnation layer. The electron stagnation layer is observed to have a peak electron density of 4.5×10^{19} cm^{-3} at a delay time of 40 ns with respect to the peak of the seed plasma laser pulse. Significant stagnation of the electrons is observed to occur at a probe delay time of 10 ns, while stagnation of the broader plasma occurs at a time delay of 15 ns. The Al^{+} ions are found to stagnate somewhat later at a time delay of 20 ns after the peak of the seed plasmas. First evidence of stagnation of the neutral atoms is found to occur at a time delay of 30 ns. This is attributed to the effects of space charge separation that has already been proposed in several other experiments.

The emission features of excited neutrals and ions in the stagnation layer of laterally colliding laser produced plasmas have also been investigated. Angle, spectrally and temporally resolved optical imaging and spatially and temporally resolved optical emission spectroscopy were used to diagnose the stagnation layer. Optical emission spectroscopy shows clear differences in the spatial extent of atoms with respect to that of singly and doubly charged ions. Atoms are found to remain closer to the target than ions and doubly charged ions are found to extend further from the target than singly charged ions. It also shows that the temporal and spatial development of emission fronts of Al^0, Al^+ and Al^{2+} are very different; Al^0 emission is the slowest to develop spatially and ultimately pervade the stagnation layer while Al^{2+} develops fastest revealing how space charge effects, namely the dependence of the expansion velocity of plasma species on their charge state in the seed plasmas, is a significant determining factor in the development of the stagnation layer.

Emission from neutral atoms appeared as a V shaped distribution extending from the target surface. Angle and spectrally resolved fast imaging revealed an asymmetric layer of ions in the stagnation layer. This layer is formed very early (< 80 ns) in contrast to the atoms (≈ 150 ns) at a time when the seed plasmas are still rapidly expanding, thereby causing compression of the layer. In contrast the broadband and atomic layer emission distributions are quite cylindrically symmetric about an axis normal to the target however with a dip in the atomic emission observable at the centre in the lateral expansion plane. These studies should be very useful in building up a more complete picture of the mechanisms involved in stagnation layer formation and structure for relatively low energy colliding laser plasma experiments and apposite applications, e.g., pulsed laser deposition. It should also provide a useful reference dataset for comparison with future experiments and testing future colliding plasma computer models in this parameter regime.

References

[1] P. Hough, C. McLoughlin, T. J. Kelly, P. Hayden, S. S. Harilal, J. P. Mosnier, J. T. Costello, Electron and ion stagnation at the collision front between two laser produced plasmas, *Journal of Physics D: Applied Physics*, **42**, 055211 (2009).

[2] P. McKenna, D. C. Carroll, R. J. Clarke, R. G. Evans, K. W. D. Ledingham, F. Lindau, O. Lundh, T. McCanny, D. Neely, A. P. L. Robinson, L. Robson, P. T. Simpson, C.-G. Wahlströ and M. Zepf, Lateral Electron Transport in High-Intensity Laser-Irradiated Foils Diagnosed by Ion Emission, *Physical Review Letters*, **98**, 145001 (2007)

[3] Y. Okano, Y. Hironaka, K. G. Nakamura, and K. Kondo, Time-resolved Electron Shadowgraphy for 300 ps Laser Ablation of a Copper Film, *Applied Physics Letters*, **83**, 8 (2003).

[4] C. Ursu, S. Gurlui, C. Focsa, G. Popa, Space- and Time-Tesolved Optical Diagnosis for the Study of Laser Ablation Plasma Dynamics, *Nuclear Instruments and Methods in Physics Research Section B: Beam Interactions with Materials and Atoms*, **267**, 446–450 (2009).

[5] R. J. Goldston and P. H. Rutherford, Introduction to Plasma Physics, *Institute of Physics Publishing*, (1995).

[6] P. Hough, C. McLoughlin, S. S. Harilal, J. P. Mosnier, J. T. Costello, Emission Characteristics and Dynamics of the Stagnation Layer in Colliding Laser Produced Plasmas, *Journal of Applied Physics*, Accepted December 2009.

[7] National Institute of Standards and Technology (NIST) Atomic Spectra Database, *http://physics.nist.gov/PhysRefData/ASD/lines_form.html*

[8] H. Luna, K. D. Kavangah, J. T. Costello, Study of Colliding Laser Produced Plasma by Analysis of Time- and Space-Resolved Imaging Spectra, *Journal of Applied Physics*, **101**, 033302 (2007).

[9] S. S. Harilal, C. V. Bindhu, and H.-J. Kunze, Time Evolution of Colliding Laser Produced Magnesium Plasmas Investigated using a Pinhole Camera, *Journal of Applied Physics*, **89**, 9, (2001).

[10] D. R. Farley, K. G. Estabrook, S. G. Glendinning, S. H. Glenzer, B. A. Remington, K. Shigemori, J. M. Stone, R. J. Wallace, G. B. Zimmerman and J. A. Harte, Radiative Jet Experiments of Astrophysical Interest using Intense Laser, *Physical Review Letters*, **83**, 10, (1999).

Chapter 5:

Faraday Cup Probe

The previous chapter outlined the results obtained from laser and optical diagnostics of colliding laser produced plasmas. This chapter begins by introducing the results obtained using a Faraday cup on the kinetic energy distribution of the ions emitted from a single seed plasma. A comparison is then made between the properties of the ions emitted from a single seed plume with those emitted from a pair of colliding plasmas. The final section of the chapter presents the potential applications of colliding plasmas and the promising results from some preliminary experiments performed during the project.

5.1: Faraday Cup Probe of Single Plasmas

A Faraday cup probe has been utilised to analyse the behaviour of electrons and ions from single and colliding laser produced plasmas. A lot of work has already been published on probing electron and ion emission from single laser produced plasmas using electrical probes [*e.g.* 1 - 4]. The first experiments presented here also focussed on electrons and ions emitted from single laser produced plasmas so that a comparison could be made with results in the literature. This ensured that the Faraday

cup probe was working as expected before experiments on colliding laser produced plasmas were performed.

To perform the experiments on single plasmas, the same experimental setup was used as with colliding plasmas, except that one of the laser beams used to create the seed plasmas was blocked and so was not allowed to reach the surface of the target. This meant that only one of the seed plasmas was created and so the charged particle emission from a single plasma could be easily studied. A key advantage of this procedure was that the time of flight distribution of electrons and ions from the seed plasmas could be compared with those from colliding plasmas without adjusting of the experimental arrangement.

A schematic drawing of the experimental configuration used during these experiments has already been shown in figure 2.23. Briefly, the same method to create the colliding plasmas as described in Chapter 4 was employed here resulting in two seed plasmas separated by a distance of 1.3 mm. The target material was 99.99% pure aluminium. The Faraday cup was located at a distance of 100 mm from the target and the entrance to the Faraday cup comprised of a 2 mm diameter hole resulting with an angular acceptance of 1°. For angle resolved measurements, the Faraday cup could be rotated about the plasmas with an accuracy of ± 1° as illustrated in figure 2.23. The probe was biased negatively to interrogate the ion emission and biased positively to examine the electron emission.

Figure 5.1 shows an example of the signal obtained from the Faraday cup when it is biased to collect ions (red curve) and electrons (blue curve). To create the plasma, one of the split laser beams was blocked and the other is allowed to impinge on the Al target thereby creating a single plasma. The energy of the incoming laser beam was 600 mJ. After splitting the laser beam one of the parts was blocked before reaching the

target and the other part created a single seed plasma on the alumium target. This part of the laser beam contained an energy of 300 mJ.

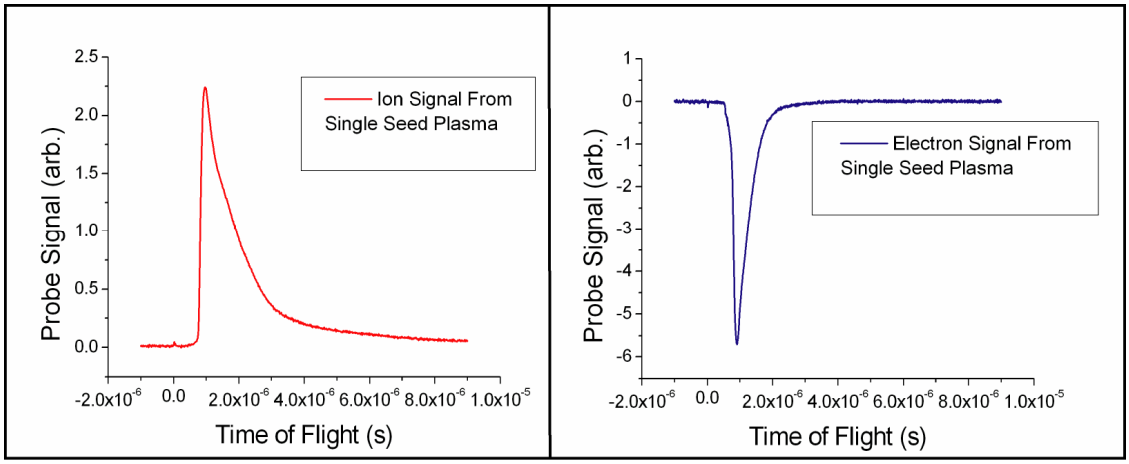

Figure 5.1: Left: Ion signal from a single laser produced plasma detected with the Faraday cup. Right: Corresponding electron signal. The plasma was created by forming a single seed plume on the target by focussing a laser beam with an energy of 300 mJ, a wavelength of 1064 nm and a pulsewidth of 6 ns on the surface of an aluminium target. A bias voltage of -30 V was used to collect the ions and +30 V to collect electrons.

The ion emission signal from a single laser produced plasma has been comprehensively investigated in the literature [e.g., 1 - 4]. As already outlined in Section 1.6.6, the Faraday cup can be utilised to record the kinetic energy distribution of the ions emitted from the plasma. The kinetic energy distribution for the ions shown in figure 5.1 is shown below in figure 5.2.

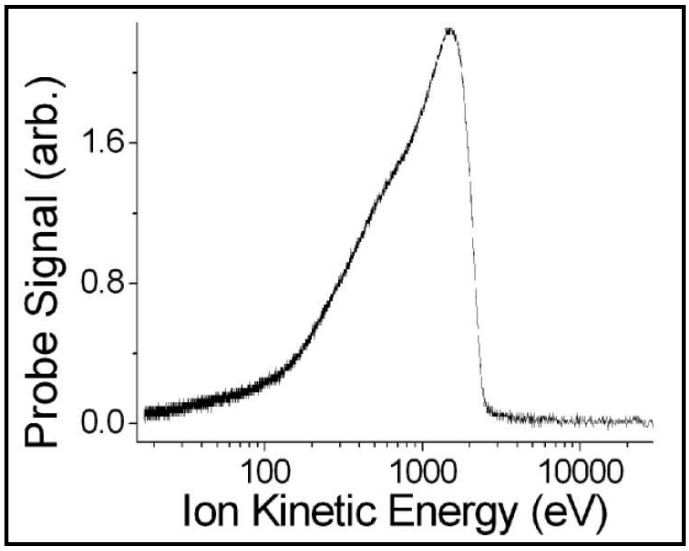

Figure 5.2: Kinetic energy distribution of the ion time of flight signal presented in figure 5.1.

The range of ion kinetic energies emitted from single laser produced plasmas is known to be very large. In the case presented here (figure 5.2), the energies range from ≈ 10 eV to 3 keV or so.

As the energy of the laser creating the plasma is varied, so too does the time of flight distribution of the ions. For example, as the laser energy is increased, more and more high energy ions (with concomitantly shorter times of flight) are observed. Also the range of kinetic energies grows as the energy of the laser is increased. This is clearly visible in figure 5.3 where the ion time of flight signal is compared for a variety of incident laser energies. It is important to note at this point that the laser energies defined in figure 5.3 are that of the energy of the full laser beam before division into two parts by the wedge prism or the so called “whole beam energy”. Thus, the energy of part of the laser beam allowed to reach the target and create an individual seed plume is half this value. Defining the laser energy with respect to the full energy at this point (and hence forth) aids direct comparison of the single plasma case with that of colliding plasmas in Section 5.3 below.

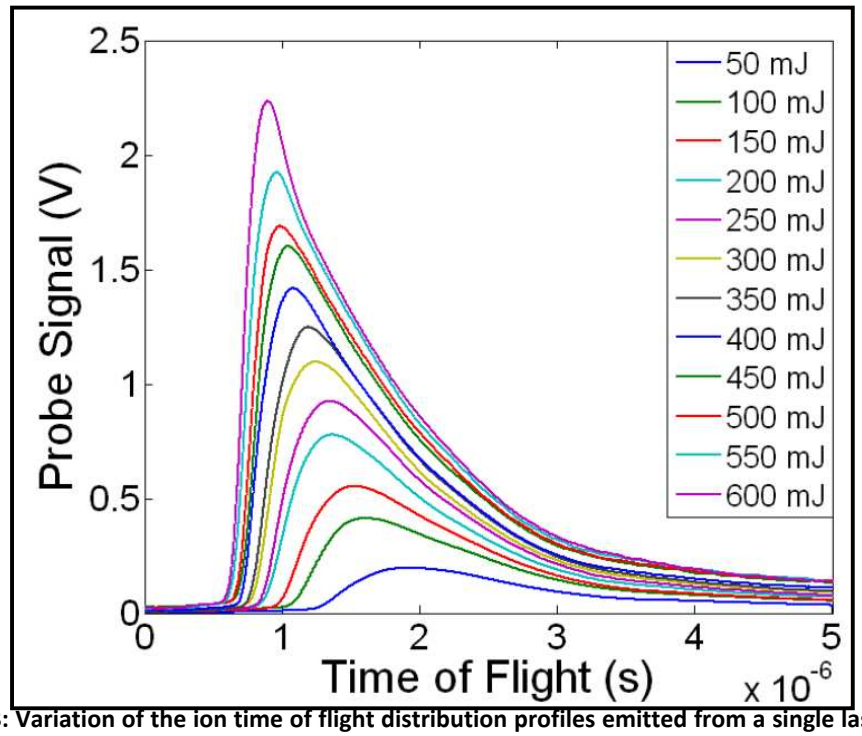

Figure 5.3: Variation of the ion time of flight distribution profiles emitted from a single laser produced plasma as a function of incident laser energy.

It can also be seen in figure 5.3 that the ion flux also grows strongly with increasing laser enegy. Integrating the ion time of flight signal, one can obtain the dependence of the ion flux as a function of laser energy and the results of this procedure are shown in figure 5.4 for each of the seed plasmas.

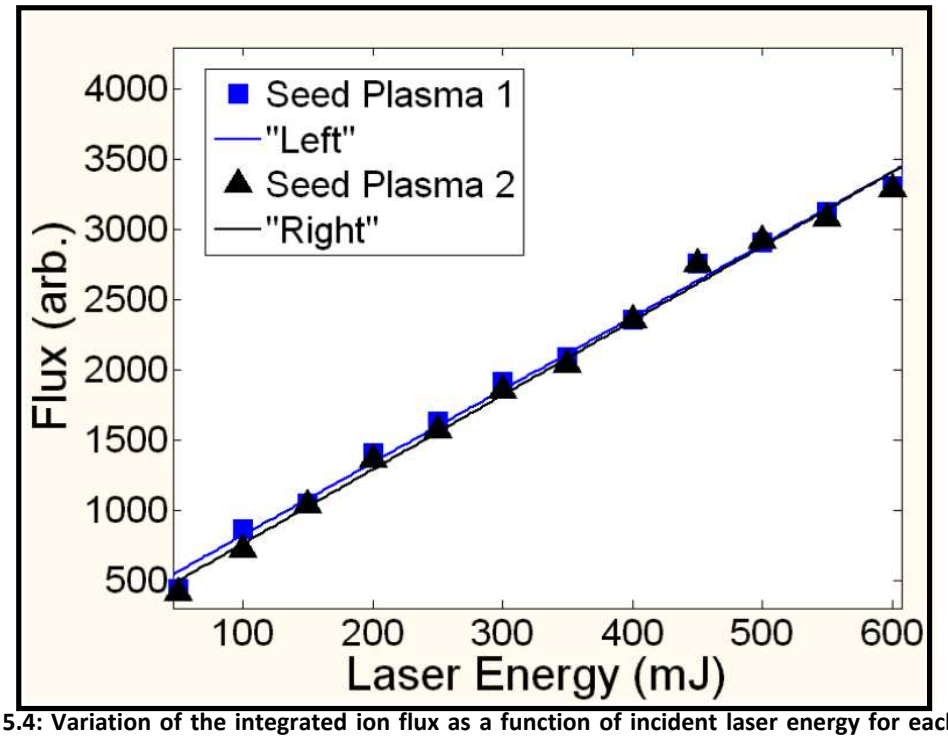

Figure 5.4: Variation of the integrated ion flux as a function of incident laser energy for each of the individual seed plasma plumes. Once again the energy of the laser is defined as the full energy before splitting at the wedge prism.

It is clear from figure 5.4 that the emitted ion flux from a single laser produced plasma increases linearly with increasing laser energy. In the case of seed plasma 1, designated as the "left plasma" here, the laser beam creating seed plasma 2, designated "right plasma" was blocked and vice versa. The results from both plasmas are in very good agreement and so the physical parameters for both of the seed plasmas appear to be very similar.

Angle resolved ion probe measurements have also been performed on a single plasma plume. In this experiment the laser beam creating the right plasma was blocked and the Faraday cup was rotated to observe the ion emission as a function of angle or angular deviation from the target normal. The results from the angle resolved measurements are presented in figure 5.5. The 0 degree angle of detection is designated to be the direction normal to the target (*cf.* figure 2.23).

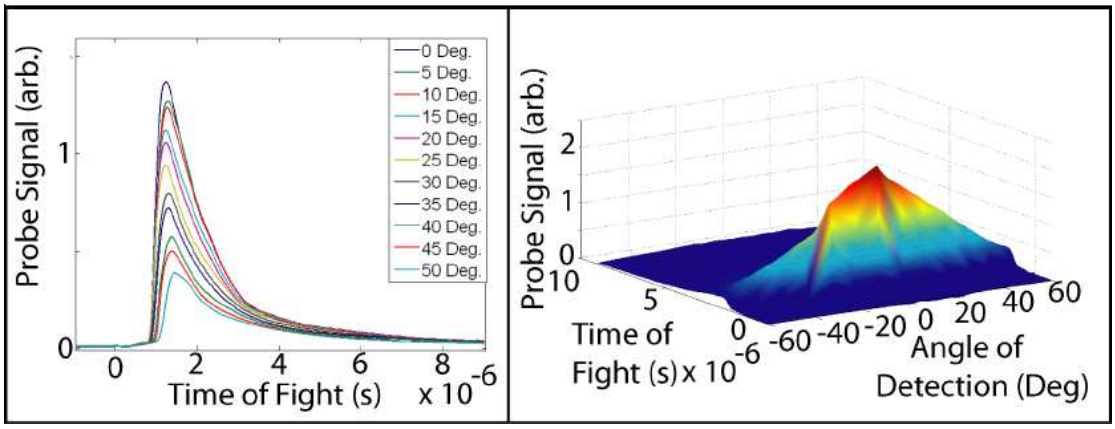

Figure 5.5: Left: Ion time of flight signal from a single Al plume as a function of angle of detection in the range 0° to 50°. Right: surface plot of the ion time of flight signal as a function of angle of detection spanning -60° to +60°. The whole energy of the laser beam was 600 mJ i.e. 300 mJ at the focal spot of a single seed plume.

As the angle of detection is increased (i.e. the Faraday cup is rotated away from the target normal) the flux of the ions reaching the detector decreases. The shape of the time of flight profile, however, remains similar for all angles. To examine this relationship in greater detail, the integrated ion flux has been extracted from the raw data and plotted as a function of viewing (or detection) angle in figure 5.6.

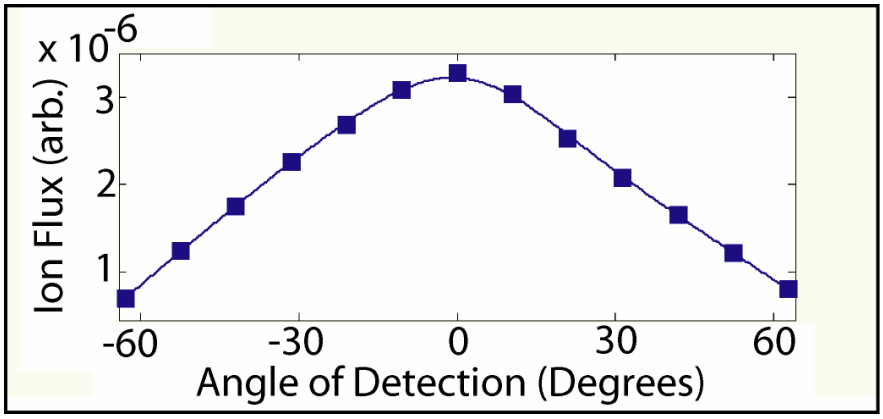

Figure 5.6: Ion flux (integrated ion time of flight signal) as a function of angle of detection of the Faraday cup. The experimental data (blue squares) have been fitted with a $\cos^2(\theta)$ curve (solid blue curve).

As can be seen from figure 5.6 a $\cos^2\theta$ function fits the angular distribution of the ion emission for a single seed plasma well. This observation has already been well

documented [5] and the results presented here on single plumes are in good agreement with many previous studies. Having ensured that the Faraday cup was working as expected, experiments on colliding plasmas were initiated.

5.2: Faraday Cup Probe of Colliding Plasmas

Performing the experiments on single plumes ensured that the Faraday cup was in proper working order so that experiments on colliding plasmas could begin. The very first experiment on colliding plasmas involved detecting the ion and electron time of flight signals from the complete colliding plasma system i.e. with both laser beams unblocked and allowed to create two seed plasmas. The target material remained a flat slab of 99.99% pure aluminium. These time of flight profiles are plotted in figure 5.7 below.

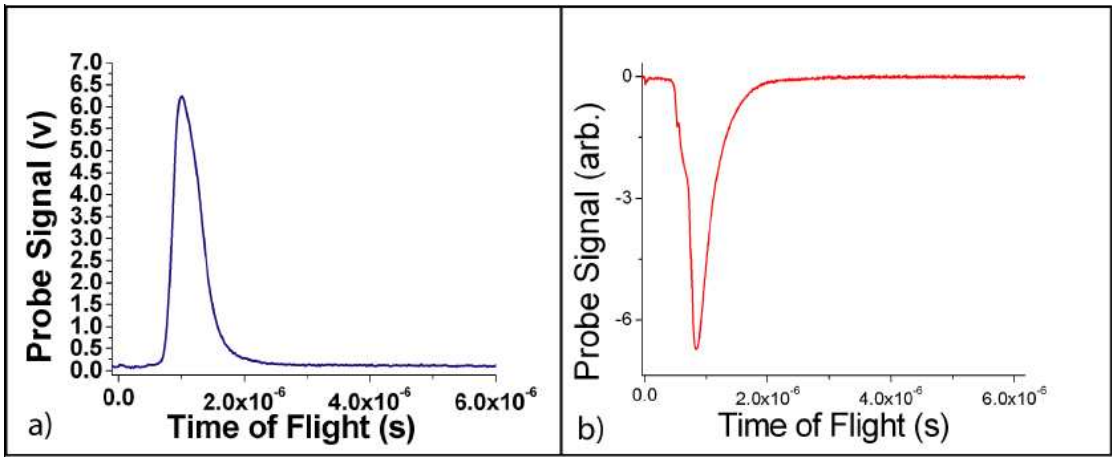

Figure 5.7: a) Ion time of flight profile for colliding plasmas at an angle of detection of 0°. b) Corresponding electron time of flight profile. The whole laser beam energy was 600 mJ i.e. 300 mJ at each of the focal spot.

From figure 5.7 (left panel), it is very clear that there is a striking difference between the ion time of flight profile from colliding plasmas compared to that from a

single plasma. Further, in depth, comparisons are made in Section 5.3 below. It is apparent from figure 5.7 a) that the time of flight profile of the ions emitted from the colliding plasma system possesses a much narrower range flight times that for a single plasma. The long tail of low energy ions (with long times of flight) that are very characteristic of the ion emission from single plasmas is absent in the colliding plasma case. On the other hand, the electron signal is not significantly different to that of a single plume. Following conversion of the ion time of flight axis to kinetic energy scale, figure 5.8 is obtained.

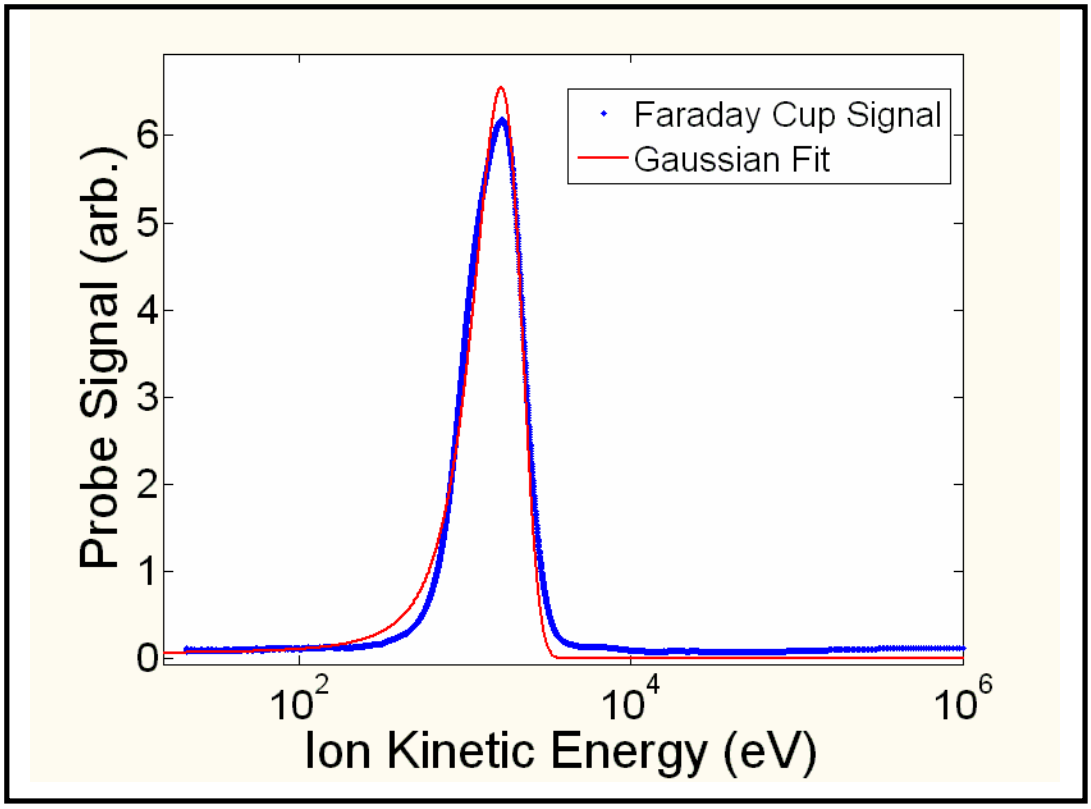

Figure 5.8: Kinetic energy distribution for ions emitted normal to the target from colliding plasmas. A Gaussian profile of the form f(x) = a*exp(-((x-b)/c)^2) fits the distribution of ion kinetic energies very well and yields an R^2 value of 0.98.

Figure 5.8 shows the ion kinetic energy distribution for the colliding plasmas system. A Gaussian profile is also fitted to the signal from the Faraday cup. The profile is very symmetric and the kinetic energies range from ≈ 500 eV to ≈ 2 keV Full Width Zero Maximum (FWZM). In fact, as visible in figure 5.8, the kinetic energy distribution

can be very well described by a Gaussian profile in complete contrast to ion emission in the case of single plasma plumes. The large flux of low energy ions present in single plumes is absent in colliding plumes.

With differences between the ion emission from single plumes and colliding plasmas visible from the very first result, it is more appropriate (and helpful to the reader), to characterise the ions emitted from colliding plasmas whilst comparing the results to single plasmas. For this reason the remainder of the results obtained from colliding plasmas is compared and contrasted with those from single plumes in Section 4.3.

5.3: Comparisons: Single and Colliding Plasmas

5.3.1: Ion Energy Distribution

The ion time of flight and kinetic energy profiles for colliding aluminium plasmas are compared to the ion profiles from the independent seed plumes, i.e. left seed plume only and right seed plume only in figure 5.9. The whole laser beam energy was 600 mJ i.e. 300 mJ in each of the pulses generating the two seed plasmas.

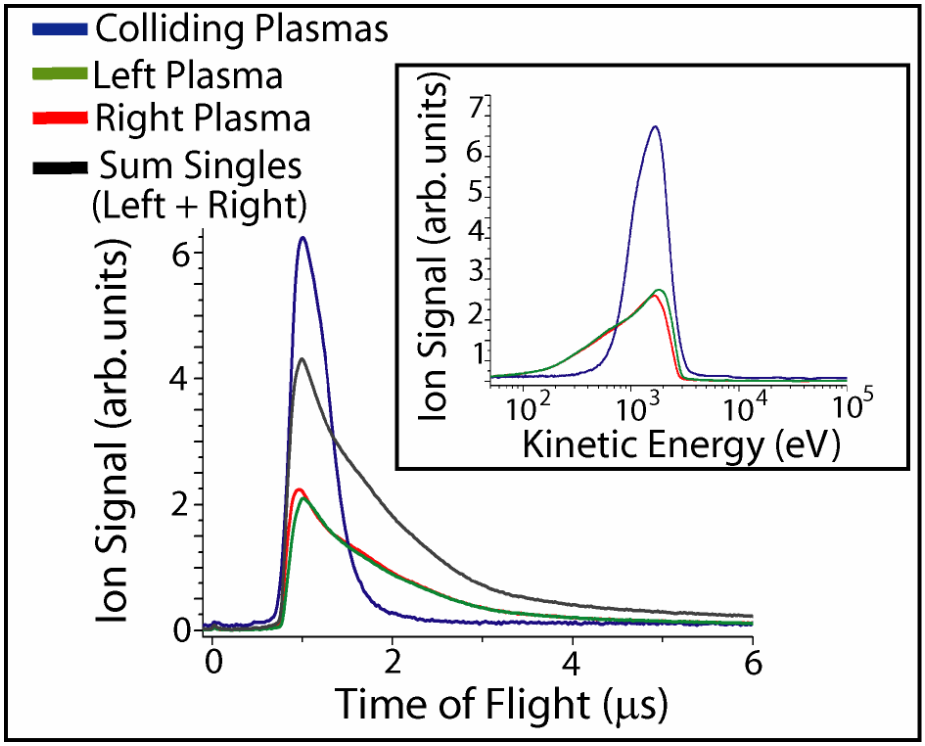

Figure 5.9: Main: Comparison of the ion time of flight profiles from the individual seed plasmas and colliding plasmas. Also shown (black curve) is the numerical sum of the signals for the seed plumes. Insert: comparison of the kinetic energy distributions for colliding plasmas and single plasmas.

As shown in figure 5.9 (main), the time of flight profile observed for colliding plasmas is found to be noticeably narrower than that from either of the seed plasmas, which have almost identical profiles. In figure 5.9 (insert) the time of flight scale is converted to kinetic energy and it shows a striking redistribution of the kinetic energy of emitted ions in the colliding plasma case compared to the individual single seed plumes. The low energy tail present in the kinetic energy distribution for the single plasma case is significantly attenuated, resulting in a narrower and more symmetric distribution. Typically the ions emitted from a single laser produced plasma possess a Maxwell-Boltzmann kinetic energy distribution [6]. The kinetic energy distribution of the seed plasmas ranges from ≈ 0.1 to 3 keV with a Full Width at Half Maximum (FWHM) of 2.6 keV with a very asymmetric distribution. The ions from the colliding plasmas exhibit a FWHM of 1.8 keV with an almost Gaussian profile.

We can also see from figure 5.10 that the (instantaneous) peak current from the colliding plasma is enhanced approximately three fold compared to that of a single plasma or by ≈ 50% compared to the numerical sum of the left and right seed plumes. The ion emission, normal to the target, from the colliding plasmas is clearly not a simple numerical sum of those from the seed plumes and we are in fact, observing an entirely new ion signal originating from the combined colliding plasma system.

5.3.2: Ion Angular Distribution

Figure 5.10 shows the angle resolved ion time of flight signal from the colliding laser plasmas system. The same experimental parameters as used to obtain figure 5.9 were employed to observe the ion angular distribution in figure 5.10.

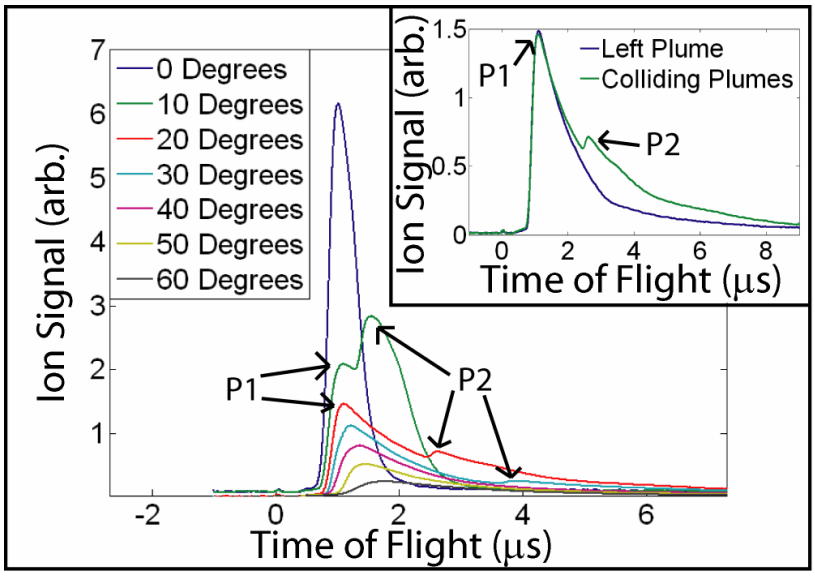

Figure 5.10: Main: Angle resolved ion time of flight signal for colliding plasmas (main). Insert: Comparison of the colliding plasma TOF signal with that of a single plume at a detector angle of 20°.

It can be readily seen from figure 5.10 that a narrower energy distribution is observed only in the direction normal to the target. The energy distribution broadens with increasing angle. It is evident from figure 5.10 that ion signal splits into two

distinct peaks, labeled P1 and P2, when the Faraday cup is moved to angles between 5° and 30° on either side of the target normal. The first peak, P1, originates from ions leaving from a seed plasma plume and arriving at the detector which appear to be largely unaffected by the presence of the stagnation layer. This is clear in figure 5.10 (inset) where it can be seen that the first peak, P1, of the colliding plasma signal matches extremely well with the ion TOF signal from the left seed plasma plume only. The signal and kinetic energy of P2 decreases rapidly as the detector is rotated away from the target normal. Beyond ± 20° P2 is severely diminished and has disappeared completely for angles greater than ± 30° where the traces are indistinguishable from the single plasma plume case. Therefore, the conclusion is that P2 is due predominantly to ion emission from the stagnation layer and/or a component of the ion emission from the seed plasmas that is significantly modified by the presence of the stagnation layer. This emission component is clearly highly directional and stands in stark contrast to emission from single plasma plumes where ions are emitted over a wide range of angles.

The exact physical mechanism or mechanisms underlying the narrowing of the kinetic energy distribution for colliding plasmas has yet to be determined. However, one can speculate as follows. In the early stages of stagnation layer formation (first few tens of nanoseconds) it is known that electrons dominate [7] the collision plane and so the prompt highly charged ions from the seed plumes are likely to experience a finite accelerative force. Hence, one would expect to observe an increase in the number of ions at higher energies close to the peak or cut-off energy. However, as time progresses, ion stagnation is established, and the stagnation layer can build up a net positive charge which can result in Coulomb blocking of the slow ions from each seed plasma thereby significantly reducing the number of low energy ions reaching the Faraday cup and consequently reducing the tail of the distribution, or almost eliminating it as can be seen in our case. Additionally, at later times when ion stagnation has established itself, one could also suffer a loss of low velocity ions in

their interaction with the stagnation layer (e.g., in neutralisation via collisional recombination processes), again leading to a suppression of the low velocity ions. All of these processes (and perhaps others) could act in consort to reduce the low energy ion flux below our detectable limits.

5.3.3: Dependence on Laser Energy

Controlling the energy of an ion beam is very important for most of the applications of ion sources. Tunability of the energy of the ions is one of the main advantages of the laser ion source and enables them to be deployed in a wide variety of applications from ion injection into accelerators to materials modification.

In figure 5.11, ion time of flight results obtained by varying the energy of the incident laser pulse are presented for colliding plasmas where they are compared to those from a single plume. Once again, the energies defined in figure 5.11 are that of the whole laser beam energy.

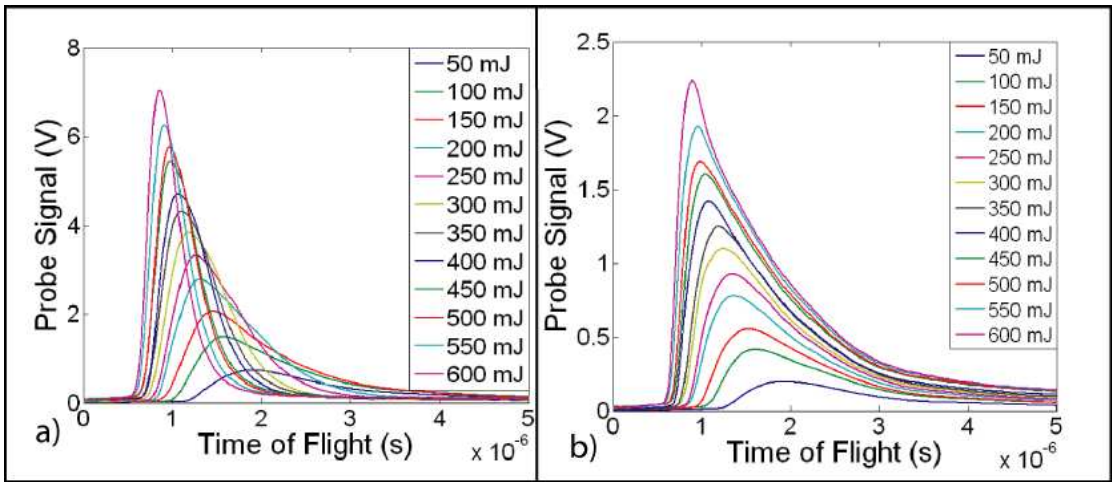

Figure 5.11: a) Ion time of flight distribution for colliding plasmas for a variety of incident laser energies. b) Ion time of flight distribution for a single plasma for a variety of incident laser energies. The scales on each axis are comparable.

It is immediately clear that there is an entirely different ion distribution behavior for colliding plasmas compared to the individual single plasmas as the energy of the laser is increased. Figure 5.11 b) is a re-plot of figure 5.3 designed to make the comparison between the two scenarios easier. Again, briefly, in the single plume case, the range of kinetic energies of the ions and the ion flux both increase with laser pulse energy. However the ions in the colliding plasmas case display a different behavior where it is clear that the range of kinetic energies increases more slowly with laser energy compared to the single plasma plume case. The peak flux of the ions emitted from the colliding plasma system is also increased significantly compared to the single plumes.

Figure 5.12 (main) shows the dependence of the peak kinetic energy and the kinetic energy FWHM of the ion beam on incident laser energy for colliding plasmas. It is clear from figure 5.12 that by varying the incident laser energy (whole laser energy), E_L, it is possible to tune the kinetic energy distribution of the ions emitted from colliding laser produced plasmas. The peak kinetic energy of the ion signal from colliding plasmas (blue diamond) increases linearly with E_L as it does for the single plume case. However, the FWHM of the kinetic energy distribution of the ions from colliding plasmas (blue squares) increases much more slowly compared to the single plume case and the FWHM scales as $E_L^{1/2}$. In contrast, in the case of a single plasma, we observe that both the peak position (red stars) and the FWHM (red circles) of the kinetic energy distribution increase linearly with E_L for these plasma regimes. Hence relatively narrower profiles (referenced to the peak position) can be obtained with increasing laser energy in the case of colliding plasma ion sources.

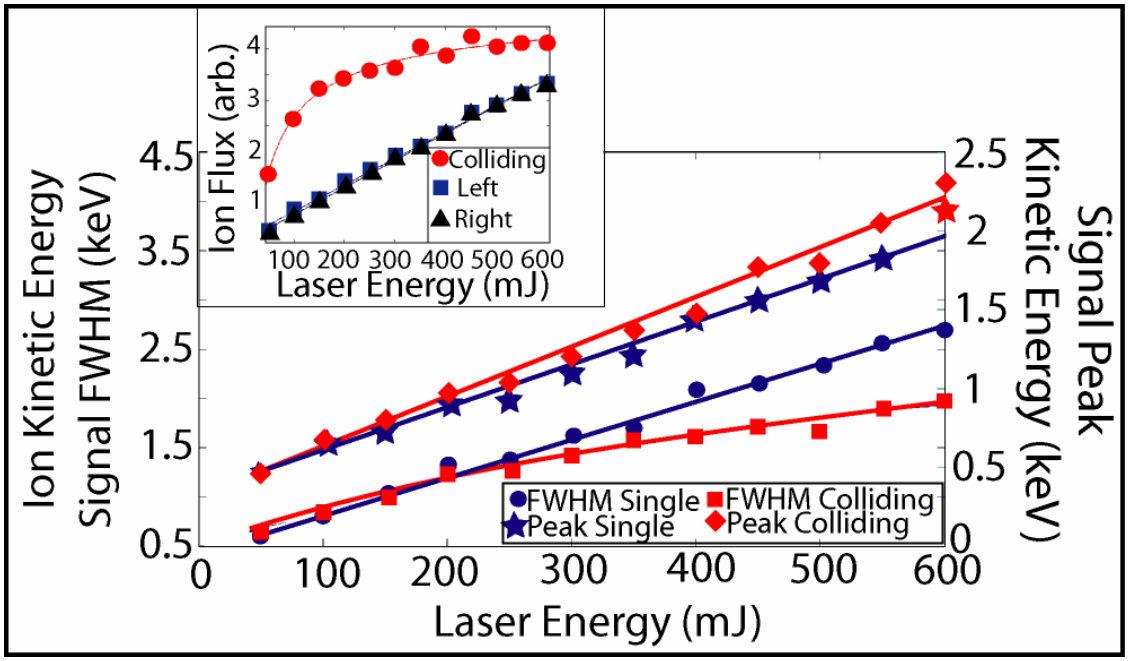

Figure 5.12: Main: Kinetic energy full width at half maximum (FWHM) and peak kinetic energy variation with incident laser energy for colliding plumes and single plasmas. Insert: Variation of integrated ion TOF signal (flux) with incident laser energy for colliding plumes.

The dependence of the integrated ion flux on the energy of the laser pulse for colliding plasmas is given in figure 5.12 (inset). The integrated ion flux from the colliding plasmas (red dots), increases rapidly at the lower laser energy scale and levels off in the case of higher laser energies and, in fact, again the integrated ion flux scales as $\alpha E_L^{1/2}$. This is in stark contrast to the case of the single plasma where the ion flux increases linearly with laser energy in these plasma regimes (blue squares and black triangles). A weak stagnation and accumulation of plasma is expected at lower laser energies and an enhancement in ion flux is noticed with increasing energy (i.e. with increasing stagnation). With increased stagnation (and increasing laser energy), one gets increased ionisation (e.g. collisional ionization) and a larger gain in ion emission (relative to single plumes) will be achieved. This is clear in figure 5.12 (insert).

Finally the integrated ion time of flight signal is plotted as a function of angle of detection between -60° and +60° in figure 5.13.

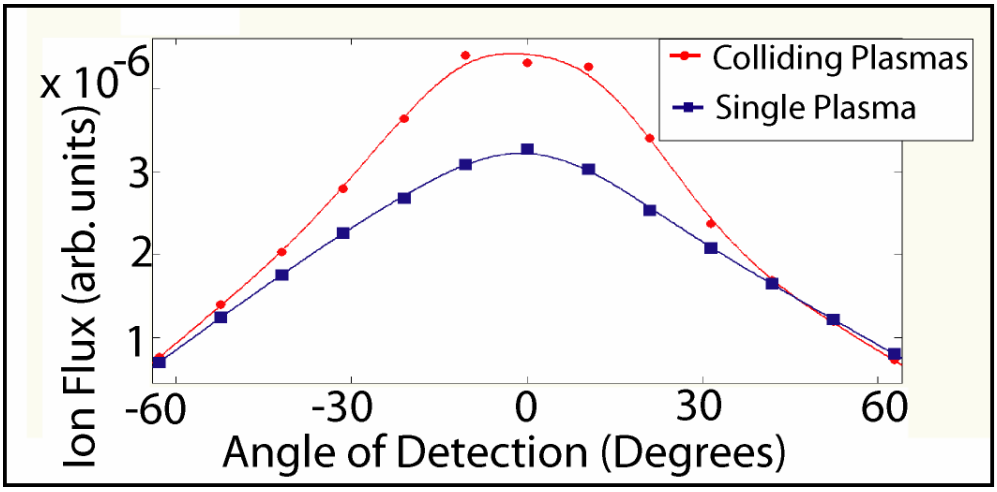

Figure 5.13: Ion flux (integrated ion time of flight signal) as a function of angle of detection of the faraday cup for a single plasma (blue) and colliding plasmas (red). The experimental data (squares) have been fitted with a $\cos^2(\theta)$ curve (solid curve) in both the single plasma and colliding plasmas case.

Figure 5.13 reveals how the ion emission from colliding plasmas differs from that of a single plasma between -30° and + 30°. Outside this angular range, the ion emission from colliding plasmas is identical to that from the seed plasma. Therefore, at angles beyond ±30° the Faraday cup only detects ions from the corresponding seed plasma on the side of the collision plane. The ion emission from the opposite seed plasma is therefore blocked by the stagnation layer as there is no evidence of ion detected from it at all. The ion emission from the stagnation layer is only detectable at angles between -30° and +30° and so it is highly directional.

5.4: Summary

Faraday cup electron and ion probe experiments were performed on single and colliding laser produced aluminum plasmas in a vacuum environment. A redistribution of kinetic energies is observed from the stagnation layer in the colliding plasmas where the lower energy ions gain kinetic energy resulting in an ion signal with a narrower range of kinetic energies compared to those from the single (seed) plume (34 %

narrower in comparison to the seed plasma at a laser energy of 600 mJ). The width (full width at half maximum) of the ion kinetic energy was found to increase linearly with increasing incident laser energy, E_L, for the single plume case whereas for colliding plasmas the width is proportional to $E_L^{1/2}$. For colliding plasmas the ion flux increases quite rapidly at the low energy laser scale before approaching saturation near the upper end of the available laser energy. The kinetic energy of the peak of the ion signal is found to increase linearly for both single and colliding plumes but is found to be on average 10% higher for colliding plasmas.

References

[1] B. Sharkov and R. Scrivens, Laser Ion Sources, *IEEE Transactions on Plasma Science*, **35**, 6, (2005).

[2] L. Láska, J. Badziak, F. P. Boody, S. Gammino, K. Jungwirth, J. Krása, E. Krousky, P. Parys, M. Pfeifer, K. Rohlena, L. Ryc, J. Skála, L. Torrisi, J. Ullschmied and J. Wolowski, Factors Influencing Parameters of Laser Ion Sources, *Laser and Particle Beams*, **25**, 199-205, (2007).

[3] M. Okamura and S. Kondrashev, Review of Laser Driven Sources for Multi-Charged Ions, *IEEE Particle Accelerator Conference*, **1-11**, 609-613, (2007).

[4] A. Misra, T. Srivastava and R. T. Thareja, Optimization of Laser Ablated Aluminium Plasmas using Charge Collector, *International Journal of Modern Physics B*, **13**, 12, 1503-1512, (1999).

[5] J. F. Ready, Effects of High Power Laser Radiation, Academic Press, New York (1971).

[6] D. Doria, A. Lorusso, F. Belloni and V. Nassisi, On the Dynamics of a Non-equilibrium Cu Plasma Produced by an Excimer Laser Interaction with a Solid, *Journal of Plasma Physics*, **72**, 2, 229-239, (2006).

[7] P. Hough, C. McLoughlin, T. J. Kelly, P. Hayden, S. S. Harilal, J. P. Mosnier, J. T. Costello, Electron and ion stagnation at the collision front between two laser produced plasmas, *Journal of Physics D: Applied Physics*, **42**, 055211 (2009).

Chapter 6: Potential Applications of Colliding Plasmas

In Chapter 5, the characteristics of ion emitted from colliding laser produced plasmas was investigated and compared and contrasted to ions emitted from single plumes.

In this chapter we outline the potential applications of colliding laser produced plasmas that were identified during the course of the project. The results of some preliminary exploratory test materials deposition experiments using colliding plasmas are also presented.

6.1: Colliding Laser Plasma Ion Source

In Chapter 5 a tunable and quasi-mono-energetic ion source was presented using laterally colliding plasma scheme. Two nanosecond laser beams were used to generate the colliding plasmas. The ions originated from the stagnation layer and possessed a narrower Gaussian-like kinetic energy profile which could be tuned by varying the input laser energy. So the colliding laser ion source provides higher flux as well narrower kinetic energy distribution compared to traditional single laser plasma ion source. There are several factors affecting the properties of the Laser Ion Source (LIS) which include laser wavelength and energy. With the colliding LIS one can gain more flexibility by considering additional changes, for example, in the target geometry.

The majority of applications of ion sources require ion beams with a narrow energy spread and in this respect, ions from colliding plasmas show much promise.

These preliminary studies present only the concept of colliding plasma LIS and its advantage over the single plasma LIS. It is hoped that these colliding plasmas can be used as the next generation of laser ion sources providing an improved, more versatile source of laser produced ions.

6.2: Materials Source

Very preliminary experiments were performed to explore the use of colliding plasmas as a source for materials deposition. In this scheme it is envisaged that the colliding plasmas could potentially replace single plumes as the source for deposition of materials for some applicatons of Pulsed Laser Deposition (PLD). These introductory experiments simply aimed to deposit ZnO onto a blank silicon substrate using a single plasma and compare the results to a colliding plasma materials source. This would elucidate the differences (if any) between deposition using colliding plasmas and a single plasma.

For the first experiment, a blank silicon substrate was placed 7 cm {which is a standard distance (i.e. several cm's) for PLD} away from a 99.99% pure ZnO target. Oxygen was injected into the chamber to create a background pressure of 1 mbar. When performing depositions using the colliding plasmas, the colliding plasmas were created using the same method as that outlined above. The laser energy was set 400 mJ (i.e. 200 mJ in each laser beams) and focused using a 30 cm focal length lens onto the surface of the target again with focal spot sizes of approximately 100 μm separated by 1.3 mm. The deposition was performed for 1000 laser pulses and the target was continuously moved to avoid laser drilling of the target. When performing deposition

of single plumes, one of the laser beams used to create the colliding plasmas was blocked and the other allowed to reach the target resulting in the creation of a single laser produced plasma. This method guaranteed that the experimental parameters (e.g. focal spot size, laser energy *etc.*) remained constant during the experiment. Depositions using a single plume were performed for 2000 laser pulses (1000 pulses from each seed plasma) to compensate for the fact that when depositing using a colliding plasma system, two plasmas are created during the 1000 laser pulses aggregated in that case. This would enable direct comparison between the two samples.

The deposited materials were viewed using Scanning Electron Microscopy (SEM) which revealed the structures deposited on the surface of the blank silicon substrates. The first results from this experiment are shown below in figure 6.1.

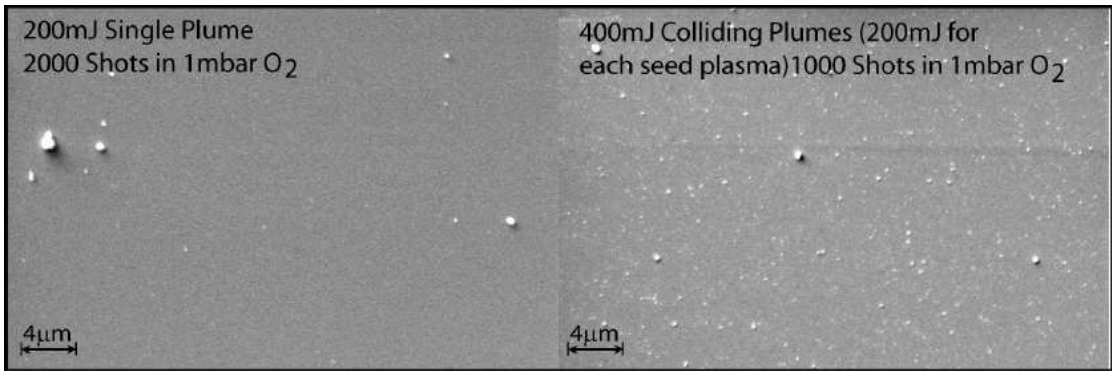

Figure 6.1: Comparison of the surface of the blank silicon substrates following deposition using a single plasma (left) and a colliding plasma (right) imaged using Scanning Electron Microscopy.

It is clear from figure 6.1 that there is a significant difference between the resulting depositions using single and colliding plasma plumes. In the case of colliding plasmas there are a lot more nano-particles deposited onto the surface of the blank substrate compared to the single plasmas case. It seems that the stagnation layer increases clusterisation of plasma enhancing the amount of nanoparticles deposited on the substrate as can be seen in figure 6.2.

A similar experiment was also performed for different parameters and again comparable results were obtained. This time the laser energy was reduced to 200 mJ (i.e. 100 mJ in each focal spot). The pressure in the chamber was also reduced to 1×10^{-1} mbar and the blank silicon substrate was positioned at a distance of 4 cm from the surface of the target. Once again, the deposition was performed for 2000 laser pulses (1000 from each seed plasma) for the single plasma deposition and 1000 laser pulses for the case of colliding plasmas. The surface morphologies of the samples were again investigated using scanning electron microscopy and the results of this are presented in figure 6.2 below.

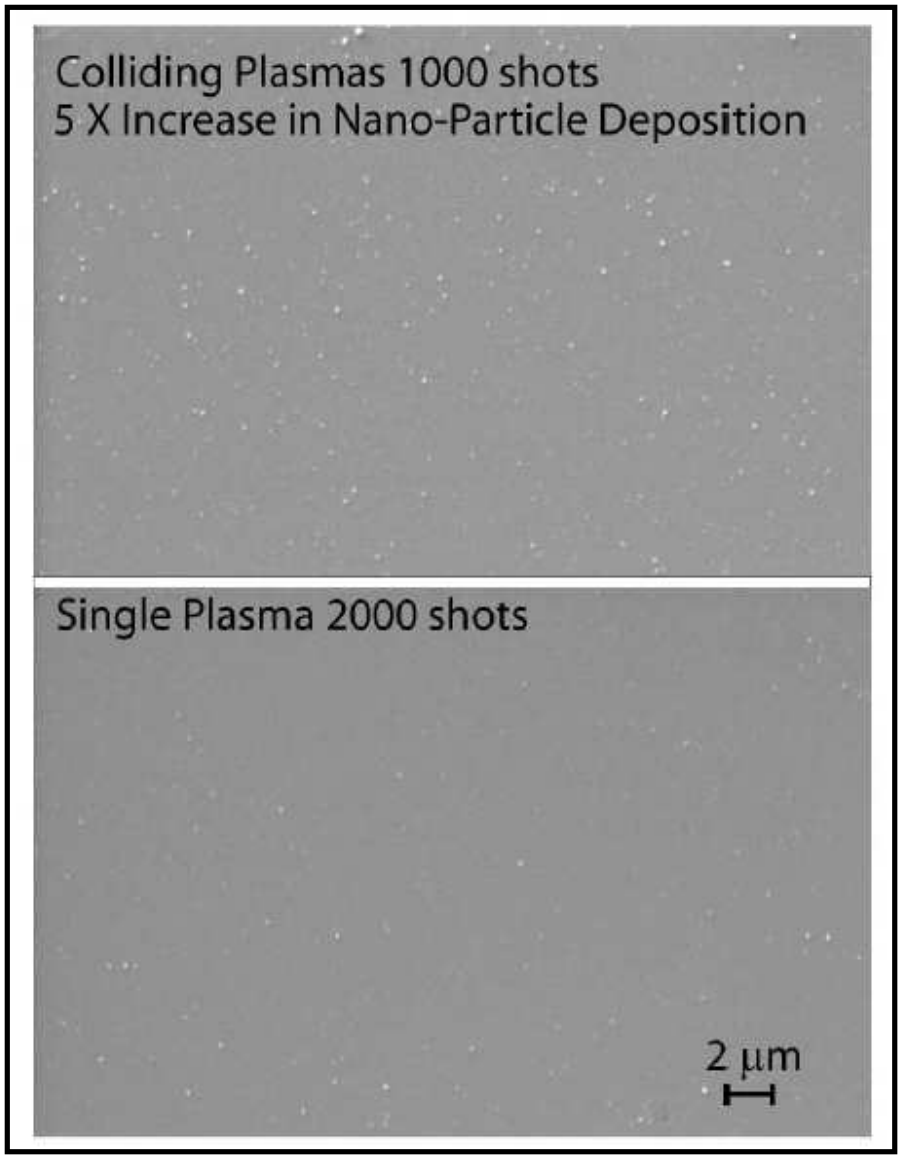

6.2: Comparison of the surface of the blank silicon substrates following deposition using colliding plasmas (top) and a single plasma (bottom) imaged using Scanning Electron Microscopy. The background pressure was kept constant at 1×10^{-1} mbar and the laser energy was set to 200 mJ (100 mJ at each focal point).

The results shown in figure 6.2 are analogous to those in figure 6.1 above where an increase in the number of nanoparticles deposited onto the surface of the substrate is clearly visible in the case of deposition of colliding plasmas. In the latter experiment a five fold increase in the number of nanoparticles on the surface of the substrate is observed.

The results from these preliminary experiments undoubtedly show that colliding laser produced plasma have the potential to be used as next generation sources of nano-structures as an enhancement in the deposition of nanoparticles is clearly visible in figures 6.1 and 6.2.

6.3: Summary

Two main applications of colliding plasmas were identified during the course of the project. Firstly, the unique characteristics of the ions emitted from colliding plasmas (e.g. narrow kinetic energy profile, enhanced tunability *etc.*) point to the potential for utilising colliding plasmas as a new source of laser produced ions, a so called colliding laser ion source.

Secondly, preliminary experiments on the deposition of materials using colliding laser produced plasmas indicate significant potential as a source for pulsed laser deposition. In particular it was found that there was an enhancement in the number of deposited nanoparticles when using colliding plasmas compared to a single plasma.

Chapter 7:

Conclusions and Outlook

In this final chapter, a summary of the results obtained during the project and an outlook for the future of colliding laser produced plasmas is is given. Potential applications beyond materials growth and suggestions for follow-on experiments are suggested.

7.1: Conclusions

The work presented in this thesis is concerned with studies of single and colliding laser produced plasmas utilising laser, optical and electrical plasma diagnostics. The project began with the design and construction of a completely new laboratory to investigate the properties and potential applications of colliding laser produced plasmas.

The first experiments concentrated on laser interferometry of single laser produced plasmas in a vacuum environment from which the 2 dimensional spatial profile of the electron density was extracted with high temporal resolution (4 ns). The substantial body of results from similar experiments provides a solid database with which to compare the results from these first experiments and to ensure that the interferometer was working well and providing physically reasonable data.

The next experiment compared the results from laser interferometry of a single plume (Zn) created vacuum with that created in a gaseous atmosphere (O_2). The results

from this study were the first to be published using the new laboratory facility. It was found that the electron density was higher at further distances from the target in the oxygen atmosphere compared to that in vacuum. This was recognised as an effect of plasma confinement which occurs when the plasma is created in a background gas. Evidence of a compressed layer of gas rapidly expanding outwards (i.e. a shockwave) that occurs at the plasma – gas interface was visible in the interferograms and manifest itself as a blurring of the fringes at the position of the compressed gas layer.

Compressive gas layers formed when laser produced plasmas expand into gaseous atmospheres have being studied extensively in the literature. The main diagnostic technique employed to study them was shadowgraphy. It was decided to further investigate them using interferometry and to compare the results to those from shadowgraphy. Several experiments were performed for single plumes created with a range of energies in a range of background gas pressures. It was found that in the pressure range ≈ 100 - 1000 mbar, the compressed gas layer was visible in both shadowgrams and interferograms and expanded with velocities of ≈ 10 kms^{-1}. However, in pressure range of ≈ 1 – 100 mbar, the visibility of the compressive layer was diminished significantly in the shadowgrams and, in fact, was impossible to detect at the low pressure end of the scale above. On the other hand the compressed gas layer was still visible as blurring of the fringes of the interferograms. Indeed the visibility of the gas layer could be further enhanced by applying a “find edges” algorithm to the interferograms which highlighted discontinuities in the interferograms. The velocity of the compressed layer at these pressures was much larger with a value peaking at just over 100 kms^{-1} for a plasma created with a 400 mJ laser pulse in a background gas pressure of 1 mbar.

Subsequent investigations focussed on colliding laser produced plasmas. The first of these experiments involved fast imaging of colliding plasmas. By employing an Intensified Charged Coupled Device (ICCD), images with high temporal resolution (3 ns)

were obtained. In addition, with the insertion of narrow band pass filters into the optical imaging system – it was possible to select line emission from particular plasma species, such as neutral atoms or singly charged ions. The spatio-temporal dynamics of neutral atoms, singly charged ions and the plasmas as a whole (i.e. a broadband filter accepting emission from all plasma species but rejecting laser light at 1.064 μm) were extracted for colliding plasmas.

In the next phase of the project complementary laser interferometry of colliding plasmas was performed which revealed the spatio-temporal behaviour of free electrons in the stagnation layer at the interface between the two plasmas. The results from the fast imaging were compared to those from the laser interferometry revealing that free electrons were the first plasma species to stagnate at the collision plane between the two colliding plasmas, closely followed by ions and finally stagnation of neutral species. These effects were attributed to the separation of charge in space in the seed plasmas, something which has been observed in the past by several different groups but made manifest optically in colliding plasma experiments.

Optical emission spectroscopy was utilised to examine the spatial distribution of different plasma species in the stagnation layer. Spectra were taken at relatively early (80 ns) and late (150 ns) time delays (relative to the life of the stagnation layer) after creation of the seed plumes. At the earlier time delay of 80 ns, it was found that the stagnation layer mainly comprised neutral atoms along with singly and doubly charged ions. Doubly charged species were found to lie at the furthest distances from the target surface followed by singly charged species. Neutral aluminium species were found to remain close to or in the vicinity of the target. Again, these effects were ascribed to ambipolar field effects in the seed plume expansion.

Angle and spectrally resolved fast imaging was performed on the colliding plasmas. Images were taken of the stagnation layer from two orthogonal angles of

view revealing the structure of the stagnation layer in both the lateral expansion plane and the vertical expansion plane (see figure 4.9 for definition of expansion planes).

The broadband images of the stagnation layer revealed it to be highly symmetric (about an axis normal to the target). The ion spatial profiles, however, were found to possess an asymmetric shape, being elongated in the vertical expansion plane. This was attributed to a "pinching" effect from the seed plumes. The neutral atoms were also found to be reasonably symmetric (albeit not to the same degree as the broadband emission) but there was clear evidence of a "V" shaped emission feature in the neutral species when viewing the lateral expansion plane. This observation was attributed to the fact that the neutral atoms are the species in the plasma with the lowest velocity and hence, collide with the outside regions of the already formed layer (mainly ions) resulting in an increase in neutral emission *i.e.* a "V" shape in the spatial emission distribution.

The final experiments concentrated on electrical probe studies of the colliding laser produced plasmas. These experiments utilised a Faraday cup as the detector which enabled extraction of the Time of Flight (TOF) distribution of the plasma species, from which the kinetic energy distribution could be obtained. The cup was based positively to attract electrons and negatively to attract the ions. The TOF profiles were then converted to kinetic energy distributions. The TOF (kinetic energy) distribution of the ions emitted from a single seed plasma was compared to that from colliding plasmas. It was found that the kinetic energy distribution from a single seed plasma followed a Maxwell-Boltzmann distribution and so exhibited a very wide range of kinetic energies. This observation has already been reported as far back as 1970's. In complete contrast, however, the kinetic energy distribution of ions emitted from colliding plasmas follows a more symmetric, Gaussian-like profile and so possesses a much narrower range of energies than single plumes.

Angle resolved measurements of the ion TOF profile revealed a double peak structure, with one of the peaks originating from angular ion emission from the stagnation layer, and the other peak emanating from a seed plasma. The angular emission from the stagnation layer diminished in both signal and energy rapidly with increasing angular deviation from normal and disappeared completely beyond ± 30°. The ion emission from the colliding plasma system was also shown to be highly tunable by varying the energy of the incident laser beam, E_L, normal to the target. The full width at half maximum (FWHM) of the ion kinetic energy signal was revealed to increase as $E_L^{1/2}$.

Finally, the end of the project focused on identifying potential applications of colliding plasmas. Single plumes are currently used as the source of laser produced ions. These sources are utilised for a wide variety of applications, e.g. injection into accelerators, surface modification and ion implantation *etc.* Factors such as laser wavelength and laser energy are utilised to adjust the properties of the ions emitted from the plasmas. With the colliding laser ion source, there exists more scope to tune the properties of the ions including target geometry and separation between the foci. With the very first experiments unveiling a source of ions with a much more symmetric distribution of kinetic energies, there is no doubting the potential for utilising colliding plasmas as a next generation laser ion source.

Very preliminary experiments were also performed on utilising colliding plasmas as a source for materials deposition, a variation on the so called “Pulsed Laser Deposition” (PLD) technique. To investigate whether there is any benefit in employing colliding laser produced plasmas in PLD applications, some first test experiments were performed on the deposition of Zinc Oxide (ZnO – 99.99% pure) using single and colliding laser produced plasmas in order to make a comparison between the two scenarios. A blank silicon substrate was used with oxygen as a background or ambient gas during the depositions. For deposition using colliding plasmas, a pair of laser beams

was focused onto the surface of the ZnO target and the material from 1000 shots accumulated.

In the case of deposition using single plasmas, one of the laser beams (called, for example, laser beam A) used to create the colliding plasma was blocked and hence not allowed to reach the target. The other laser beam (called, for example, laser beam B) remained unaffected and created a single plume at the surface of the target. The deposition was performed for 1000 laser shots after which laser beam B was then blocked and laser beam A allowed to reach the target. The deposition was again performed for another 1000 laser shots. This technique enabled a direct comparison between the sample deposition using single plumes and colliding plumes. The results indicated that there was a significant increase in the number of nanoparticles deposited on the surface of the substrate using the colliding plasmas. It is thought that the stagnation layer acts as a source for clusterisation which increases the fraction of nanoparticles emitted from the plasma and hence an increase in the deposition rate of nanoparticles is observed with the stagnation layer present.

7.2: Outlook

The work presented in this thesis indicates that colliding laser produced plasmas have significant potential for both fundamental studies of plasma collisions and applications. Starting with the basic properties of colliding laser produced plasmas, there remains a lack of systematic studies on the properties of the stagnation layer as a function of various experimental parameters, finely tuned and over a wider parameter range. The exact response of the plasma parameters of the stagnation layer, such as temperatures, densities, spatial distribution and temporal evolution *etc.*, as the parameters of the experiment are varied (*e.g.* target geometry, seed plasma

separation, laser wavelength, energy, pulsewidth *etc.*) is still not fully understood. Such systematic and fundamental studies are vital to the progression of colliding plasmas from preliminary investigations in the laboratory (as is the case currently) to being utilised for further applications. They would also provide a valuable reference when designing future experiments/applications for colliding plasmas. In addition, any next phase of the work will require the extension of existing models such as the multifluid approach [1] to the parameter range of relevance here.

This thesis has outlined two potential applications of colliding plasmas. Firstly, as a new source of laser produced ions, a so called colliding laser ion source and secondly, as a new source for materials deposition, in particular as a source of nanoparticles and clusters. Presently, only preliminary investigations have been performed here. Much more in-depth investigations are needed in order to realise these ambitions for colliding plasmas. For example, in the case of the colliding laser ion source, experiments need to be performed using a variety of targets, especially heavy targets including W and Ta which are currently widely used for applications involving standard single laser ion sources [2]. Again systematic studies are needed to elucidate the response of the ions emitted from colliding laser produced plasmas as a function of the various experimental parameters relevant to colliding plasma experiments (outlined above). The same can be said for the proposition of utilising the colliding plasma as a source for materials deposition. The preliminary studies in this thesis identify the fact that there is a strong potential for increasing the deposition rate of nanoparticles on a substrate using the colliding plasmas as the source for deposition but further, in depth, studies are needed to realise the full potential of the colliding plasmas. Systematic studies involving the effects on the deposition of the materials by varying not only the experimental parameters of the colliding plasmas (outlined above) but also experimental parameters of the deposition, for example, background gas pressure, target substrate distance, substrate orientation, substrate temperature *etc.*

It has also been shown in the literature that colliding plasmas can make an impact in other application domains. For example, colliding plasmas have already been utilised to simulate laboratory scale models of astrophysical event such as outflows associate with young stellar objects. They have been studied to replicate the events inside hohlraums indirect fusion devices where the hohlraums host multiple colliding plasmas sources to drive fusion indirectly. There is also scope to utilise colliding plasmas as a conversion medium of laser to short wavelength light in High Harmonic Generation (HHG). Single plumes have already been used successfully for this application [3] and there is no reason to believe that stagnation layers could not also be used.

In conclusion, the project has revealed some interesting findings into both the properties of the stagnation layer and the mechanisms of stagnation. Preliminary experiments have shown that there is potential to utilise colliding plasmas as a new source of laser produced ions and for materials deposition.

References

[1] P. W. Rambo and J. Denavit, Interpenetration and Ion Separation in Colliding Plasmas, *Physics of Plasmas*, **1**, (12), 4050-4060 (1994).

[2] L. Láska, J. Krása, M. Pfeifer, and K. Rohlena, S. Gammino, L. Torrisi, L. Andó, and G. Ciavola, Angular Distribution of Ions Emitted from Nd:YAG Laser-Produced Plasma, *Review of Scientific Instruments*, **73**, 2, (2002).

[3] R. A. Ganeev, M. Suzuki, M. Baba, and H. Kuroda, Extended high-order harmonics from laser-produced Cd and Cr plasmas, *Applied Physics Letters*, **94**, 051101 (2009).

Appendices

APPENDIX A1: Technical Drawings

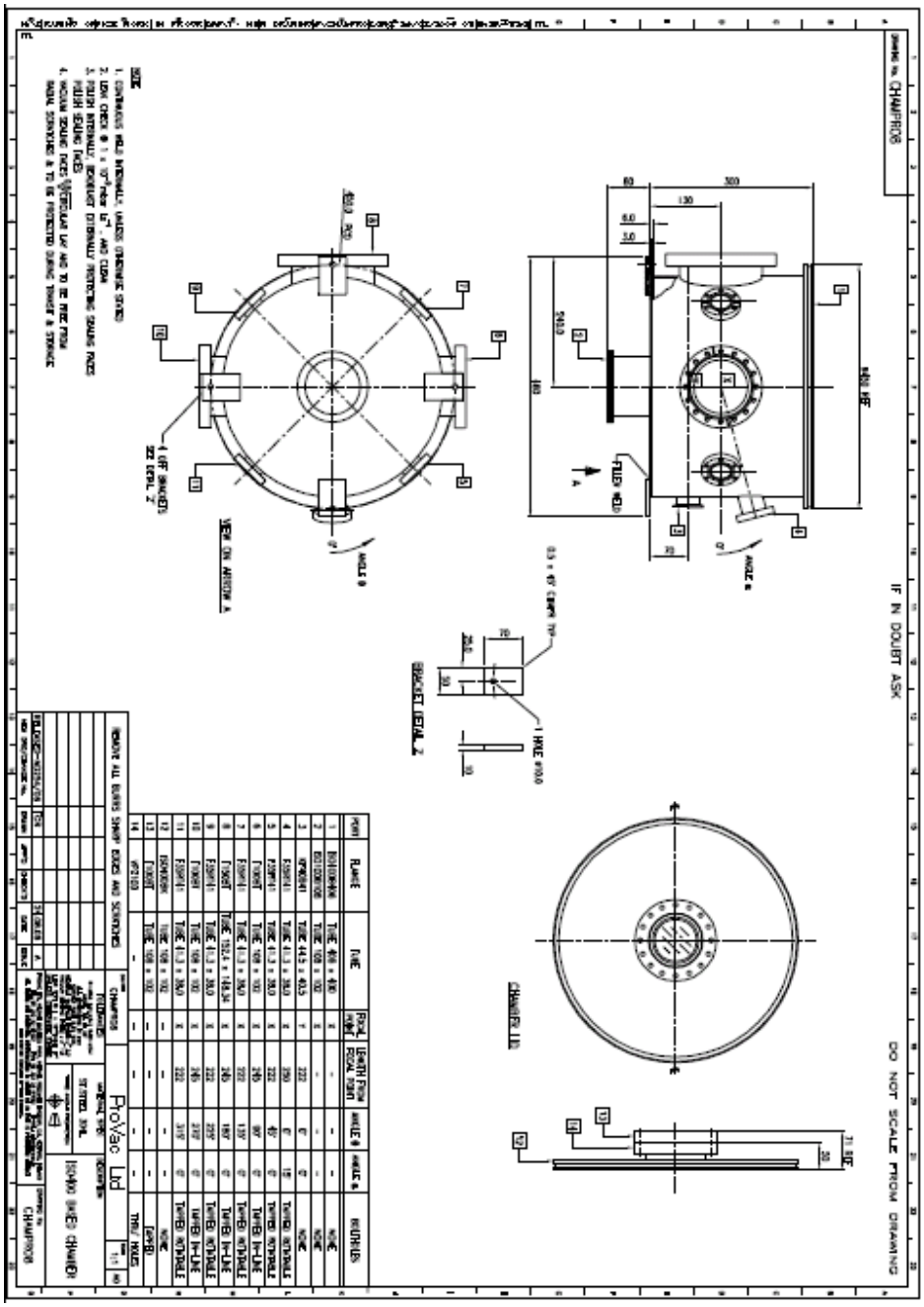

Figure A1.1: Technical drawing of the main interaction chamber and lid.

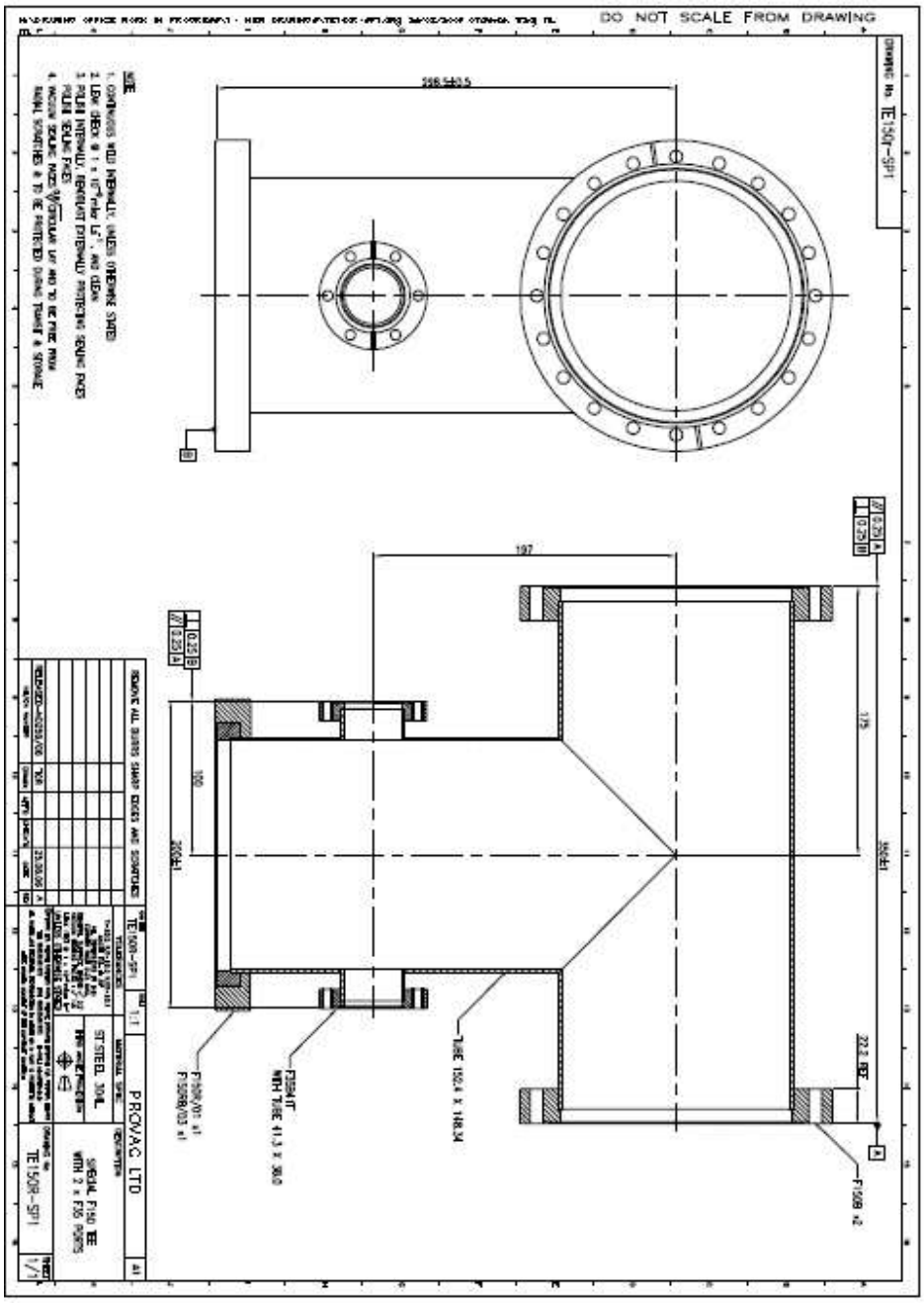

Figure A1.2: Drawing of the specially made T-Piece to connect the RETOF with the main chamber.

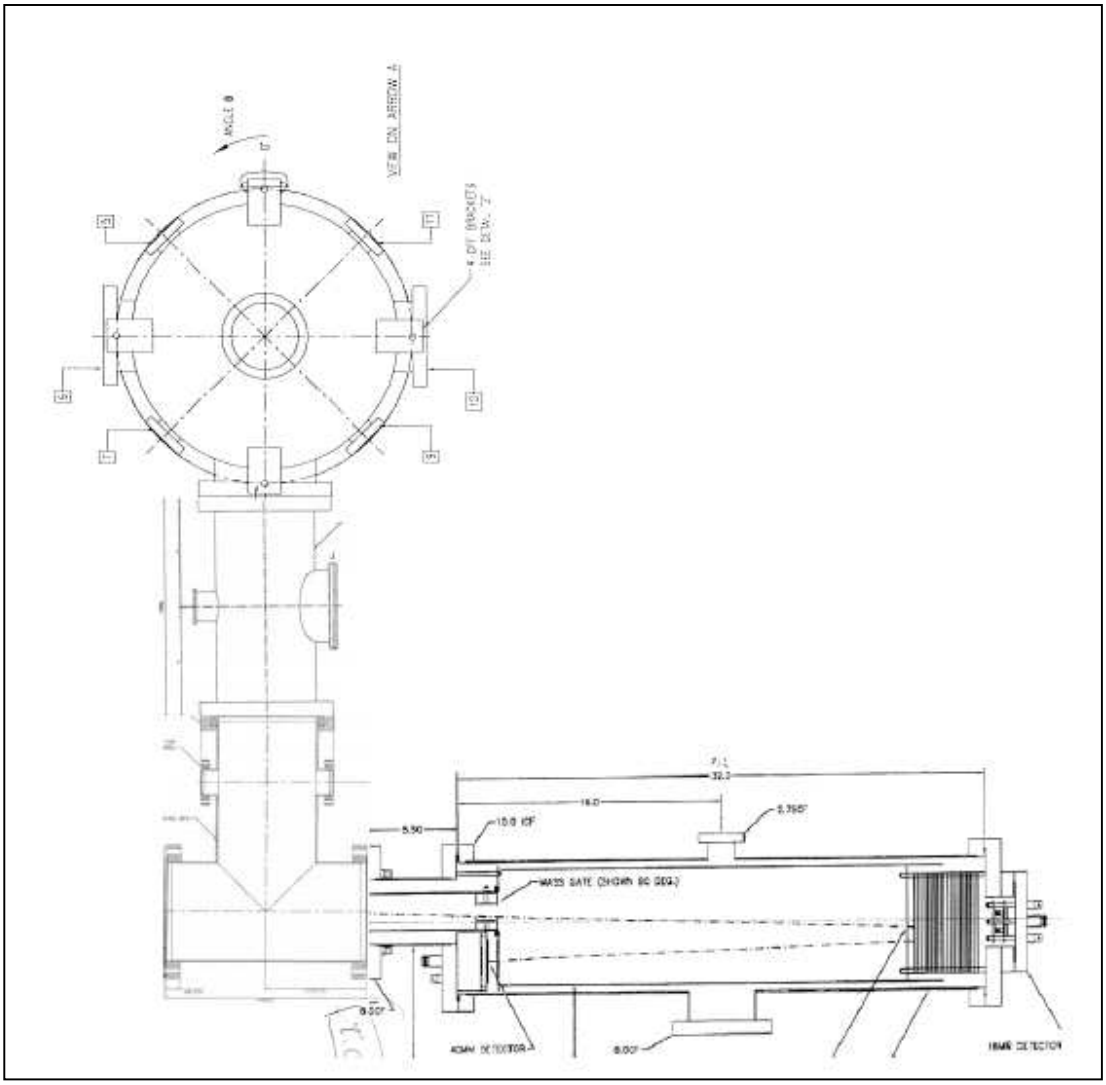

Figure A1.3: Diagram showing layout of experimental system.

APPENDIX A2: Publications and Conferences Presentations

Publications:

First Name Author:

- P. Hough, C. McLoughlin, S. S. Harilal, J. P. Mosnier and J. T. Costello, Emission Characteristics and Dynamics of the Stagnation Layer in Colliding Laser Produced Plasmas, *Journal of Applied Physics*, Accepted, December 2009.
- P. Hough, C. McLoughlin, T. J. Kelly, P. Hayden, S. S. Harilal, J. P. Mosnier, J. T. Costello, Electron and Ion Stagnation at the Collision Front Between Two Laser Produced Plasmas, *Journal of Physics D: Applied Physics*, **42**, 055211, March 2009.
- P. Hough, C. McLoughlin, T. J. Kelly, S. S. Harilal, J. P. Mosnier, J. T. Costello, Time Resolved Nomarski Interferometry of Laser Produced Plasma Plumes, *Applied Surface Science*, **255**, 10, 5167-5171, March 2009.

Other:

- S. S. Harilal, R. W. Coons, P. Hough and A. Hassanein, Influence of Spot Size on Extreme Ultraviolet Efficiency of Laser-Produced Sn Plasmas, *Applied Physics Letters*, **95**, 221501, November 2009.
- A. Azima, S. D usterer, P. Radcliffe, H. Redlin, N. Stojanovic, W. Li, J. Feldhaus, D. Cubaynes, M. Meyer, J. Dardis, P. Hayden, P. Hough, V. Richardson, E. T. Kennedy, and J. T. Costello. Time Resolved Pump Probe Experiments Beyond the Jitter Limitation at Flash, *Applied Physics Letters*, **94**, 14, 144102, April 2009.
- C. McLoughlin, P. Hough, J. Costello, E. McGlynn, J. P. Mosnier. Growth and Field Emission Properties of ZnO Nanostructures Deposited by a Novel Pulsed Laser Ablation Source on Silicon Substrates, *Ultramicroscopy*, **109**, 5, 399-402, April 2009.

- C. McLoughlin, P. Hough, J. Costello and J. P. Mosnier. Particle Diagnostics of a ZnO Laser Ablation Plume for Nanostructured Material Deposition, *Applied Surface Science*, **255**, 10, 5338-5341, March 2009.
- M. Meyer, D. Cubaynes, D. Glijer, J. Dardis, P. Hayden, P. Hough, V. Richardson, E. T. Kennedy, J. T. Costello, P. Radcliffe, S. Dusterer, A. Azima, W. B. Li, H. Redlin, J. Feldhaus, R. Taieb, A. Maquet, A. N. Grum-Grzhimailo, E. V. Gryzlova, and S. I. Strakhova. Polarization Control in Two-Color Above-Threshold Ionization of Atomic Helium, *Physical Review Letters*, **101,** 19, 193002, November 2008.
- P. Radcliffe, S. Düsterer, A. Azima, W.B. Li, E. Plönjes, H. Redlin, J. Feldhaus, P. Nicolosi, L. Poletto, J. Dardis, J.P. Gutierrez, P. Hough, K.D. Kavanagh, E.T. Kennedy, H. Luna, P. Yeates, J.T. Costello, A. Delyseries, C.L.S. Lewis, D. Glijer, D. Cubaynes, and M. Meyer. An Experiment for Two-Colour Photoionisation Using High Intensity Extreme-UV Free Electron and Near-IR Laser Pulses, *Nuclear Instruments and Methods in Physics Research A*, **583**, 516-525 December 2007.

Publications in Preparation:

- Quasi-Mono-Energetic, Tunable Ion Source Based on Colliding Laser Produced Plasmas. For submission to Applied Physics Letters.

Conferences and Poster Presentations:

I have attended 11 conferences (both in Ireland and abroad) and presented 10 posters and 1 oral presentation since October 2006. These conferences were:

2009

- 10^{th} International Conference on Laser Ablation, Singapore, 22^{nd} – 27^{th} November, 2009. Presented an oral presentation entitled "Colliding Laser Produced Plasmas as Novel Sources: Optical Diagnostics."

- 26th International Conference on Photonic, Electronic and Atomic Collisions (ICPEAC), held in Kalamazoo, Michigan, USA, 22nd – 28th July 2009. Presented a poster entitled "Colliding Laser Produced Plasmas as Novel Sources: Optical Diagnostics."
- Physics at EBITS and Advanced Research Light sources (PEARL) 2009 held in Dublin City University 6th – 9th May 2009. Presented a poster entitled "Colliding Laser Produced Plasmas as Novel Sources: Optical Diagnostics."
- Institute of Physics Spring Weekend 2009 held in Wexford, 3rd – 5th April 2009. Presented a poster entitled "Colliding Laser Produced Plasmas as Novel Sources: Optical Diagnostics."

2008

- 14th International Conference on the Physics of Highly Charged Ions (HCI) 2008 held in Chofu, Tokyo, 1st – 5th September. Presented a poster entitled "Probing Electrons and Ions in Stagnation Layers at the collision front between colliding Laser Produced Plasmas."
- European Materials Research Society (EMRS) 2008 held in Strasbourg, France, May 26th – 30th 2008. Presented a poster entitled "Time Resolved Nomarski Interferometry of Laser Produced Plasma Plumes."

2007

- Photonics Ireland 2007 held in Galway, 24th – 26th September. Presented two posters entitled "Colliding Laser Generated Plasmas as Nano-Materials Sources" and "Time Resolved Nomarski Interferometery of Rapidly Expanding Laser Produced Plasma Plumes."
- The 25th Conference on Photonic, Electronic and Atomic Collisions (ICPEAC 25) held in Freiburg, Germany, 25th – 31st July 2007. Presented a poster entitled "Colliding Laser Produced Plasmas as Atomic, Molecular and Cluster Sources: A Progress Report."

- Attended a workshop on “Plasma Processes for Biomedical Applications” held in the National Centre for Plasma Science and Technology on the 24th May 2007. Presented a poster entitled “Colliding Laser Produced Plasmas as Atomic Molecular and Cluster Sources: A Progress Report.”
- The Ninth European Conference on Atoms Molecules and Photons (ECAMP 9) held in Crete, Greece, 6th – 11th May 2007. Presented a poster entitled “Colliding Laser Produced Plasmas as Atomic Molecular and Cluster Sources: A Progress Report.”

2006

- The Third National Meeting on Quantum, Atomic, Molecular and Plasma Physics (QUAMP III) held in Durham, England, Sept. 18th - 22nd 2006.

Talks and Seminars:

- Given an oral presentation at the 10th International Conference on Laser Ablation on the 26th November 2009 entitled “Colliding Laser Produced Plasmas as Novel Sources: Optical Diagnostics.”
- Given a seminar as part of the National Centre for Plasma Science and Technology (NCPST) seminar series on the 28th November 2008 entitled “Optical Diagnostics of Plasma-Gas and Plasma-Plasma Interactions.”
- Given a seminar at a visit to the Intense Laser Irradiation Laboratory in Pisa, Italy in April 2008 entitled “Probing Electrons and Ions in Single and Colliding Laser Produced Plasmas.”

Awards:

- Won 1st place at the 1st National Centre for Plasma Science and Technology (NCPST) Poster Competition held in DCU 25/4/2008 for a poster entitled "Colliding Laser Plasmas as Novel Sources: Optical Diagnostics."
- Won 3rd place at the BOC Gases Poster competition 2009 for Physics Ph.D. students studying in the School of Physical Sciences in Dublin City University. The competition was held in DCU on the 20th Feb. 2009 and my poster was entitled "Colliding Laser Produced Plasmas as Novel Sources: Optical Diagnostics".
- Won 3rd place at the 2nd National Centre for Plasma Science and Technology (NCPST) Postgraduate Seminar Competition held in DCU 25/4/2008 after giving a seminar entitled "Spatially and Temporally Resolved Electron & Ion Mapping of Colliding Laser Produced Plasmas."

Summer School:

I have also attended a summer school on plasma physics for PhD. Students. The 8th Carolus Magnus Summer School on Plasma and Fusion Energy Physics was held in Bad Honnef, Germany, 3rd – 14th September 2007. At the summer school I presented a poster entitled "Colliding Laser Produced Plasmas as Atomic Molecular and Cluster Sources"